

Performance of RPC detectors and study of muons with the Iron Calorimeter detector at INO

By

Meghna K K

Enrolment Number : PHYS01200904012

Bhabha Atomic Research Centre

Mumbai - 400 085

*A thesis submitted to the
Board of Studies in Physical Sciences*

*In partial fulfillment of requirements
For the Degree of*

DOCTOR OF PHILOSOPHY

of

HOMI BHABHA NATIONAL INSTITUTE



October, 2015

Homi Bhabha National Institute

Recommendations of the Viva Voce Committee

As members of the Viva Voce Board, we certify that we have read the dissertation prepared by **Meghna K.K.** entitled "Performance of RPC detectors and study of muons with the Iron Calorimeter detector at INO" and recommend that it maybe accepted as fulfilling the dissertation requirement for the Degree of Doctor of Philosophy.

 Date: 17.1.17
Chair - Prof. M.V.N. Murthy


 Date: 17/1/17
Guide/Convener - Prof. Nita Sinha

 Date: 17/1/17
Co-Guide - Prof. Satyajit Saha

 Date: 17/1/17
Member 1 - Prof. Prafulla Behera

 Date: 17.1.17
Member 2 - Prof. D. Indumathi

 Date: 17.1.17
Member 3 - Prof. Jim Libby

 Date: 17.1.17
External Examiner - Prof S. Uma Sankar

Final approval and acceptance of this dissertation is contingent upon the candidate's submission of the final copies of the dissertation to HBNI.

I hereby certify that I have read this dissertation prepared under my direction and recommend that it may be accepted as fulfilling the dissertation requirement.

Date: 17/1/17

Place: 17EC, CHENNAI


Guide- Prof. Nita Sinha


Co-Guide- Prof. Satyajit Saha

STATEMENT BY AUTHOR

This dissertation has been submitted in partial fulfillment of requirements for an advanced degree at Homi Bhabha National Institute (HBNI) and is deposited in the Library to be made available to borrowers under rules of the HBNI.

Brief quotations from this dissertation are allowable without special permission, provided that accurate acknowledgement of source is made. Requests for permission for extended quotation from or reproduction of this manuscript in whole or in part may be granted by the Competent Authority of HBNI when in his or her judgement the proposed use of the material is in the interests of scholarship. In all other instances, however, permission must be obtained from the author.



Meghna K K

(Enrolment Number : PHYS01200904012)

Date: 30/10/2015

Place: Chennai

Declaration

I hereby declare that the investigation presented in the thesis has been carried out by me. The work is original and has not been submitted earlier as a whole or in part for a degree/diploma at this or any other Institution/University.



Meghna K K

(Enrolment Number : PHYS01200904012)

Date: 30/10/2015

Place: Chennai

List of publications

Publications in Refereed Journal:

1. Published

- (a) *Measurement of electrical properties of electrode materials for the bakelite Resistive Plate Chambers*, **K.K. Meghna**, A. Banerjee, S. Biswas, S. Bhattacharya, S. Bose, S. Chattopadhyay, G. Das, C. Marick, S. Saha and Y.P. Viyogi, JINST 7 (2012) P10003.
- (b) *A simulations study of the muon response of the Iron Calorimeter detector at the India-based Neutrino Observatory*, A. Chatterjee, **K.K. Meghna**, R. Kanishka, T. Thakore, V. Bhatnagar, R. Gandhi, D. Indumathi, N.K. Mondal and N. Sinha, JINST 9 (2014) P07001.
- (c) *Simulations study of muon response in the peripheral regions of the Iron Calorimeter detector at the India-based Neutrino Observatory*, R. Kanishka, **K.K. Meghna**, V. Bhatnagar, D. Indumathi and N. Sinha, JINST 01 (2015) P03011.

2. Communicated:

- (a) *Effects of variation of environmental parameters on the performance of Resistive Plate Chamber detectors*, **Meghna K. K.**, S. Biswas, A. Jash, S. Chattopadhyay, S. Saha, *Nuclear Inst. and Methods in Physics Research*, A.

Proceedings

- (a) *New development and surface characterization of bakelite-based Resistive Plate Chamber*, **Meghna K. K.**, S. Biswas, S. Bhattacharya, S. Bose, S. Chattopadhyay, G. Das, C. Marick, Y.P. Viyogi, and S. Saha, DAE Symposium on Nuclear Physics 2011, Proceedings of the DAE Symp. on Nucl. Phys. 56 (2011).
- (b) *Surface resistivity measurements and related performance studies of the Bakelite RPC detectors*, **K. K. Meghna**, A. Banerjee, S. Biswas, S. Bhattacharya, S. Bose, S. Chattopadhyay, G. Das, C. Marick, S. Saha, Y.P. Viyogi, RPC2012, PoS RPC2012 (2012) 031.

-
- (c) *Energy resolution and charge identification efficiency of muons in INO ICAL detector*, S. P. Behera, A. K. Mohanty, **Meghna K. K.**, and V. M. Datar, DAE Symposium on Nuclear Physics 2013, Proceedings of the DAE Symp. on Nucl. Phys. 58 (2013).
- (d) *A Simulations Study of the Response of ICAL Detector to Muons*, **Meghna K. K.**, Kanishka Rawat, Nufact 2013, to appear in the proceedings of NUFACT 2013.
- (e) *How Muons Are Reconstructed in Different Regions of ICAL*, Kanishka Rawat, **Meghna K. K.**, Nufact 2013, to appear in the proceedings of NUFACT 2013.

In preparation

- (a) *A Study of Atmospheric Muon Charge Ratio using ICAL detector*, Meghna K. K., D. Indumathi, Nita Sinha



Meghna K K

(Enrolment Number : PHYS01200904012)

Date: 30/10/2015

Place: Chennai

Dedicated to

My Parents

ACKNOWLEDGEMENTS

I express my sincere gratitude to my supervisors Prof. Nita Sinha and Prof. Satyajit Saha for their constant support and guidance throughout the course of this work. I am grateful to them for their personal support, patience and encouragement during my study period.

I have no words to thank to Prof. D. Indumathi for being an excellent teacher and for all valuable discussion and suggestions. I am deeply indebted to her as it would have been difficult to pursue this work without her support.

I am really thankful to Prof. M. V. N Murthy for inspiring discussions and guidance. He is a constant source of motivation for learning new things.

I would like to express my sincere gratitude to Prof. G. Rajasekharan of IMSc, Prof. Naba Mondal, Prof. Gobinda Majumder, Prof. R.G. Pillay, Prof. V. Nanal, Prof. Amol Dighe, Dr. B.Satyanarayana, Prof. S. Raychaudhuri of TIFR, Prof. J. Libby and Prof. Prafulla Behera of IITM, Prof. Uma Sankar of IIB and Prof. Vivek Datar of BARC for their help and valuable discussion at various stages.

I gratefully acknowledge Mr. N. Panyam, Mr. R. Shinde, Mr. M. Bhuyan of TIFR, Ganesh Das of VECC and Mr. Chandranath Marick of SINP for their assistance during the course of my work.

I am thankful to administration staffs at TIFR, IMSc and SINP. I gratefully acknowledge the cluster facilities at IMSc and TIFR for computational work and the persons in charge of the computing facilities.

I would like to acknowledge the INO Collaboration for giving me an opportunity to do this work.

I am thankful to my friends and batchmates Animesh Chatterjee, Lakshmi S Mohan, S. Mathimalar, Maulik Nariya, Moon Moon Devi, Neha Dokania and Thirunavukarasu Anand for their support and cooperation during my course of work.

I wish to thank my friends and colleagues Kolahal Bhattacharya, Asmita Redij, Shiba Behera, Kanishka Rawat, Mohammed Salim, Rathulnath, Tanmay Mitra, Saikat Biswas, Vivek Singh, Nitali Dash, Sumanta Pal, Anushree Ghosh, Sudeshna Dasgupta, Deepak Samuel, Rajesh Ganai, Raveendrababu Karanam, Abhik Jash, Deepak Tiwari, Chandan Gupta and many others for both academic and nonacademic discussion and support.

I am grateful to my teachers from various institutes for their continuous encouragement and motivation.

I express my special thanks to my friends Jilmy P Joy and Anvy Moly Tom for their help and moral support.

I am thankful to my friend Kannan and my comrades Riju, Joji and Ravindra for their help, inspiration and encouragement.

I express my deep gratitude to my close friends Dr. Fr. Francis Karackat and Arya. S for being there and inspiring me.

Finally, with all my heart I would like to thank my parents and brother for their trust, continuous support and patience.

Synopsis	xvii
0.1 Introduction	xviii
0.2 Characterization and study of environmental dependence of bakelite RPCs	xix
0.3 Simulation studies with ICAL detector	xxi
0.3.1 Response of ICAL to muons	xxi
0.3.2 Study of the atmospheric muon charge ratio using ICAL detector	xxiii
0.4 Summary	xxiv
1 Introduction	1
1.1 The History of neutrinos	1
1.2 Sources of neutrinos	3
1.3 Solar Neutrino Puzzle	4
1.4 Atmospheric neutrino Anomaly	6
1.5 Neutrino Oscillations	7
1.6 The ICAL at INO and its physics goals	10
1.7 The ICAL detector	11
1.8 Scope of this thesis	12
2 The ICAL Detector and Simulation Framework	17
2.1 Atmospheric neutrino fluxes	17
2.2 Neutrino interactions	18
2.3 The ICAL detector geometry	18
2.4 The magnetic field	20
2.5 Resistive plate chambers	21
2.6 The event simulation and reconstruction	22
2.6.1 Muon reconstruction	23
2.7 Chapter summary	25
3 The Response of ICAL to Muons	27
3.1 Introduction	27
3.2 Fixed vertex muons	28
3.2.1 Azimuthal dependence of the resolution	30
3.3 Smeared Vertex Muons	34
3.3.1 Track Reconstruction Efficiency	36
3.3.2 Direction (Up/Down) Reconstruction	36

3.3.3	Zenith Angle Resolution	37
3.3.4	Muon momentum resolution	38
3.3.5	Mean Shift	42
3.3.6	Momentum Reconstruction Efficiency	42
3.3.7	Relative Charge Identification Efficiency	44
3.4	The muon response at other energies	45
3.5	Peripheral and Side region	46
3.6	Summary	47
4	Atmospheric Muon Charge Ratio using ICAL detector	51
4.1	Introduction	51
4.2	Cosmic ray muon flux at sea level	53
4.2.1	Kaons and the rise of the muon charge ratio	54
4.3	Propagation of the surface muons to the detector	55
4.4	Atmospheric muon Charge Ratio	56
4.5	Muon event generation	57
4.5.1	Mountain Profile of INO site	57
4.5.2	The muon event generation	57
4.6	Reconstruction of simulated events	59
4.6.1	Reconstruction of muons inside ICAL using GEANT4	59
4.6.2	Reconstruction of surface energy of events	61
4.7	Results and Discussion	61
4.7.1	Angular dependence of the charge ratio	63
4.8	Summary	66
5	Fabrication and Testing of Bakelite Resistive Plate Chambers	71
5.1	Introduction	71
5.2	Working Principle of Resistive Plate Chambers	73
5.2.1	Modes of operation	73
5.3	Fabrication of RPCs	74
5.4	Fabrication of Pick-up panel	76
5.5	Cosmic ray test set up	78
5.6	Results	79
5.7	Summary	81
6	Effects of variation of environmental parameters on the performance of Resistive Plate Chamber detectors	83
6.1	Introduction	83
6.2	Experimental Details	84
6.3	Results and interpretation	87
6.3.1	Leakage Current	87
6.3.2	Plate Resistance	89

6.3.3	Noise Rate	91
6.3.4	Efficiency	95
6.3.5	Time Resolution and Arrival Time	97
6.4	Glass RPC in Avalanche Mode	101
6.5	Summary	102
7	Summary and Future Outlook	107
7.1	Open issues and future work	111
	Bibliography	112

Synopsis

0.1 Introduction

The study of neutrinos, the second most abundant particles in the universe, has many implications in different areas of Physics. The discovery of neutrino oscillations has clearly established that at least two neutrinos have non-vanishing masses. However the nature of neutrino mass is still an unsolved problem.

The proposed magnetized Iron Calorimeter (ICAL) detector at India-based Neutrino Observatory (INO) laboratory is designed to study atmospheric neutrino oscillations [26]. The INO lab is proposed to be located at Theni in Tamil Nadu, India. The main goals of the experiment are to measure the neutrino oscillation parameters more precisely and to determine neutrino mass hierarchy, ie. the sign of the 2–3 mass square difference $\Delta m_{32}^2 \equiv m_3^2 - m_2^2$, using atmospheric neutrinos.

Since neutrinos are weakly interacting, a large detector volume is needed to get a sufficient number of neutrino induced events. To determine whether the incoming particle is a neutrino or anti-neutrino, the charge of the secondary particle needs to be measured. The proposed ICAL will be a 50 kTon magnetized detector having this capability.

The Resistive Plate Chambers (RPCs) will be used as the active detector elements in the ICAL detector. Previous studies have shown that the operation of RPCs depends on the external environmental parameters [61–66]. The range of the external parameters in which the operation of RPCs is stable needs to be determined for the long term use of RPCs without damaging them. A study is done to investigate the effect of external temperature and humidity on the performance of RPCs and to find the range of these parameters in which RPCs are stable and effective.

The ICAL detector is mostly sensitive to the muons coming from the atmospheric ν_μ ($\bar{\nu}_\mu$) interactions. As a muon passes through RPCs it leaves its signature “hit” in each RPC; these hits can be joined to find the track of the muon. In order to determine the sensitivity of the ICAL to neutrino oscillation parameters it is important to see how accurately the ICAL simulations can reconstruct the muon information such as its momentum, angle and charge. In these studies, the response of the ICAL to fixed energy muons was studied in different parts of the ICAL detector. The momentum reconstruction efficiency, momentum and angular resolution and the charge identification efficiency were calculated as functions of energy and angle. The results of these sensitivity studies are crucial for the physics simulation studies at ICAL and have been used by the entire INO collaboration [24] for finding the sensitivity of ICAL to neutrino oscillation parameters and mass hierarchy [37, 38], etc.

Since the ICAL detector cavern at INO will have a rock overburden of 1000 m or more all around, the low energy cosmic ray muons will not reach the detector. But the muons with energy greater than 1 TeV can reach the detector. This will be a background to neutrino events. But since the neutrino interaction vertex is inside the ICAL detector, cosmic ray muon events can be separated from neutrino events. A code was developed for generating the atmospheric muon events at the INO site taking into account both the geography and the detailed topography of the surrounding hills as well as the geometry of the ICAL detector and the cosmic ray angular flux distribution. The capability of ICAL to find the atmospheric μ^+/μ^- ratio for high energy muons was studied with the code. This has implications for understanding the K/π ratio in the cosmic ray interactions.

0.2 Characterization and study of environmental dependence of bakelite RPCs

Resistive Plate Chamber (RPC) detectors are used in many experiments in High Energy and Astroparticle Physics, as trigger and tracking detectors or time-of-flight (TOF) detectors. These are gaseous detectors. The good time resolution, simple structure and comparatively good spatial resolution capabilities make them a good choice for trigger and tracking detectors. The RPC has been chosen to be the active detector in the ICAL experiment. The properties of prototype RPC detectors have been studied earlier [68–70]. The characterization of electrode material, details of construction etc., have been reported [69]. Characterization of the RPCs, specially for operation in external environment with varying temperature and humidity and interpretation of the related experimental findings have been attempted in course of this thesis work.

Two bakelite RPCs of dimension (30 cm \times 22 cm) were fabricated. The P-120 grade bakelite plates of thickness 2 mm were used as electrodes. The inner surfaces were covered with a thin layer of viscous silicon fluid. The outer surfaces of the bakelite were coated with dry graphite coatings made from 99.999% pure, -200 mesh graphite powder. The surface resistivity was found to be in the range $0.8 \text{ M}\Omega/\square - 1.3 \text{ M}\Omega/\square$.

The measurements were done by operating the RPCs both in avalanche and streamer modes. The gas used for the streamer mode was a mixture of Argon (55%), isobutane (7.5%) and environmentally friendly R134A (tetrafluoroethane) (37.5%) and that for the avalanche mode was a mixture of tetrafluoroethane (95%) and isobutane (5%). A ribbon cable based pick-up panel constructed for this experiment was used to collect the signal. The RPC was placed inside an aluminium chamber in which the temperature and humidity was kept constant during the measurement. The temperature inside chamber was measured using a PT100 sensor and the relative humidity (RH) was measured using a Honeywell HIH-4000 series humidity sensor.

Two scintillators (SC I and SC II) placed below the RPC and a finger scintillator (SC III) placed above were used to generate three fold coincidence trigger which is used as the master trigger (MT). It was found that the acceptance corresponding to this set up was equal to two adjacent strips. So the signals from two adjacent strips were ORed

and the coincidence between this signal and the master trigger gave the four-fold (FF) signal.

The measurements were done for different values of temperatures in the range $19^{\circ} - 30^{\circ}\text{C}$ and RH in the range 50 –70%. The leakage current, plate resistance, noise rate, efficiency and the time resolution of the RPC were measured.

It was found that the leakage current increases as temperature and RH increases. The resistivity of the electrode plates were obtained from the plots of leakage current as a function of applied bias voltage (I-V curve). The plate resistivity decreased slightly as RH increased, but the dependence was less compared to that due to temperature variation. Data were collected for calculation of noise rate and efficiency at each temperature and RH value. They were measured while increasing the high voltage. It was observed that for a particular RH value, the noise rate increases as temperature increases. The dependence was nonlinear and more visible above the knee voltage. The noise rate slightly decreased as RH increased.

The RPC detector performance is characterized by the detection of cosmic muons, which are detected by the RPCs in coincidence with the cosmic muon telescope. The detection efficiency is defined as the ratio of FF to master MT. The measurement was done for both the modes. It was found that as the temperature increased the voltage at which the efficiency reaches plateau decreased. A similar behaviour was observed for RH also, but the dependence on temperature was more significant. Since plate resistance decreases as temperature and RH increase, the effective voltage across the gas gap is more at higher temperature and with higher RH. The effect manifests itself relatively more for avalanche mode operation.

Since the measurement of the direction of muons (whether up going or down going) is crucial for ICAL detector, the time resolution of RPCs plays an important role. For timing calculations the signal from SC III was taken as the START of TDC and signal from a single strip of an RPC was taken as the STOP signal. The RPC was operated in avalanche mode and at a fixed voltage 12 kV. The measurements were done for 10 mV and 70 mV thresholds. The time spectrum was fitted with a Gaussian distribution to get the mean (arrival time (T)) and standard deviation (time resolution (σ)).

The arrival time decreased by 5% – 10% as temperature increased for both the thresholds. The variation of the electron drift time with temperature could be the reason for the change in the propagation delay. The temperature dependent variation of permittivity of the pick up strip may also be a contributing factor. For 10 mV threshold the resolution improved as temperature increased and for 70 mV threshold the resolution was nearly constant for all the temperatures. This behaviour could be due to the increase in the effective voltage across the gas gap and consequently the drift velocity as temperature increases. The arrival time and resolution are not much dependent on humidity.

0.3 Simulation studies with ICAL detector

Two different simulation studies were performed; one was to characterise the sensitivity of ICAL to muons and the other to study the sensitivity of ICAL to the μ^+/μ^- charge ratio in cosmic ray muons. In both cases a GEANT4 based code was used to propagate the generated muons through the ICAL detector. While the study of sensitivity of muons was restricted to fixed energy muons, the actual cosmic ray muon flux distribution was used in the second study.

0.3.1 Response of ICAL to muons

Neutrinos (ν) and anti-neutrinos ($\bar{\nu}$) interact differently with matter. A charged current interaction of the ν_μ with the detector material results in μ^- while $\bar{\nu}_\mu$ gives μ^+ which can be distinguished since ICAL is magnetized. The separation of neutrino and anti-neutrino events therefore requires accurate charge determination of the muons. This along with matter effects is crucial to distinguish Normal hierarchy from Inverted hierarchy in the mass ordering in the 2–3 sector. Since the oscillation probability is sensitive to the energy and zenith angle of the neutrino, the momentum and the angle of the muon have to be measured precisely. Hence reconstruction of momentum, angle and charge of the muons are all very crucial for ICAL physics studies.

The ICAL geometry

The geometry of the proposed ICAL detector is coded into a GEANT4 based program [25] as follows. There are three identical modules, each of size $16\text{ m} \times 16\text{ m} \times 14.45\text{ m}$, placed along x axis with 20 cm gap between them. Each module consists of 151 layers of iron plates of thickness 5.6 cm with resistive plate chambers of dimension $1.84\text{ m} \times 1.84\text{ m} \times 2.5\text{ cm}$ as active detector in the 4 cm gap between iron plates. The iron plates are supported every 2m in x and y directions with steel spacers. In each module four copper coils are placed in gaps at $x = x_0 \pm 4\text{ m}$, $|y| \leq 4\text{ m}$ where x_0 is the central x value of each module. The gaps run through the entire vertical height of the detector. This provides magnetic field in the x - y plane. The field has been mapped using MAGNET6.26 software [31]. In the central region, for a $8\text{ m} \times 8\text{ m}$ square area in the x - y plane between coil slots, the magnetic field is uniform both in magnitude and direction and maximum ($\sim 1.5\text{ T}$). For the region outside the coil slots near edges in the x direction, called the side region, the field is uniform but in the opposite direction. In the peripheral region, (outside the central region with $-8\text{ m} \leq y \leq -4\text{ m}$ and $4\text{ m} \leq y \leq 8\text{ m}$) both the direction and magnitude of the magnetic field vary considerably. The muon response in the three regions of ICAL detector has been studied separately.

Generating Muon Tracks

The ICAL detector is designed to study muons. Since the muons are minimum ionizing particles, they leave a long clean track in the detector whereas the hadrons give showers. The muon momentum and the charge are determined from the curvature of

the track in the magnetic field using the Kalman filter algorithm [34]. The energy of hadrons is determined from the number of hits in the detector.

When a charged particle passes through the detector, it gives signals in the RPC which is read using x and y pick-up strips. The z value is obtained from the layer information along with the time stamp, t . Using the hit information from three neighbouring layers, the track finder forms short tracklets which are then combined to form tracks. The track finder separates the muon track and hadron shower. If there is more than one track, the track closest to the vertex is identified as a muon track. The track fitter algorithm is based on Kalman filter. The momentum, direction and charge of the muon are reconstructed from the fitted parameters. Both the detector geometry and Kalman filter algorithm for ICAL are available as codes developed by the collaboration [24].

We have propagated 10000 muons with fixed energy and θ that follow a uniform ϕ distribution for the analysis. The vertex of the events are defined according to the region of the ICAL detector under study.

Analysis and Results

Central region: The vertex was randomly generated in the $8\text{ m} \times 8\text{ m} \times 10\text{ m}$ central volume where the magnetic field is uniform and maximal. We have taken the events with $z_{in} \leq 400\text{ cm}$ for the analysis, where z_{in} is the input z position. Both fully contained and partially contained events are analyzed. It was found that the track reconstruction efficiency, which is the ratio of successfully reconstructed tracks to the total number of events, is above 90% for muons with a momentum greater than $2\text{ GeV}/c$. Only those events which are reconstructed as a single track for which the fit is better than $\chi^2/\text{ndf} < 10$ (where ndf is the number of degrees of freedom) are considered for further analysis. The momentum reconstruction efficiency is defined as the ratio of the number of reconstructed events (irrespective of charge), to the total number of generated events. The reconstruction efficiency depends on the input momentum and the zenith angle of the muon. For momentum values below $4\text{ GeV}/c$ as the input momentum increases, the reconstruction efficiency increases for all angles, since the number of hits increases as the particle crosses a larger number of layers. At higher energies the efficiency becomes almost constant except for very small angles. The average reconstruction efficiency of about 80% is obtained in the central region.

The relative charge identification efficiency is defined as the ratio of the number of events with correct charge identification, to the total number of reconstructed events. Low energy particles undergo multiple scattering which results in the incorrect reconstruction of direction. So the charge identification efficiency is low at lower energies. But it increases as the energy increases since the number of layers with hits increases. The average charge identification efficiency of 98% is obtained.

It is found that the ICAL detector is capable of reconstructing angle very accurately. The angular resolution, which is the width of the reconstructed angular distribution

when fitted with a Gaussian distribution, improves as energy increases. It is better than a degree for all the angles.

The reconstructed momentum distribution of low energy muons shows an asymmetric tail. So they are fitted with convoluted Gaussian and Landau distributions. The momentum distributions for energies greater than a few GeV fit poorly to Gaussian distribution. This is because of the badly reconstructed events due to dead spaces in the detector. The particles with different azimuthal angle, ϕ , have different detector response because of the presence of the coil gap, support structures, orientation of magnetic field etc. Hence the muon sample was separately studied in four ϕ bins: Bin I with $|\phi| \leq \pi/4$, Bin II with $\pi/4 < |\phi| \leq \pi/2$, Bin III with $\pi/2 < |\phi| \leq 3\pi/4$, and Bin IV with $3\pi/4 < |\phi| \leq \pi$. In each bin the distribution was fitted with a Gaussian. It was found that the quality of the fit improves with this separation. The momentum resolution improves as energy increases initially since the number of layers crossed by the particle increases. But as the energy increases further the particle starts going out of the detector. The resolution worsens for such partially contained events with the straight section of track inside the detector.

Peripheral, Side regions: For the events generated in the side and peripheral regions of the ICAL detector, the results were compared with those in the central region. Due to the non-uniform and low magnetic field strength some extra selection criteria were placed while reconstructing the tracks. The reconstruction was slightly worse in both side and peripheral regions compared to the central region.

In summary, simulation studies determined that the ICAL detector had good sensitivity to muons with excellent angle and charge-id determination. The response of ICAL to muons in different regions of ICAL was completely characterized.

0.3.2 Study of the atmospheric muon charge ratio using ICAL detector

When the primary cosmic rays interact with the atmosphere they produce showers which contain pions and kaons. These secondary particles either interact with the particles in the atmosphere or decay to muons. Since the primary cosmic rays mainly contain positively charged particles, there are more μ^+ than μ^- . The measurement of charge ratio of the muons will help in the better understanding of the atmosphere neutrino flux, cosmic ray showers and the hadronic interaction. The MINOS experiment has observed a rise in the underground muon charge ratio [46] as a function of energy and also observed that the charge ratio depends on $[E_\mu^{surface}, \cos \theta]$ rather than $E_\mu^{surface}$ alone.

The surface muon flux can be described by Gaisser's formula [50],

$$\frac{dN_\mu}{dE_{\mu,0}d\Omega} \approx \frac{0.14E_{\mu,0}^{-2.7}}{\text{cm}^2.\text{sec}.\text{sr}.\text{GeV}} \times \left\{ \frac{1}{1 + \frac{1.1E_{\mu,0} \cos \theta_z}{\epsilon_\pi}} + \frac{\eta}{1 + \frac{1.1E_{\mu,0} \cos \theta_z}{\epsilon_K}} \right\}, \quad (0.3.1)$$

where $\epsilon_\pi = 115$ GeV, $\epsilon_K = 850$ GeV, $\eta = 0.054$ and the two terms in the brackets describe

the contribution from pions and kaons, with ϵ_i 's being energies at which the interaction probability of π s and K s become equal to decay probability. The parameter η is related to the relative contribution to muon decay from π and K decay respectively.

0.4 Summary

The ICAL detector at INO is designed to study the neutrino oscillation with atmospheric neutrinos using matter effect. The ability to identify the charge of the particle makes this a unique massive detector of this kind.

This thesis consists of two parts. The resistive plate chamber, the active detector element of ICAL, was fabricated, characterized and optimized. The electrode properties of the bakelite material were also studied in detail.

The dependence of RPCs on environmental parameters were investigated by varying the external temperature and humidity. The study has been done for both streamer and avalanche modes. The RPC efficiency was found to be $\sim 90\%$ in the plateau region for all temperature and humidity. The RPC parameters were found to be more sensitive to temperature than humidity and dependence is more prominent in avalanche mode than in streamer mode. The operation of RPC was found to be stable for the temperature around $21\text{--}25^\circ\text{C}$ and relative humidity $\sim 53\text{--}60\%$.

Detailed simulation studies of muons in ICAL comprises the second part of this thesis. The response of ICAL to muons was understood in different parts of ICAL detector. The central region gave the best results compared to peripheral and side region. It was found that the ICAL has good sensitivity to muons, their momentum, charge and direction.

This muon response study has been widely used in Physics simulations studies for ICAL. In particular, a study was done to find the sensitivity of the ICAL to high energy muons charge ratio. The energy and angular spectra of atmospheric muons were generated using the standard Gaisser's parametrization. The digitized topographical map of INO mountain was used for the energy loss calculation. The fitted parameters from MINOS experiment were used for generating μ^+ to μ^- ratio. The generated events were passed through ICAL code to get reconstructed events. It was found that the ICAL has very good sensitivity to this ratio in the muon energy range $\sim 1\text{--}5$ TeV, and over a large angular acceptance. When the muon passes through matter, it loses energy by ionization and radiation. The total energy loss can be expressed as [50]

$$-\frac{dE_\mu}{dX} = a + bE_\mu, \quad (0.4.1)$$

where a is the ionization loss and b is the fractional energy loss by radiation processes. These parameters are slowly varying functions of energy at the high energies where radiative contributions are important. Only muons with surface energies greater than 1 TeV will reach ICAL detector since the cavern is 1.3 km underground. At these energies a and b can be considered as constants. The values for muon with ~ 1000 GeV surface

energy are $a = 2.7 \times 10^{-3} \text{GeV}/(\text{gm}/\text{cm}^2)$ and $b = 4.0 \times 10^{-6}/(\text{gm}/\text{cm}^2)$. In terms of the surface muon energy $E_{\mu,0}$, the energy of the muon at slant depth X is given as,

$$E_{\mu} = \{E_{\mu,0} + \epsilon\}e^{-bX} - \epsilon, \quad (0.4.2)$$

where $\epsilon = a/b$. In order to calculate the slant depth the topographical map of the Bodi West Hills region, where INO is proposed to be located, is used. The map of 10 km distance around the INO peak, which is in the format latitude, longitude and elevation has been converted to r , θ and ϕ for the simplicity of flux calculation. In the simulations study, muons with energy $E_{\mu,0}$ and zenith angle θ were generated at the sea level according to the distribution given in Eqn. (4.2.1). The azimuthal angle, ϕ , distribution was generated uniformly. Then the particle was propagated through the mountain to the detector. According to the value of θ and ϕ , the slant depth is calculated from the digitized mountain profile and the energy at the detector, E_{μ}^{det} , obtained. The events were generated for five sides of ICAL detector: top, left, right, front, and back.

These events were passed through Geant based ICAL code in which detailed geometry of ICAL detector is defined. The muon momentum, charge, θ and ϕ at the detector were reconstructed using Kalman filter algorithm. The surface energy of muon and the surface charge ratio were calculated using the reconstructed momentum of the muon at the detector. The original and reconstructed charge ratio were then compared to determine the sensitivity and accuracy with which this can be determined. It was found that the reconstruction from the top face of the detector (accounting for about half the events) gives excellent sensitivity and accuracy for the muon charge ratio. In the case of events reconstructed from the sides, a systematic offset in the ratio occurred because of the azimuthal dependence in the sensitivity to muons and the topography of the mountain. This could be overcome by redefining the charge ratio including reconstruction efficiency for μ^+ and μ^- .

List of Figures

1.1	Predicted neutrino flux from mostly natural neutrino sources [11]	3
1.2	The calculated energy spectra of the solar neutrinos Ref.[13]	5
1.3	Zenith angle distributions of μ -like and e -like events for sub-GeV and multi-GeV data sets. Upward-going particles have $\cos \theta < 0$ and downward-going particles have $\cos \theta > 0$. Ref.[20]	7
1.4	The normal and inverted hierarchy	9
2.1	Muon neutrino (left) and muon antineutrino (right) total charged current cross sections in (cm^2/GeV), obtained from NUANCE, are shown (smooth lines) as a function of incident neutrino energy, E_ν , in comparison with the existing measurements of these cross sections along with their errors [28]	19
2.2	Schematic view of ICAL detector	19
2.3	Magnetic field map as generated by the MAGNET6 software.	21
2.4	Sample track of a neutrino event generating a muon track and hadron shower in the ICAL detector.	23
3.1	Muon neutrino survival probability in vacuum and matter [26]	28
3.2	Reconstructed momentum distributions for input momentum and zenith angle, $(P_{\text{in}}, \cos \theta) = (5 \text{ GeV}/c, 0.65)$ (left panel) and $(10 \text{ GeV}/c, 0.85)$ (right panel) with vertex fixed around $(100, 100, 0)$.	29
3.3	Top panels: Gaussian fits to reconstructed momentum distributions for muon energy and zenith angle $(P_{\text{in}}, \cos \theta) = (5 \text{ GeV}/c, 0.65)$ (left panel) and $(10 \text{ GeV}/c, 0.85)$ (right panel) with vertex fixed around $(100, 100, 0)$. The panels below show the effect of further removing events that reconstruct more than one track with displaced vertices – events with smaller values of P_{rec} are suppressed, fairly significantly, in the case of the more vertical, higher energy muons compared to the corresponding histograms in the panels above.	30

- 3.4 Schematic showing muon tracks (for μ^-) in the x - z plane for the same values of $(P_{in}, \cos \theta)$ but with $|\phi| < \pi/2$ and $> \pi/2$ (momentum component in the x direction positive and negative respectively). The different bending causes the muon to traverse different number of layers in the two cases. 31
- 3.5 Relative momentum resolution, σ/P_{in} , for muons with fixed momentum $(P_{in}, \cos \theta) = (5 \text{ GeV}/c, 0.65)$, plotted in bins of the azimuthal angle ϕ , with $\phi = 0$ corresponding to the x -direction. Note the y -axis does not begin with zero. 32
- 3.6 Distributions of end x positions of the track for muons with fixed momentum $(P_{in}, \cos \theta) = (5 \text{ GeV}/c, 0.65)$ in four different bins of azimuthal angle. 33
- 3.7 Different ϕ regions 33
- 3.8 Gaussian fits to momentum distributions for muons with fixed momentum $(P_{in}, \cos \theta) = (5 \text{ GeV}/c, 0.65)$ in four different bins of azimuthal angle as described in the text. 34
- 3.9 Momentum resolution as a function of energy for $\cos \theta = 0.65$ in four different bins of azimuthal angle as described in the text. The curve labelled V corresponds to the resolution of the fully smeared ϕ data. 34
- 3.10 Reconstructed momentum distributions for $(P_{in}, \cos \theta) = (5 \text{ GeV}/c, 0.65)$ smeared over the central volume of the detector for μ^- and μ^+ particles. 35
- 3.11 Reconstructed momentum distributions for $(P_{in}, \cos \theta) = (5 \text{ GeV}/c, 0.65)$ (left panel) and for $(10 \text{ GeV}/c, 0.85)$ (right panel) are compared when the vertex is fixed around $(100, 100, 0)$ and smeared over the central volume of the detector. 35
- 3.12 Reconstructed angular distribution for $P_{in} = 1 \text{ GeV}/c$ at two different input angles. 37
- 3.13 Reconstructed angular distribution for input $(P_{in}, \cos \theta_{in}) = (5 \text{ GeV}/c, 0.65)$; $\theta = 49.46^\circ$. 38
- 3.14 Angular resolution in degrees as a function of input momentum. 38
- 3.15 Momentum distributions for $(P_{in}, \cos \theta) = (1 \text{ GeV}/c, 0.65)$ fitted with Landau convoluted Gaussian; this fits better than a pure Gaussian at lower energies, $P_{in} \leq 2 \text{ GeV}/c$. 39
- 3.16 Momentum distributions for $(P_{in}, \cos \theta) = (6 \text{ GeV}/c, 0.65)$ fitted with Gaussian 39
- 3.17 Reconstructed momentum distribution for $(P_{in}, \cos \theta) = (4 \text{ GeV}/c, 0.65)$ in different ϕ bins, fitted with a Gaussian distribution. 41
- 3.18 Muon resolution as a function of muon energy for different (fixed) values of $\cos \theta = 0.45, 0.65, 0.85$, from top to bottom respectively, shown for different ϕ regions. 41

3.19	Muon resolution as a function of input momentum and $\cos \theta$, in different bins of azimuthal angle ϕ .	42
3.20	Shift in the mean of reconstructed momentum as a function of the input momentum.	43
3.21	Reconstruction efficiency as a function of the input momentum for different $\cos \theta$ values.	43
3.22	The relative charge identification efficiency as a function of the input momentum for different $\cos \theta$ values. Note that the y -axis range is 0.87–1 and does not start from zero.	45
3.23	Reconstructed momentum distributions for $(P_{in}, \cos \theta) = (0.6 \text{ GeV}/c, 0.65)$ (left panel) and for $(50 \text{ GeV}/c, 0.65)$ (right panel) with the vertex smeared over the central volume of the detector.	46
3.24	Top (bottom) figures show the reconstructed momenta P_{rec} using selection criteria $N_{hits} > n_0$ for partially contained events in the peripheral region with $(P_{in}, \cos \theta) = (5 \text{ GeV}/c, 0.65)$ (top) and $(9 \text{ GeV}/c, 0.85)$ (bottom) with $n_0 = 15$ (20) in the left (right) figure. Fully contained events have no N_{hits} constraint. In each figure, the black curve is without constraints on N_{hits} , red is with $N_{hits}/\cos \theta > n_0$ and blue is for $N_{hits} > n_0$.	47
4.1	Mountain 3D plot of 10 km distance around the INO peak. Here X and Y are the longitude and latitude in degrees while Z is the elevation in meters	58
4.2	The distribution of energy of muons at the detector for one year	60
4.3	The zenith angle distribution of muons at the detector for one year	60
4.4	The ϕ distribution of muons at the detector for one year	61
4.5	The distribution of surface energy of muons reaching the detector for one year	61
4.6	Charge ratio $R_\mu = N_{\mu^+}/N_{\mu^-}$ as a function of surface energy of the muons detected at the top surface of ICAL alone.	63
4.7	Efficiency weighted charge ratio as a function of surface energy of the muons detected over the entire detector.	63
4.8	Charge ratio as would be measured by ICAL over 1 year as a function of azimuthal angle.	64
4.9	Charge ratio as would have been measured by ICAL over 1 year as a function of zenith angle.	65
4.10	Charge ratio as a function of $E_\mu^{surface} \cos \theta$ from simulated data with 1 year exposure at ICAL.	65
4.11	Charge ratio expected to be measured over 1 year at ICAL as a function of $(E_\mu^{surface} \cos \theta)$ in comparison with other experiments.	66
5.1	Schematic representation of a RPC	75
5.2	Gas nozzles, edge spacers and button spacers	75

5.3	Left: Completed RPC. Right: Surface resistivity measurement set-up.	76
5.4	Gas mixing unit.	77
5.5	Ribbon cable pick up panel	77
5.6	Impedance of different Strips	78
5.7	Schematic view of efficiency measurement set up	78
5.8	The front-end electronics and DAQ	79
5.9	Typical induced pulse on a pick up strip at 8 kV	79
5.10	Leakage current as a function of voltage	80
5.11	Noise rate as a function of voltage	80
5.12	Efficiency(%) as a function of voltage	81
6.1	Experimental setup	85
6.2	Calibration curves for the sensors.	86
6.3	Schematic view of experimental setup	87
6.4	The leakage current for different bakelite RPCs, RPC I (left) and RPC II (right) at 7.4 kV	87
6.5	Relative humidity and temperature as a function of time during measurement	88
6.6	Electrical representation of an RPC gas gap	88
6.7	Leakage current as a function of voltage at 53% RH for different temperatures for (a) streamer, and (b) avalanche modes of operation. Lines are drawn through the data to indicate the trend.	90
6.8	Leakage current as a function of voltage at 24°C at different RH values for (a) streamer, and (b) avalanche modes of operation. Lines are drawn through the data to indicate the trend.	91
6.9	Plate resistance as a function of temperature for different RH values for (a) streamer, and (b) avalanche modes of operation.	92
6.10	Plate resistance as a function of RH at different temperatures for (a) streamer, and (b) avalanche modes of operation.	93
6.11	Noise rate as a function of applied voltage at the same RH for different temperatures for (a) streamer and (b) avalanche modes of operation. The same is plotted at the same temperature (21°C) for different RH (c) streamer and (d) avalanche modes of operation. Lines drawn through the points indicate the trend of the experimental data.	94
6.12	Efficiency as a function of voltage for the same RH at different temperatures for (a) streamer and (b) avalanche modes of operation.	96
6.13	Efficiency as a function of voltage for the same temperature at different RH values for (a) streamer and (b) avalanche modes of operation.	97
6.14	TDC Calibration curve.	98
6.15	The distribution of the time difference between the RPC and the master trigger.	99

- 6.16 Plots of (a) average arrival time T and (c) time resolution σ_{time} as function of temperature, measured for the avalanche mode operation of the RPC at 53% RH. The same observable parameters are plotted in (b) and (d) respectively as function of RH at 24°C temperature. 100
- 6.17 Efficiency and noise rate as a function of voltage for different temperature at RH = 53% 102
- 6.18 Efficiency and noise rate as a function of voltage for different humidity for T = 24°C 102

List of Tables

1.1	Neutrino oscillation parameters	10
2.1	ICAL detector parameter specifications	20

Abbreviation Notation and Nomenclature

INO	India-based Neutrino Observatory
ICAL	Iron Calorimeter
RPC	Resistive Plate Chamber
KGF	Kolar Gold Fields
CERN	European Organization for Nuclear Research (Geneva)
LHC	Large Hadron Collider
e^-	Electron
e^+	Positron
μ	Muon
p	Proton
n	Neutron
π	Pion
W^\pm	Vector boson
ν_e	Electron neutrino
ν_μ	Muon neutrino
ν_τ	Tau neutrino
$\bar{\nu}_e$	Electron anti-neutrino
$\bar{\nu}_\mu$	Muon anti-neutrino
ν_1, ν_2, ν_3	Neutrino mass eigenstates
$\theta_{12}, \theta_{13}, \theta_{23}$	Neutrino mixing angles
δ_{ij}^2	Neutrino mass squared differences
δ_{atm}	Mass squared difference measured by atmospheric neutrino experiment
δ_{sol}	Mass squared difference measured by solar neutrino experiment
L	Distance traveled by the neutrino
E	Energy of the neutrino
CC	Charged-Current (interaction)
CP	Charge conjugation and Parity (symmetry)
CPT	Charge conjugation, Parity and Time reversal (symmetry)
GZK	Greisen-Zatsepin-Kuzmin (limit)
eV	Electron Volt
α	Townsend coefficient
β	Attachment coefficient
FWHM	Full Width at Half Maximum
HV	High Voltage
PVC	Poly Vinyl Chloride
DAQ	Data Acquisition
NIM	Nuclear Instrumentation Module
CAMAC	Computer Automated Measurement and Control
VME	Versa Module Europa

Introduction

Neutrinos, the second most abundant particles in the universe after photons, are one of the least understood particles in the Standard Model of particle physics. They are neutral leptons (spin 1/2 particles) with a very tiny mass which is many orders of magnitude smaller than the masses of quarks or charged leptons. Only the left handed neutrinos and right handed anti-neutrinos have been experimentally observed. The neutrinos can have only weak interactions (except for gravity) and hence they can travel great distances without much interaction and hence can carry the information about their sources. There have been many experimental attempts to study the neutrino properties since their discovery. Their weakly interacting nature makes it difficult to observe them; hence their detection requires very large, massive detectors. The observed phenomenon of neutrino oscillations has given first signature of the physics beyond the Standard Model.

1.1 The History of neutrinos

In 1931 W.Pauli was the first scientist to propose a hypothetical neutral particle for explaining the continuous nature of the beta particle energy spectrum resulting from beta decay of a nucleus. It was thought to be a two-body decay which ought to have resulted in a discrete beta particle energy spectrum peaking at an energy equal to the Q -value of the decay process. Pauli explained the spectrum by introducing an additional neutral particle with spin half and very small mass which goes unobserved. Within the standard model of particle physics, there are now known to be three kinds of active neutrinos one associated with each of the charged leptons.

Neutrinos were first observed by Reines and Cowan in an experiment performed at the Savannah River nuclear facility [1]. They used the $\bar{\nu}_e$ flux from the nuclear reac-

tor. This neutrino flux was incident on water with $CdCl_2$ dissolved in it. The interaction of $\bar{\nu}_e$ with a proton gives a neutron and a positron. The positron annihilated with electron to produce two gamma rays. Further, the neutrons were absorbed by $CdCl_2$ and a gamma ray gets emitted after few microseconds. The coincidence between these two gamma signals confirmed the interaction of a (anti-electron type) neutrino with a proton. The muon neutrino was discovered in 1962 [2] at the Brookhaven Alternating Gradient Synchrotron (AGS). The very first neutrino beam was produced using high energy proton beam from AGS. Pions, produced by striking protons on a beryllium target, decay to give muons and neutrinos. The muons were stopped by a steel wall and only neutrinos reached the detector. These neutrinos in their subsequent weak interactions were found to produce charged muons but never electrons leading to the conclusion that a new type of neutrino (muon type) had been produced in the pion decay. A 10-ton aluminum spark chamber was used to detect the neutrinos. In 2000, the first evidence of tau neutrino was found by the DoNuT Experiment at Fermilab [3]. In DoNuT experiment a high energy beam of proton is collided with a block of tungsten to produce the charm particle D_s which decays to $\bar{\nu}_\tau$ and τ . The interaction of ν_τ with the detector produced τ which was detected using a spectrometer.

In order to explain the LSND results [4], a fourth type of neutrino which does not have any Standard Model interaction, has been proposed which is known as Sterile neutrino. But none of the experimental attempts have yet confirmed the existence of the sterile neutrino. Many models with 3 active and 1 or 2 or more sterile neutrinos have been proposed in the last few years and a huge experimental effort is currently being made worldwide, to search for sterile neutrinos.

Neutrinos were thought to be massless, but the observation of the phenomenon of neutrino oscillations proved that at least two neutrinos have non-zero mass. The limits on the sum of the three neutrino masses have been provided by the cosmological measurements [7]. The determination of absolute neutrino mass is also an interesting area of experimental neutrino physics. There are many experiments dedicated for the measurement of absolute neutrino mass eg. MARE, Mainz, KARTRIN etc. [8–10]. Many neutrinoless double beta decay experiments are running and under construction to determine the nature of neutrinos, whether they are Dirac or Majorana type. These experiments can also measure an effective neutrino mass.

1.2 Sources of neutrinos

The neutrinos are produced by different sources with varying energy range (see 1.1).

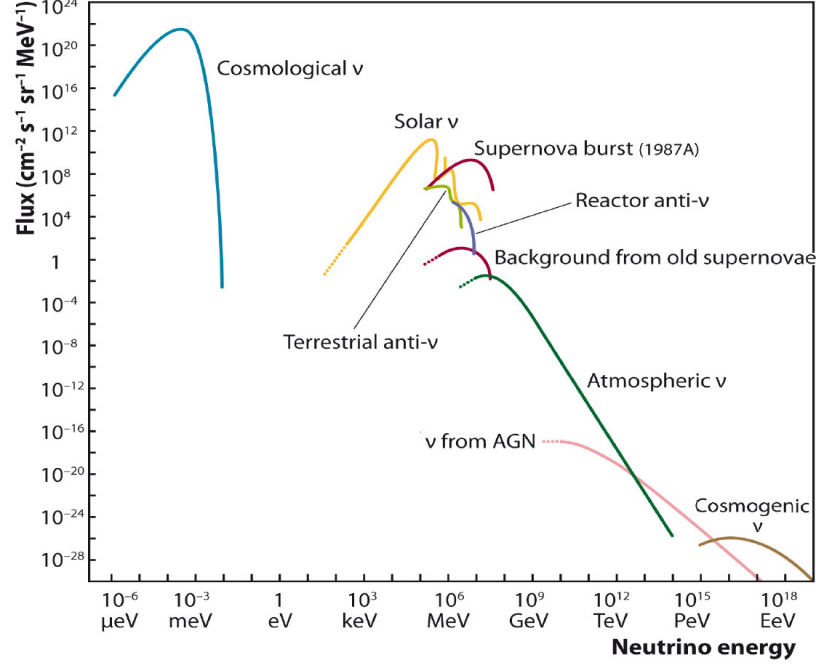


Fig. 1.1. Predicted neutrino flux from mostly natural neutrino sources [11]

According to the Big-Bang theory, there is a background of very low energy neutrinos which are known as the relic neutrinos. Though they are very numerous in Nature (about 330 neutrinos per cm^3), they evade detection since they are of very low energy. They are decoupled after the first second of birth of the Universe. The energy of the relic neutrinos is around 0.1 meV.

The Sun is a source of electron type ($\nu_e, \bar{\nu}_e$) neutrinos. The details of the production of neutrino in Sun is given in Section 1.3. They come from different nuclear reactions taking place inside the Sun and the energy range of these neutrinos depend on these reactions.

During the Supernova explosion, huge number of neutrinos are produced along with photons. Neutrinos are produced in a star during the core burning phase and carry away most of the energy. They escape from the star before light is generated as they interact with matter through the weak interaction. Light that comes out of the supernova explosion is generated after core collapse, which causes shock wave front to move outward and explode as it reaches the surface. This generates the burst of photons which therefore, follow the burst of neutrinos from the supernova explosion. This is the reason why massive neutrino detectors such as Borexino, Daya Bay, KamLAND,

LVD, IceCube, Super Kamiokande etc. are considered as parts of a SuperNova Early Warning System (SNEWS), which will provide the trigger to the astronomers to look for photon signals coming out of a possible supernova explosion. The neutrinos from supernova 1987A were detected in 1987 which confirmed the production of neutrinos in supernova. Within a time window of 12 seconds, 24 neutrinos were detected world wide and all of them were electron neutrinos.

During the decays of unstable, radioactive elements inside Earth, neutrinos are produced. Since the amount of radioactive material inside earth is unknown, the flux of geoneutrino is also not known. Measuring the geoneutrino flux can help in understanding the radioactive nature of Earth. The geoneutrinos were first observed by the Kamioka liquid scintillator antineutrino detector (KamLAND) experiment in 2005 [12]. The KamLAND has the sensitivity to electron antineutrinos produced by the decay of ^{238}U and ^{232}Th within the Earth. It is a 1000 tons of ultra-pure liquid scintillator detector surrounded by photomultiplier tubes.

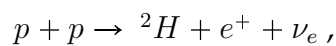
Atmospheric neutrinos are generated when the cosmic rays interact with atomic nuclei in the Earth's atmosphere. The details can be found in Section 1.4. The first observation of atmospheric neutrinos were done by underground experiments in the mines of Kolar Gold Fields (KGF) in India [5] and in South Africa [6]. The energy spectra of atmospheric neutrinos peaks around few hundreds of MeVs and it extends up to few TeVs.

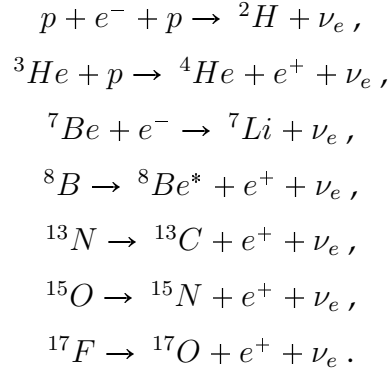
The man made nuclear reactors and particle accelerators are also sources of neutrinos. The energy of neutrinos from accelerators can go up to 100 GeVs and the reactor neutrino energy is around 4 MeV.

1.3 Solar Neutrino Puzzle

According to the Standard Solar Model (SSM), which describes the structure and evolution of the Sun, it consists of hydrogen plasma and produces energy and high intensity electron neutrino flux during nuclear fusion reactions.

Mainly neutrinos are produced in proton – proton chain reactions and the CNO cycle. Majority of the neutrinos are coming from pp chain. The following reactions in Sun produce electron neutrinos:





The solar energy spectra predicted by SSM is shown in Fig. 1.2

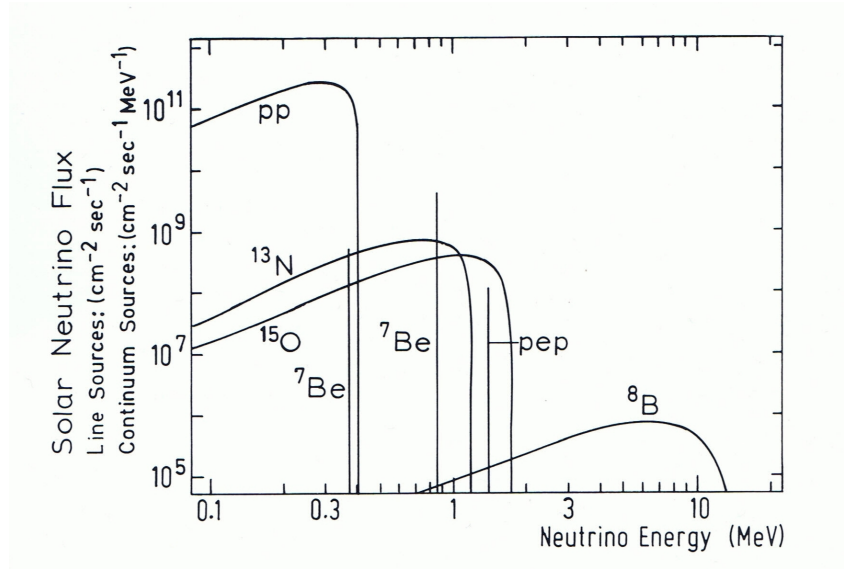
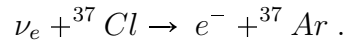


Fig. 1.2. The calculated energy spectra of the solar neutrinos Ref.[13]

The experimental study of solar neutrinos were first done by R. Davis in 1960's [14] in the well-known Homestake experiment. It was a radiochemical experiment in which ν_e interacts with chlorine to produce Argon,



The experimental set up was a huge tank containing liquid tetrachloroethylene, C_2Cl_4 . It was placed in Homestake Gold mine at 4400 mwe underground to reduce cosmic ray background. The radioactive Argon (${}^{37}\text{Ar}$, $\tau_{1/2} \approx 35$ days) atoms were collected for several months and the number of atoms were counted from their observed electron capture decay to ${}^{37}\text{Cl}$. It was found that the number of neutrino capture events measured was only about one third of the value predicted by Bahcall [15]. This is known as the solar neutrino problem and had been confirmed by many other experiments.

The Sudbury Neutrino Observatory (SNO) is a 1000 ton heavy water (D_2O) Cerenkov detector which could measure the fluxes of the electron neutrino as well as the fluxes of other flavours from the Sun. The other experiments which measured the solar neutrino spectra were mostly sensitive only to electron neutrinos. The SNO is sensitive to both charge current (CC) interaction and neutral current (NC) interactions. The CC interactions were sensitive only to electron type neutrino whereas the NC interactions were sensitive to all types of neutrinos. The SNO had measured the electron neutrino flux which was found to be less than the flux of all active flavours [16]. But the total neutrino flux via neutral current measurement was found equal to the SSM prediction. This was an evidence for neutrino flavour change.

1.4 Atmospheric neutrino Anomaly

The interaction of cosmic rays, consisting of mostly high energy ($\sim GeV$) protons, with the atmospheric nuclei produces hadron showers, mainly of pions and kaons. These hadrons decay into muons and muon neutrinos. While passing through the atmosphere the muons decay to electron, electron neutrino and muon neutrino.

$$\begin{aligned}\pi^+ &\rightarrow \mu^+ \nu_\mu & \mu^+ &\rightarrow e^+ \nu_e \bar{\nu}_\mu, \\ \pi^- &\rightarrow \mu^- \bar{\nu}_\mu & \mu^- &\rightarrow e^- \bar{\nu}_e \nu_\mu, \\ K^+ &\rightarrow \mu^+ \nu_\mu, \\ K^- &\rightarrow \mu^- \bar{\nu}_\mu.\end{aligned}$$

The ratio of number of atmospheric muon neutrinos (and anti-neutrinos) to electron neutrinos (and anti-neutrinos),

$$R = \frac{\nu_\mu + \bar{\nu}_\mu}{\nu_e + \bar{\nu}_e}, \quad (1.4.1)$$

was predicted to be 2 with 5% uncertainty. But the measurements done by water Cherenkov detectors like Kamiokande [17], IMB [18], Super-Kamiokande [19] reported smaller values of R than expected.

The Super-Kamiokande detector is a water Cherenkov detector dedicated for studying neutrino oscillation. The Super-Kamiokande data showed a zenith angle dependent deficit of muon neutrinos (Fig.1.3) [20]. It was observed that the angular spectra of upward-going μ -like events showed a deficit which was not seen in the downward going events which indicated that the deficit is dependent on path length.

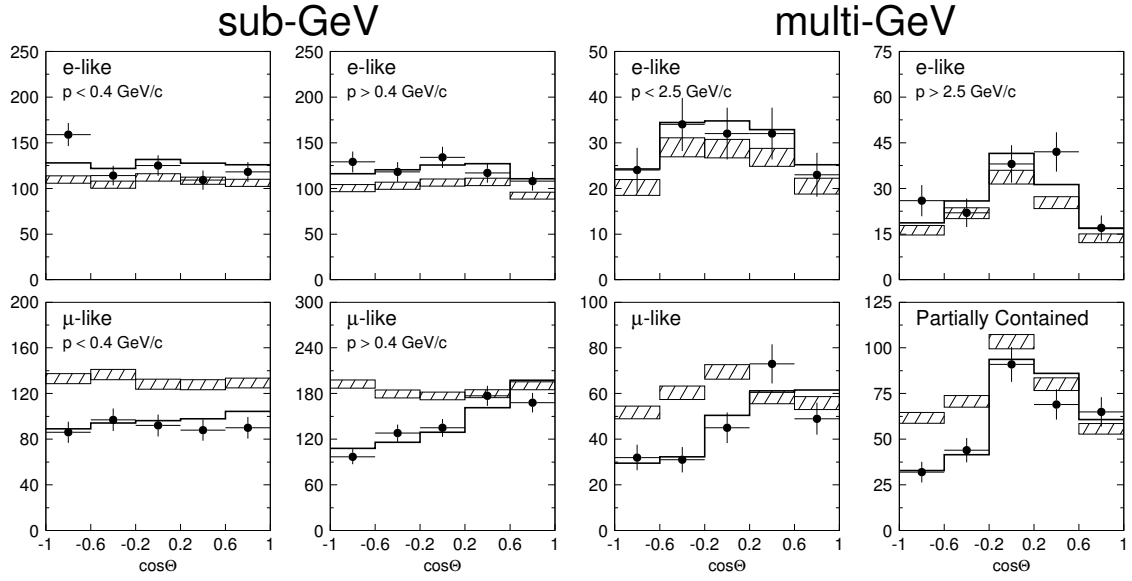


Fig. 1.3. Zenith angle distributions of μ -like and e -like events for sub-GeV and multi-GeV data sets. Upward-going particles have $\cos \theta < 0$ and downward-going particles have $\cos \theta > 0$. Ref.[20]

This is known as atmospheric neutrino anomaly.

1.5 Neutrino Oscillations

The idea of neutrino oscillations was proposed by Bruno Pontecorvo in 1957 even before any experimental evidence for this phenomenon had existed. The neutrino produced with one flavour has a non-zero probability of transition in flight to a different flavour neutrino, ν_μ , ν_e or ν_τ , by virtue of its non-vanishing mass. The discovery of neutrino oscillation opened a new era in Particle Physics by giving first evidence for physics beyond the Standard Model. In Standard Model of Particle Physics, neutrinos are massless particles and the discovery of neutrino oscillations established that at least two neutrinos have non-vanishing mass. The deficit in the number of solar neutrinos and in the ratio of atmospheric muon neutrinos to electron neutrinos can be explained by the neutrino oscillation phenomenon.

Hamiltonian for the propagation of the neutrinos in vacuum is given by

$$H_m = \begin{pmatrix} E_1 & 0 & 0 \\ 0 & E_2 & 0 \\ 0 & 0 & E_3 \end{pmatrix}, \quad (1.5.1)$$

where E_i are the energies of the neutrino mass eigenstates m_i , $i = 1, 2, 3$. Since $m_i \ll E_i$,

$$E_i \simeq p_i + m_i^2/2p_i.$$

The neutrino flavours ν_e , ν_μ and ν_τ (ν_α 's) are superpositions of mass eigenstates ν_1 , ν_2 and ν_3 (ν_i 's) with masses m_1 , m_2 and m_3 . In the basis in which the charged lepton mass matrix is diagonal, we have

$$|\nu_\alpha\rangle = \sum_i U_{\alpha i} |\nu_i\rangle. \quad (1.5.2)$$

where matrix U is a 3×3 unitary matrix known as PMNS matrix [21] which contains three sectors: solar (1–2 sector), atmospheric (2–3 sector) and reactor (1–3 sector). The PMNS matrix is given as,

$$U = \begin{pmatrix} 1 & 0 & 0 \\ 0 & c_{23} & s_{23} \\ 0 & -s_{23} & c_{23} \end{pmatrix} \begin{pmatrix} c_{13} & 0 & s_{13}e^{-i\delta} \\ 0 & 1 & 0 \\ -s_{13}e^{-i\delta} & 0 & c_{13} \end{pmatrix} \begin{pmatrix} c_{12} & s_{12} & 0 \\ -s_{12} & c_{12} & 0 \\ 0 & 0 & 1 \end{pmatrix} \quad (1.5.3)$$

$$= \begin{pmatrix} c_{12}c_{13} & s_{12}c_{13} & s_{13}e^{-i\delta} \\ -c_{23}s_{12} - s_{23}s_{13}c_{12}e^{i\delta} & c_{23}c_{12} - s_{23}s_{13}s_{12}e^{i\delta} & s_{23}c_{13} \\ s_{23}s_{12} - c_{23}s_{13}c_{12}e^{i\delta} & -s_{23}c_{12} - c_{23}s_{13}s_{12}e^{i\delta} & c_{23}c_{13} \end{pmatrix}, \quad (1.5.4)$$

where $c_{ij} = \cos \theta_{ij}$, $s_{ij} = \sin \theta_{ij}$ and δ denotes the CP violating (Dirac) phase.

In vacuum the probability of detecting a neutrino produced in flavour α and energy E , as a neutrino with another flavour β with same energy after traveling a distance L is,

$$P_{\alpha\beta} = \delta_{\alpha\beta} - 4 \sum_{i>j} \text{Re}[U_{\alpha i}^* U_{\beta i} U_{\alpha j} U_{\beta j}^*] \sin^2 \left(\frac{\Delta m_{ij}^2 L}{4E} \right) + 2 \sum_{i>j} \text{Im}[U_{\alpha i}^* U_{\beta i} U_{\alpha j} U_{\beta j}^*] \sin \left(\frac{\Delta m_{ij}^2 L}{2E} \right), \quad (1.5.5)$$

where $\Delta m_{ij}^2 = m_j^2 - m_i^2$.

In the presence of matter, there is an additional term coming because of the interaction of neutrinos with (primarily) electrons, which is diagonal in the flavor basis and is given by

$$V_f = \begin{pmatrix} V_e & 0 & 0 \\ 0 & 0 & 0 \\ 0 & 0 & 0 \end{pmatrix}, \quad (1.5.6)$$

where $V_e = \pm\sqrt{2}G_F N_e$, is the matter potential. Here G_F is the Fermi weak coupling constant and N_e is the electron density. The effective matter potential contains the contribution from both neutral current and charge current interaction. The neutral current component of the matter potential contributes equally to all the flavours. Such a diagonal term does not affect the oscillation probability, therefore it is not included in V_f .

The sign of V_e depends on whether the propagating particle is neutrino (+) or anti-neutrino (-). In the presence of matter, the mixing angle and the mass square difference get modified.

The oscillation experiments are not sensitive to the absolute mass of neutrinos. They can measure only the mass square differences. One of the most interesting factor is the mass ordering. There can be two mass ordering: $m_3 > m_2 > m_1$ which is known as normal ordering or $m_2 > m_1 > m_3$ which is known as inverted ordering (Fig.1.4). From the solar neutrino experiments the sign of Δm_{21}^2 is already measured and it is known that $m_2 > m_1$. But the sign of Δm_{32}^2 is unknown. The atmospheric neutrino experiments can probe this.

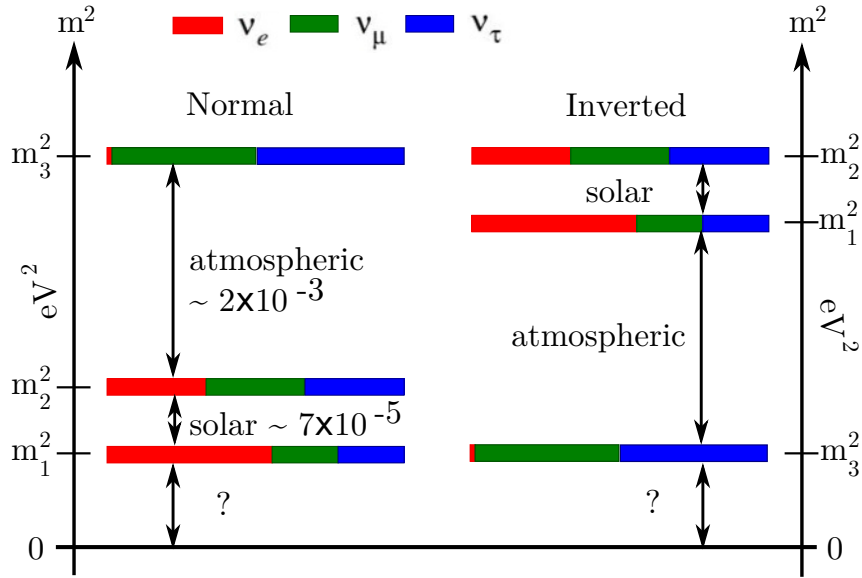


Fig. 1.4. The normal and inverted hierarchy

The magnetized Iron Calorimeter (ICAL) detector will be set up to study the atmospheric neutrinos. It will be sensitive to the oscillation probabilities $P_{\mu\mu}$, $P_{\bar{\mu}\bar{\mu}}$, $P_{e\mu}$ and $P_{\bar{e}\bar{\mu}}$. Neutrinos and anti-neutrinos interact differently with matter. In vacuum $P_{\mu\mu} = P_{\bar{\mu}\bar{\mu}}$ and $P_{e\mu} = P_{\bar{e}\bar{\mu}}$. But the presence of matter changes the oscillation probabilities depending on the sign of Δm_{ij}^2 .

The current values of neutrino oscillation parameters obtained from the global analysis of existing neutrino data are summarized in Table 1.1[22, 23].

Parameter	Best-fit values	3σ ranges	Relative 1σ precision (in percent)
Δm_{21}^2 (eV ²)	7.5×10^{-5}	$[7.0, 8.1] \times 10^{-5}$	$\sigma(\Delta m_{21}^2) = 2.4\%$
Δm_{31}^2 (eV ²)	2.46×10^{-3} (NH)	$[2.32, 2.61] \times 10^{-3}$ (NH)	$\sigma(\Delta m_{31}^2) = 2.0\%$
Δm_{32}^2 (eV ²)	-2.45×10^{-3} (IH)	$-[2.59, 2.31] \times 10^{-3}$ (IH)	$\sigma(\Delta m_{32}^2) = 1.9\%$
$\sin^2 \theta_{12}$	0.3	$[0.27, 0.34]$	$\sigma(\Delta \sin^2 \theta_{12}) = 4.4\%$
$\sin^2 \theta_{23}$	0.45 (NH), 0.58 (IH)	$[0.38, 0.64]$	$\sigma(\Delta \sin^2 \theta_{23}) = 8.7\%$
$\sin^2 \theta_{13}$	0.022	$[0.018, 0.025]$	$\sigma(\Delta \sin^2 \theta_{13}) = 5.3\%$
$\delta_{CP}(\circ)$	306	$[0, 360]$	–

Table 1.1. Neutrino oscillation parameters

1.6 The ICAL at INO and its physics goals

The iron calorimeter detector (ICAL) at the proposed India-based Neutrino Observatory (INO) is an experiment to study the atmospheric neutrinos [24]. It will be placed in an underground cavern with at least 1 km rock overburden in all directions. Only high energy cosmic ray muons and the weakly interacting particles such as neutrinos will reach the detector.

The main physics goals of ICAL are:

- to observe oscillation in the atmospheric neutrino sector and to make precision measurements of neutrino oscillation parameters. An accurate momentum and direction measurements of neutrino are very important for the precision measurements of oscillation parameters. The momentum of a charge particle produced by neutrino interaction with matter can be measured from the curvature of particle track in the magnetic field. Momentum and direction of the neutrino can be obtained from the reconstructed tracks. The details of the track fitting can be found in the Section 2.6.
- to study the matter effect experienced by the atmospheric neutrinos while passing through the Earth and to determine the sign of Δm_{32}^2 . The difference in the oscillation probabilities of ν_μ and $\bar{\nu}_\mu$ while passing through matter depends the sign of Δm_{32}^2 and the value of θ_{13} . The recent reactor neutrino experiments have found a relatively large value of θ_{13} which increases the capability of ICAL to see matter effect for determining the sign of Δm_{32}^2 . The event rate of neutrinos and

anti-neutrinos can be measured separately using a magnetized detector. When a muon neutrino (ν_μ) interacts with the detector material, it results in a μ^- while a muon anti-neutrino ($\bar{\nu}_\mu$) gives μ^+ . Hence, in order to distinguish neutrino and anti-neutrino events, the charge of the muon needs to be determined accurately. A magnetized detector can distinguish between μ^- and μ^+ events. The charge identification efficiency of the detector plays a crucial role in the determination of the mass ordering of the neutrinos.

- to look for the signature of sterile neutrinos.
- to probe the CPT violation using atmospheric neutrinos.
- to look for the non-standard interactions of neutrinos

Apart from these main goals the ICAL detector can be used to study the high energy cosmic rays, weakly interacting massive particles etc.

The cosmic ray muons are one of the major background for neutrino events. But since the vertices of the most of the neutrino events originate inside the detector, the atmospheric muon events can be separated using the event topology. Because of the rock overburden, only very high energy muons will reach the detector and practically all the cosmic muons will come only from above. The charge identification capability of ICAL can be used to measure the charge of the cosmic ray muons and hence measure the charge ratio of the muons. The study of the charge ratio and its variation according to the energy of the particles help in understanding the atmospheric neutrino flux, the composition of cosmic rays, the hadron interaction in the atmosphere etc.

1.7 The ICAL detector

In order to fulfill the goals listed above, the ICAL detector should have good energy and angular resolution and charge identification efficiency. Since the neutrino interaction cross section is very small, the detector needs to be very massive and efficient. The design of the ICAL detector satisfies these criteria.

The ICAL has three modules, each having 151 layers of iron plates interleaved with resistive plate chamber (RPC) as active detector. The active detector should have good detection efficiency and time resolution. The details of the ICAL geometry can be found in Chapter 2.

The resistive plate chambers have a good spatial resolution of about 1 cm and a time resolution of about 1 ns. The time resolution is crucial for distinguishing the up going and down going particles. The stable and the long term operation of RPC is also very important for the entire experiment. The ICAL will be using the RPCs of dimension $2\text{ m} \times 2\text{ m}$.

The iron plates of thickness 5.6 cm will be magnetized with a field strength of 1.5 T. There will be gap of 4 cm in between iron plates where the RPCs are to be placed. The signal from RPCs are collected using pick up strips.

The ICAL detector will be placed in a cavern with a rock burden of 1000 m or more all around (with a vertical overburden of $\sim 1300\text{ m}$). It is important to study the performance of the detector in different environmental conditions. The external environment can affect the performance of the detector parameters.

1.8 Scope of this thesis

In the present work, the detector properties of ICAL have been investigated in detail. The results of both the simulation and experiment are presented here.

The response of ICAL detector to fixed energy muons is studied using GEANT4 [25] simulation tool developed by CERN. The energy and angular resolution, track and momentum reconstruction efficiencies and the charge identification efficiency are calculated for different sensitive parts of the detector. These parameters are crucial for studying the sensitivity of ICAL to the mass hierarchy and the precision measurement studies of ICAL. The study is done using both fixed vertex and smeared vertex events. The muons, generated by the GEANT4 event generator, are allowed to pass through the ICAL detector. The interaction is simulated using the GEANT4 code where the ICAL geometry and the magnetization of iron plates are included in sufficient detail. The fate of the impinging muons and the hadron shower generated in course of their passage through the ICAL are obtained as outcome. The reconstructed events are analyzed to obtain the above mentioned parameters. Details are presented in Chapter 3.

Having understood the detector response, this has been used to study the sensitivity of ICAL to the atmospheric muon charge ratio. With the excellent charge identification efficiency of ICAL in a wide energy and angle range, the ratio of μ^+ to μ^- can be measured. The atmospheric muon flux at the ICAL detector is generated using a

Monte Carlo code. This uses the Gaisser's parametrization of atmospheric muon flux at the surface. The surface events are passed through the mountain in order to obtain the underground flux. The actual mountain profile of the site is used for this. The generated events are passed through ICAL code. The reconstructed events are analyzed to find the sensitivity of ICAL to the charge ratio. The results of these studies are presented in Chapter 4.

Another important aspect related to the ICAL detector involves the active detectors themselves, which are the resistive plate chamber (RPC) detectors. It is essential to understand the behaviour of these detector elements when subjected to long term operation under various laboratory environments. These aspects are also studied in course of this thesis work. Different RPCs made of bakelite are fabricated and characterized. The pick up panel using ribbon cable is also developed for this study and is presented in Chapter 5. The behaviour of RPCs under varying environmental conditions are also investigated in detail. The efficiency, time resolution, leakage current, plate resistivity and the noise rate are calculated by varying the environmental temperature and humidity. The range of parameters in which RPC operation is stable is found. The results of these studies are presented in Chapter 6.

Part I

Simulation studies

The ICAL Detector and Simulation Framework

The Iron Calorimeter (ICAL) detector will be placed in the India-based Neutrino Observatory (INO), a proposed underground facility which will be located at the Bodi West Hills (BWH) in Theni district of Tamil Nadu, India [24, 26]. The observatory will have a large underground cavern to house the ICAL detector. Other proposed experiments like search for neutrinoless double beta decay using a tin bolometer, dark matter search (DINO) etc., will also be housed in separate caverns in the same underground laboratory. There will be a rock overburden of 1 km or more around the cavern with the vertical overburden of ~ 1300 km. This will shield the detector from most of the cosmic rays and only cosmic ray muons of energy greater than a TeV will reach the detector.

The events for studying the physics capability of ICAL are generated using the NUANCE Monte Carlo generator [27]. This uses the atmospheric neutrino fluxes with various possible neutrino-nucleus interactions to generate events in the detector. It provides the vertex and momentum of all final state particles of an event. These events are propagated through a GEANT4 code developed by the collaboration [29].

2.1 Atmospheric neutrino fluxes

The atmospheric neutrinos are produced from the interaction of cosmic rays with the molecules in the atmosphere. The secondary particles like pions and kaons decay to muons and muon neutrinos and the low energy muons (anti-muons) decay to electrons (positrons), electron anti-neutrinos (electron neutrinos) and muon neutrinos (muon anti-neutrinos). Since the production of tau neutrino requires decays of mesons with heavy quarks, the flux of tau neutrino is extremely small. The atmospheric neutrinos

have an energy range from MeV to TeVs.

Above 3 GeV, the neutrino flux is symmetric about a given zenith angle on the surface of the Earth [42]. The neutrinos while passing through the Earth can introduce an up-down asymmetry due to oscillations. The geomagnetic effects can cause an asymmetry in the low energy neutrino flux in addition to the effect of oscillation.

The neutrino flux is maximum around $\cos \theta = 0$ ie. horizontal detection. The neutrino spectrum peaks around few hundreds of MeVs and then falls. There is an uncertainty of 15 – 20 % in the calculation of the atmospheric neutrino flux.

2.2 Neutrino interactions

Neutrinos take part only in weak interactions which makes it difficult to observe them. They undergo both charge current (CC) and neutral current (NC) interactions with the detector material. All CC neutrino interaction events produce an associated charged lepton.

The neutrino interactions relevant for the ICAL detector are the following:

- Quasi-elastic (QE) scattering for both charged and neutral current neutrino interactions with nucleons. This process is dominant for the neutrino energies less than 1 GeV.
- Resonant processes (RES) with baryon resonance production (like Δ resonance) for neutrino energies between 1 GeV and 2 GeV.
- Deep inelastic scattering with hadrons in the final state, which is dominant in multi-GeV regions.

The cross sections of some of the CC processes are given in Fig. 2.1.

2.3 The ICAL detector geometry

The schematic view of the 50 kt ICAL detector is given in Fig. 2.2. Monolith [?].

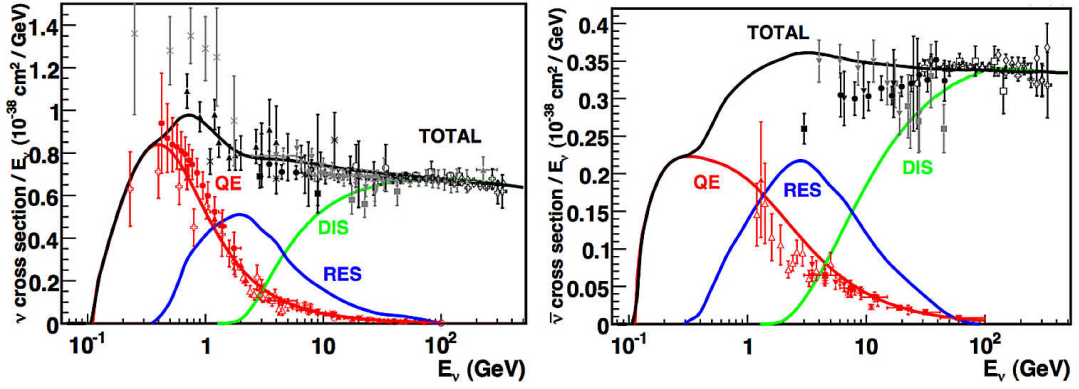


Fig. 2.1. Muon neutrino (left) and muon antineutrino (right) total charged current cross sections in (cm^2/GeV), obtained from NUANCE, are shown (smooth lines) as a function of incident neutrino energy, E_ν , in comparison with the existing measurements of these cross sections along with their errors [28]

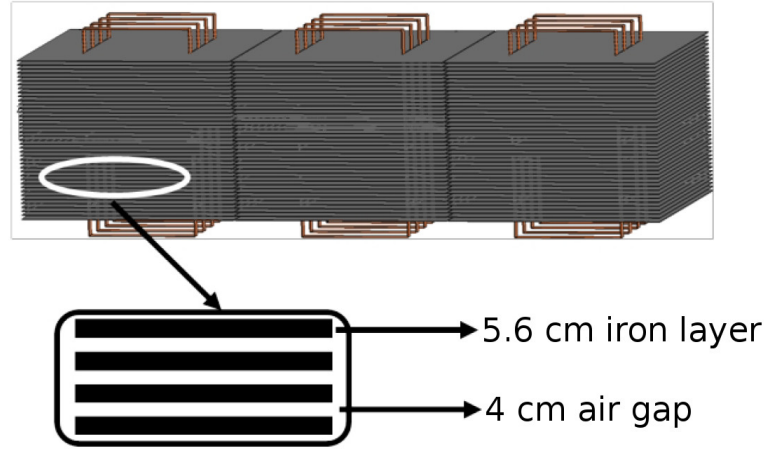


Fig. 2.2. Schematic view of ICAL detector

The ICAL detector has a modular structure. It consists of three modules each of size $16\text{ m} \times 16\text{ m} \times 14.45\text{ m}$, with a gap of 20 cm between them. Each module consists of 151 horizontal layers of iron plates of thickness 5.6 cm. There is a gap of 4 cm in between two iron plates where the active detector elements, resistive plate chambers (RPCs), are placed. The basic RPC units of size $1.84\text{ m} \times 1.84\text{ m} \times 2.5\text{ cm}$ (values used for simulation), are placed in grid-format, and have a 16 cm horizontal gap between them to accommodate steel support structures in both x and y directions. The iron sheets are supported every 2 m in both the x and y directions. There is neither a magnetic field nor an active detector element in the region of the support structures. There are 2 m wide roads along the y direction which will enable the insertion and removal of RPCs. Vertical slots, at $x = x_0 \pm 400\text{ cm}$ (where x_0 is the central x value of each module) extending up to $y = \pm 400\text{ cm}$ and cutting through all layers in each module,

are provided to accommodate the four current-carrying coils that wind around the iron plates, providing an x - y magnetic field. These slots are also free of magnetic field and RPCs. The mass of the detector is 51 kton. The basic detector parameter specifications are given in Table 2.1.

Modules	3
Module dimension	16 m \times 16 m \times 14.45 m
Detector dimension	48 m \times 16 m \times 14.5 m
Iron layers	151
Iron Plate thickness	56 mm
RPC layers	150
Gap for RPC units	40 mm
RPC dimension	1800 mm \times 1910 mm \times 20 mm
RPC units/ layer/ module	64
RPC units/ module	9600
Total RPC units	28800
Total readout channels	3686400
Magnetic field	1.5 T

Table 2.1. ICAL detector parameter specifications

2.4 The magnetic field

The simulation studies of the ICAL magnet have been done by S. P. Behera et. al [30]. A 3D electromagnetic field simulation was done to find the magnetic field distribution in an iron plate using MAGNET6.26 software [31]. The magnetic field lines in a single iron plate are shown in Fig. 2.3. The arrows denote the direction of magnetic field. The field direction reverses on the two sides of the coil slots (beyond $x_0 \pm 4$ m) in the x -direction.

The region between coil slots where the magnetic field is maximum and almost uniform in the y direction is called *central region*. The average magnetic field strength in the central region is about 1.5 T. Near the edges in the x direction outside the coil slots, the field is uniform, but in the opposite direction. This region is referred to as *side region*. The field strength is less in the side region by about 15% compared to the central region. Near the edges in the y direction ($4 \text{ m} \leq |y| \leq 8 \text{ m}$), the magnetic field varies both in direction and magnitude, this is called *peripheral region*. Near the corners the magnitude is nearly zero.

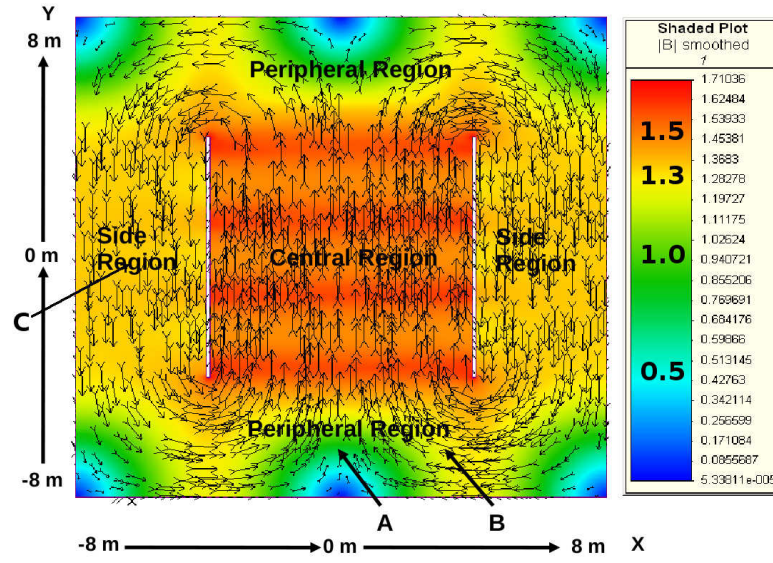


Fig. 2.3. Magnetic field map as generated by the MAGNET6 software.

The magnetic field has been generated only in the centre of the iron plate and the same field is assumed for the entire thickness of the iron plate at each (x,y) point. The field strength in the air gap between the iron plates is assumed to be zero since it is very small compared to the field strength within the iron plate.

The response of the charged particle in each region of the detector is different. In the peripheral and side regions, the edge effects and the variation of the direction and strength of the magnetic field determine the trajectory of the particles, whereas the central region is free from these effects. It is important to understand the response of the charged particles in different regions separately.

2.5 Resistive plate chambers

RPCs are gaseous detectors, in which the medium gets ionized when a charged particle passes through it. The electrode materials used here are usually glass or bakelite plates of thickness 3 mm. These plates are separated with a uniform gap of 2 mm using plastic edges and spacers. The outer surfaces of the electrode plates are coated with graphite in order to apply electric field across the gas gap. A mixture of R134A ($\sim 95\%$), isobutane and trace amounts of SF_6 gas continually flows into the chamber. The combination of gases and the highly resistive graphite coating keep the signal lo-

calized.

The signals from RPCs are collected using pick up panel made of copper. The copper sheets are pasted on a 5 mm thick foam which is used for electrical insulation and mechanical strength. These pick up panels are placed above and below the RPCs. This layer is scratched through to create uniformly spaced strips of width 1.96 cm. The pick up panels are placed in such a way that the strips above and below are transverse to each other, that is, in the x and y directions, to provide the x and y locations of the charged particle Ref. [32]. More details about RPCs can be found in Chapter 5. These and further details of various geometric and materials aspects of the RPCs are included in the simulation framework.

2.6 The event simulation and reconstruction

This thesis mostly contains the studies with muons in the detector. However, for the sake of completeness, the entire event simulation and recognition for both muons and hadrons is described below.

When neutrinos interact with the detector materials, charged leptons and hadrons are produced. The ICAL is more sensitive to muons. Being a minimum ionizing particle, muons create long tracks in the detector whereas hadrons generate showers. These secondary particles pass through the iron plates and RPCs, and generate the signal pulses. The propagation of the particles through the detector is simulated using GEANT4 package developed by CERN [25]. The ICAL geometry is written to a GDML file that can be read off by the event reconstruction package.

When a charged particle passes through the detector, it gives signals in the RPC which is read using x and y pick-up strips. The z value is obtained from the layer information along with the time stamp, t . This digitized signal is known as a “hit” in the detector. Because of the strip width, the spatial resolution in x and y are about 0.6 cm, and it is about 1 mm in the z direction due to the gas gap. The information on cross-talk from the ongoing R&D of RPCs has also been incorporated in the analysis.

A typical neutrino CC interaction event generating a muon track and associated hadron shower is shown in Fig. 2.4. It can be seen that the muon track is clean with

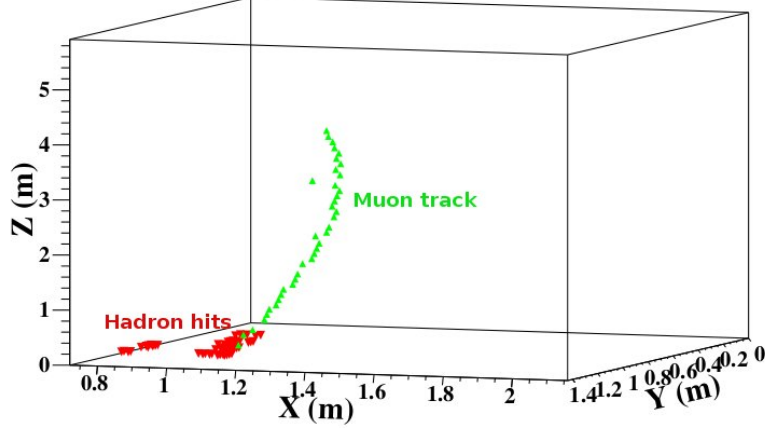


Fig. 2.4. Sample track of a neutrino event generating a muon track and hadron shower in the ICAL detector.

typically 1 hit per layer. In the case of multiple tracks, the reconstructed track closest to the vertex is considered as the muon track.

2.6.1 Muon reconstruction

In order to analyze the data, the event has to be reconstructed accurately for determining the particle position, momentum, direction and charge. This is achieved using all the information obtained from the detector as the particle passes through it.

The hadron usually leaves more than a hit in every layer. Since the x and y strip information are independent, all the possible pairs of nearby x and y hits in a plane are combined to form a *cluster*. The hadrons travel short distances in the detector and the reconstruction of an individual hadron cannot be done, since it generate shower. In the case of hadrons, while combining x and y hits there can be false count of hits, which is known as ghost hits, because of the multiple hits in a layer. In order to avoid this situation, either x or y hits are considered for the energy calibration. The hadron energy is calibrated from the total hadron hits in an event [33].

Typically muons leave only about one or two hits per layer (~ 1.6 on average) as they propagate. Hits in adjacent layers are combined to form tracklets. The tracklets are combined to form tracks if there are hits in at least five consecutive layers.

Muons leave long tracks in the detector. The muon momentum and charge can be reconstructed from the curvature of the track in the magnetic field or from the path length. The Kalman filter which takes into account the local magnetic field is used to fit a track [34]. The Kalman filter uses a track finder algorithm followed by a track fitter which gives the fitting parameters which can be used to find the momentum, charge and the angle of incoming muon.

The track finder: The track finder algorithm is a pattern recognition algorithm to find all the possible track candidates. The track finder uses the clusters formed from hits as basic elements of the algorithm. A set of clusters generated in a few successive layers is combined to form a *tracklet*.

The track finder finds all possible tracklets by considering clusters in three adjacent planes. It considers the possibility of no hits in a plane because of inefficiency of the active detector. In such cases the next plane will be considered. The tracklets are combined to form long tracks if their end points match. The direction (up/down) of the track is calculated from the timing information which is averaged over the x and y timing values in a plane. Since the particles travel with the relativistic velocity, enough number of layers should have hits to get the direction information. The track finder also separates out tracks as “shower-like” or “muon-like”. For the case of muon-like tracks, the clusters in a layer are averaged to form a single hit per layer with x , y and timing information and are sent to the track fitter which uses these information to fit the track.

The track fitter: A Kalman filter based algorithm is used to fit a track. It takes into account the local magnetic field, the multiple scattering experienced by the particle as it propagates and the energy loss of particle in the detector material. Every track is identified by a starting vector $X_0 = (x, y, dx/dz, dy/dz, q/p)$ where x and y are coordinates of the hit in a particular z plane. The charge-weighted inverse momentum q/p is taken to be zero for the first iteration. The slopes dx/dz and dy/dz are associated with the direction of the track. The initial state vector is extrapolated to the next layer using the Kalman filter algorithm which takes into account the process noise and the local mag-

netic field. The energy loss of the particle in a step is calculated using the Bethe-Bloch formula [35]. The prediction of the q/p is done using the energy loss information in the material through which the particle is propagating. Each step uses the prediction from the previous step as the initial state of that step. The extrapolated point is compared with the actual location of a hit in that layer, if any, and the process is iterated.

After filtering all the hits in a track, the same process is done in the reverse order for smoothing the track.

The fit parameters: The process of iteration in forward and reverse also achieves the best fit to the track. In order to determine the vertex of the interaction, the track is extrapolated to another half-layer of iron. This is done since the interaction is most likely to have taken place in the iron. The best fit value of the momentum at the vertex is returned as the reconstructed momentum (both in magnitude and direction). While q/p determines the magnitude of the momentum at the vertex, the direction is reconstructed using dx/dz and dy/dz , which yield $\cos \theta$ and ϕ .

2.7 Chapter summary

The atmospheric neutrino flux and the neutrino interactions relevant for the ICAL detector are discussed briefly here. Since the neutrino interacts only via weak interaction, the interaction cross section is very small. This demands a massive detector for studying neutrino properties.

The design of the ICAL detector which is going to be used to study the atmospheric neutrinos is discussed. The geometry of the ICAL detector which is a 51 kton magnetized calorimeter is described. It can be magnetized up to about 1.5 T. Resistive plate chambers will be used as the active detector elements.

The ICAL geometry is described in a GEANT4 based code which is used for the propagation of particles through the ICAL. The hits of the charged particles are registered which are used later for reconstructing the events in the detector using the Kalman filter algorithm.

The Response of ICAL to Muons

3.1 Introduction

As discussed earlier, an accurate determination of the muon energy and direction is crucial to achieve the neutrino oscillation physics goals. The muon energy and direction information can be combined with that of the hadrons to get the energy and direction of the neutrinos. Though the CC ν_e interactions produce electrons in the final state, ICAL is not optimised to reconstruct their energy and direction because of their rapid energy loss mechanisms in the dense iron.

The atmospheric neutrino flux peaks at a few hundred MeVs, and then falls rapidly with neutrino energy with roughly an $E^{-2.7}$ dependence whereas the interaction cross-section only increases linearly with energy. Hence events in the detector are dominantly of lower energy, below 20 GeV. The matter effect is more prominent for energies of a few GeV. Fig. 3.1 shows ν_μ survival probability in vacuum and in matter for different distances traveled by neutrinos and it can be seen that the matter effect is dominant in the energy range 5–10 GeV. The results of a GEANT4-based simulation study of the response to muons in the central region of the ICAL detector for energies of a few GeV is presented in this chapter.

In order to understand the response of the detector both fixed vertex and smeared vertex analysis have been carried out [36]. The events are generated using GEANT4 for fixed energy and zenith angle. The azimuthal angle ϕ is smeared over the range $(-\pi$ to $\pi)$ uniformly. The reconstruction efficiency, momentum resolution, angular resolution and the charge identification efficiency of muons in the (1–20) GeV/c momentum regime are calculated. The detector response to muons has been already used to study

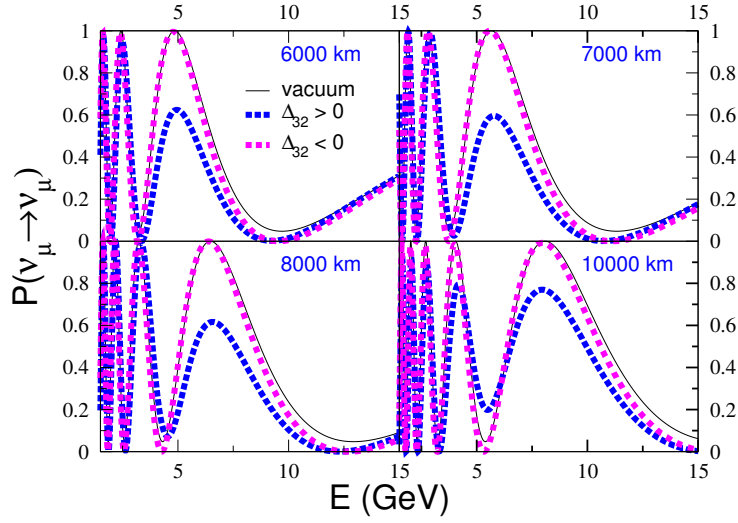


Fig. 3.1. Muon neutrino survival probability in vacuum and matter [26]

the physics reach of ICAL for the precision measurements of neutrino oscillation parameters and determination of the neutrino mass hierarchy [37],[38]. Investigations of response of hadrons were also done. Hadron energy and effective momentum of hadrons have been studied [39], [40]. Physics analysis including hadron energy information as third input in addition to muon energy and direction, has also been done [24]. Combining muon and hadron information to reconstruct neutrino kinematic variable is a very challenging problem and has not been studied so far. A separate study of the response to muons in the peripheral region of ICAL is briefly discussed at the end of this chapter.

3.2 Fixed vertex muons

The dead spaces like the coil gap and the support structures that have no active detector elements, are more or less uniformly distributed throughout ICAL. In order to understand the impact of these on the detector response, muons with vertices fixed at the location $(x, y, z) = (100 \text{ cm}, 100 \text{ cm}, 0 \text{ cm})$ which is equidistant from the supports at $x, y = 0, \pm 200 \text{ cm}$ are studied. A smearing over a small volume ($\pm 10 \text{ cm}, \pm 10 \text{ cm}, \pm 10 \text{ cm}$) is done to smear out the effects of local non-uniformities. The histograms of reconstructed muon momenta P_{rec} for two sample energies with the modulus of the input three-momentum $P_{\text{in}} = 5, 10 \text{ GeV}/c$, are shown in Fig. 3.2 for $\cos \theta = 0.65$ and $\cos \theta = 0.85$ and $-\pi \leq \phi \leq \pi$. The histograms are plotted in the range $0-2P_{\text{in}}$ for convenience as there are hardly any events that reconstruct outside this range. The mean value of the distribution is close to the input momentum, and the RMS width (square

root of variance) of the distribution, which is proportional to the momentum resolution (which is the ratio of the width to the input momentum), increases with input energy.

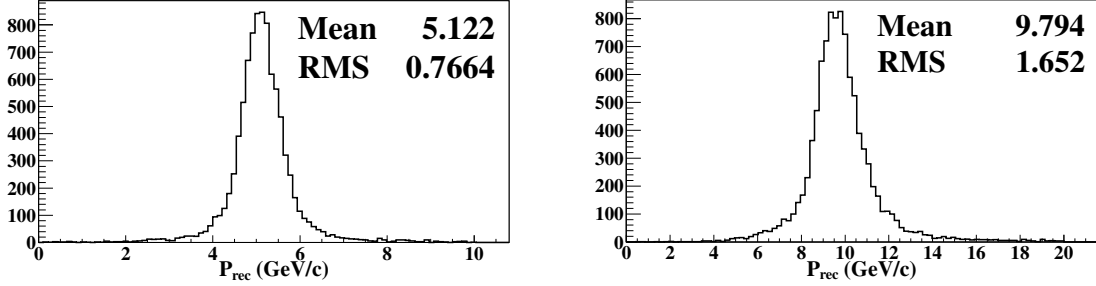


Fig. 3.2. Reconstructed momentum distributions for input momentum and zenith angle, $(P_{\text{in}}, \cos \theta) = (5 \text{ GeV/c}, 0.65)$ (left panel) and $(10 \text{ GeV/c}, 0.85)$ (right panel) with vertex fixed around $(100, 100, 0)$.

The reconstructed momentum distributions have non Gaussian tails, as can be seen for example from the fits to the data sets in Fig. 3.3. This is because most of the events reconstruct within a narrow histogram while about 5–10% of the total events (which are contributing to the tails) lie outside the Gaussian curve, causing poor fits with $\chi^2/\text{ndf} \sim 8$. These tails, especially at the lower momentum end of the distribution, arise in part due to the detector dead spaces. This is explained in detail below.

Sometimes the Kalman filter reconstruction algorithm reconstructs a single track traversing a support structure as two disjoint tracks. The reconstructed momentum of these two tracks will be larger or smaller than the actual momentum depending on whether it was the earlier or the later part of the track. This is due to the fact that the false tracks which are only sections of the single correct one, have arbitrary intermediate vertices where the momentum is reconstructed. When the tracks with small angles pass through the support structures, the two portions of the track on either side of the support structure, which does not have hits, may be displaced by several layers along the z axis with respect to each other. The problem is also more severe in the case of higher energy muons, because of their longer length of the tracks inside such dead spaces. So this problem is more in the case of small angle high energy events. But in the case of genuine neutrino events at such energies, the hadron shower associated with these muon tracks will help select the true vertex and reject the spurious, displaced ones. Hence such events may be safely removed from the analysis of pure muon events. Though removing such events improves the momentum resolution, the momentum reconstruction efficiency, especially at small angles, will be worsened. Here only the events with single reconstructed track are considered for the analysis.

Apart from the cut on the number of tracks in a particular event, a cut on reduced χ^2 is also used to select the events for the analysis. Only the tracks which satisfy the cut $\chi^2/\text{ndf} < 10$ are considered. For calculating the track reconstruction efficiency only the cut on χ^2 is used.

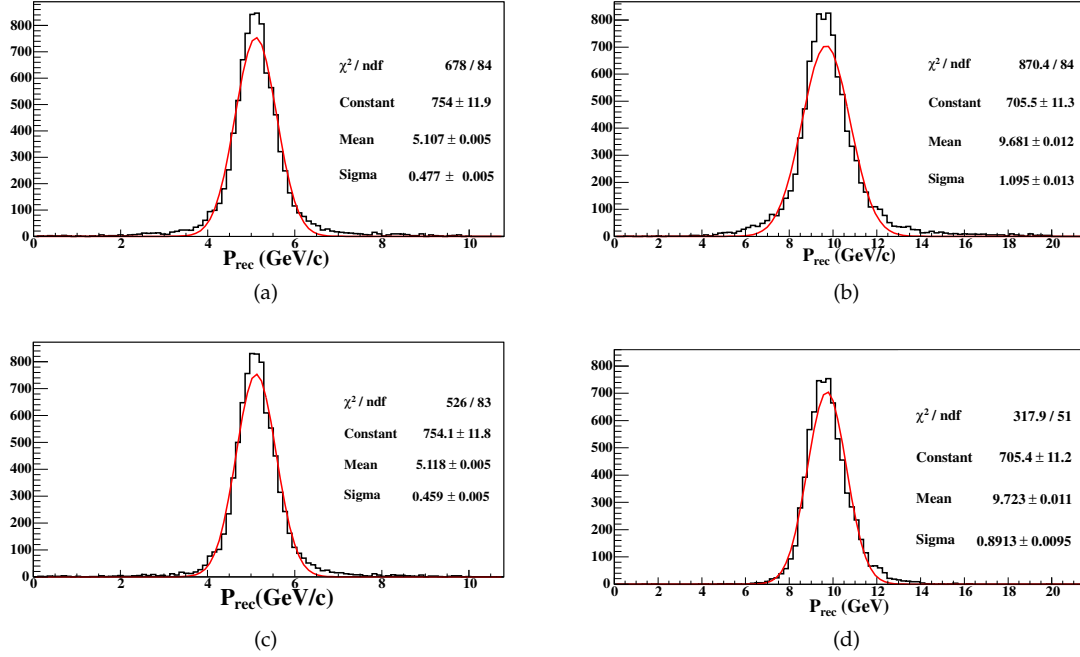


Fig. 3.3. Top panels: Gaussian fits to reconstructed momentum distributions for muon energy and zenith angle $(P_{\text{in}}, \cos \theta) = (5 \text{ GeV/c}, 0.65)$ (left panel) and $(10 \text{ GeV/c}, 0.85)$ (right panel) with vertex fixed around $(100, 100, 0)$. The panels below show the effect of further removing events that reconstruct more than one track with displaced vertices – events with smaller values of P_{rec} are suppressed, fairly significantly, in the case of the more vertical, higher energy muons compared to the corresponding histograms in the panels above.

3.2.1 Azimuthal dependence of the resolution

The response of the detector has been averaged over the entire azimuth. But it was observed that for the same zenith angle, $\cos \theta$, muons with different azimuthal angles have different response. The reconstruction is very good in some ϕ bins, but poor in other. There are several reasons for the ϕ dependence: the dead spaces like the coil gaps that are located at $x = x_0 \pm 400 \text{ cm}$ where x_0 is the centre of each module in the x direction and the support structures, which have different dimensions in the x - and y -directions; and also the orientation of the magnetic field. The cumulative ϕ dependence that we describe below is a complex consequence of all these factors.

A muon initially directed along the y -axis experiences less bending since the momentum component in the plane of the iron plates (which is referred to as in-plane momentum) and the magnetic field are parallel. The force experienced by an upward-going muons that are in the negative (positive) x direction is in the positive (negative) z direction (the opposite is true for μ^+) and so muons injected with $|\phi| > \pi/2$ traverse more layers than those with the same energy and zenith angle but with $|\phi| < \pi/2$. Hence their quality of reconstruction improves. This is illustrated in the schematic in Fig. 3.4 which shows two muons (μ^-) injected at the origin with the same momentum magnitude and zenith angle, but one with positive momentum component in the x direction, $P_x > 0$ and the other with negative x momentum component, $P_x < 0$. The muon with $P_x > 0$ (initially directed in the positive x direction) bends differently than the one with $P_x < 0$ (along negative x direction) and so they traverse different number of layers, and have roughly the same path length. Hence, muons with different ϕ shows different detector response.

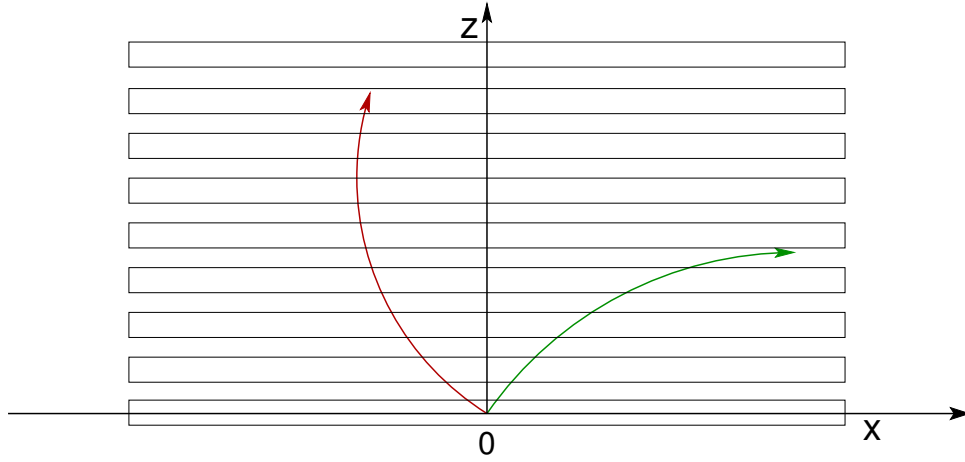


Fig. 3.4. Schematic showing muon tracks (for μ^-) in the x - z plane for the same values of $(P_{\text{in}}, \cos \theta)$ but with $|\phi| < \pi/2$ and $> \pi/2$ (momentum component in the x direction positive and negative respectively). The different bending causes the muon to traverse different number of layers in the two cases.

The response of muon in different ϕ regions can be seen from Fig. 3.5 where the momentum resolution (R), defined (with its error δR) in terms of the RMS width σ (with an error $\delta\sigma$) of the histogram as,

$$R \equiv \sigma / P_{\text{in}}, \quad (3.2.1)$$

$$\delta R / R = \delta\sigma / \sigma .$$

is plotted as a function of the azimuthal angle ϕ .

The response is symmetric in $\phi \longleftrightarrow -\phi$, within errors. It can be noticed that the best response corresponds to the events where the muon's in-plane momentum is along the x axis, i.e., $|\phi| \sim 0, \pi$, while, the worst resolution is for muons in the ϕ bin 2–3 ($\times \pi/8$). This can be understood as follows. A study of the end-point positions of the tracks show that the worst resolution corresponds to the bin where most of the tracks end in the coil gaps which is a dead space. This can be seen in Fig. 3.6 where end- x values of muons, x_{end} , with input $|\phi|$ values in the bins (0–1, 1–2, 2–3, and 3–4) $\times \pi/8$ are shown (that for other values of ϕ are not shown here for clarity). It is seen that a large fraction of muons in the ϕ bin 2–3 $\times \pi/8$ end in the coil gap ($x = 400$ cm). In addition, the resolutions worsen somewhat for ϕ bins in which more number of tracks end in the support structures $x, y = 0, \pm 200, \pm 400, \dots$ cm, compared to other ϕ bins.

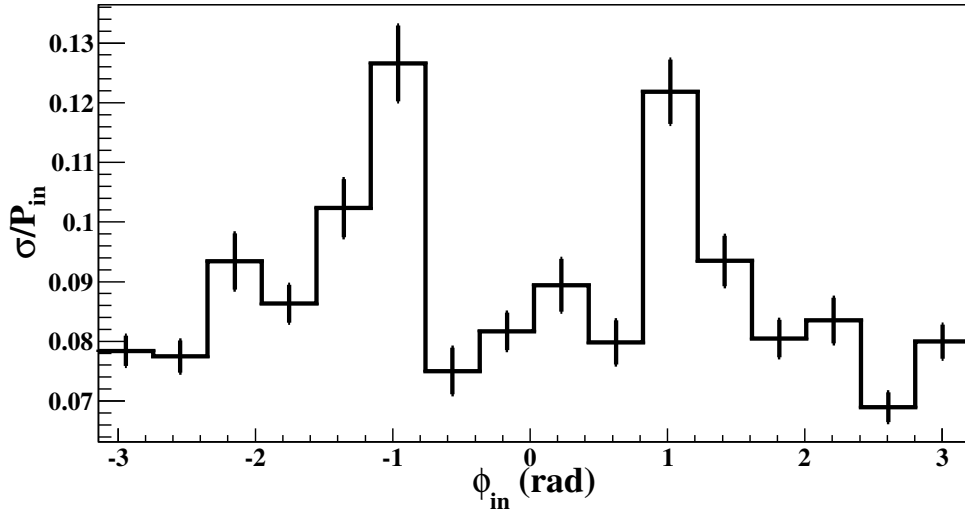


Fig. 3.5. Relative momentum resolution, σ/P_{in} , for muons with fixed momentum $(P_{\text{in}}, \cos \theta) = (5 \text{ GeV}/c, 0.65)$, plotted in bins of the azimuthal angle ϕ , with $\phi = 0$ corresponding to the x -direction. Note the y -axis does not begin with zero.

The effect of support structures is more in the case of smeared vertex events since the probability of the particles to see the support structure increases. This is discussed in Section 3.3.4 in detail.

In view of this, we separate our muon sample into four: Set I with $|\phi| \leq \pi/4$, Set II with $\pi/4 < |\phi| \leq \pi/2$, Set III with $\pi/2 < |\phi| \leq 3\pi/4$, and Set IV with $3\pi/4 < |\phi| \leq \pi$ (shown in Fig. 3.7). The response of the individual sets are shown in Fig. 3.8 for $P_{\text{in}} = 5 \text{ GeV}/c$ and $\cos \theta = 0.65$. While the width of the distributions for the four sets varies, the mean remains more or less the same. However, on separating these events, the fits to the data sets get improved, with acceptable χ^2 in each region.

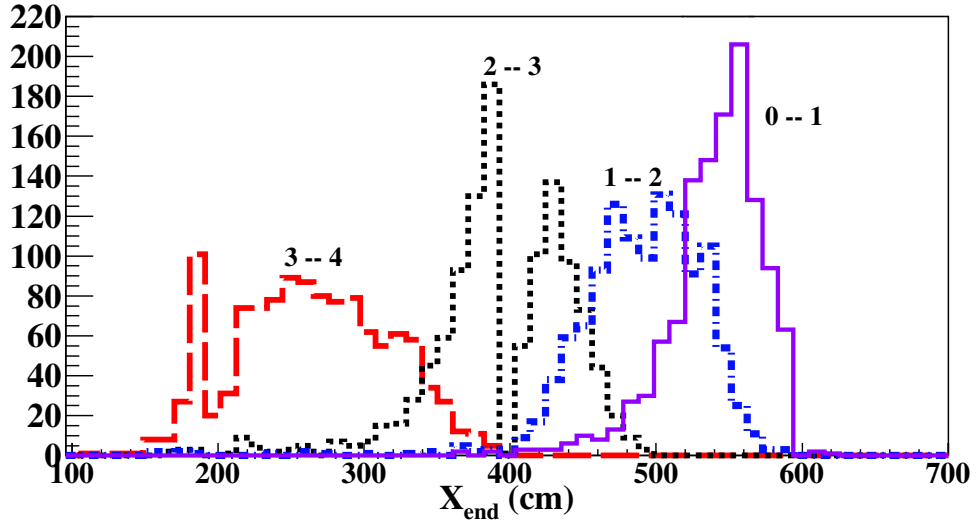


Fig. 3.6. Distributions of end x positions of the track for muons with fixed momentum $(P_{in}, \cos \theta) = (5 \text{ GeV}/c, 0.65)$ in four different bins of azimuthal angle.

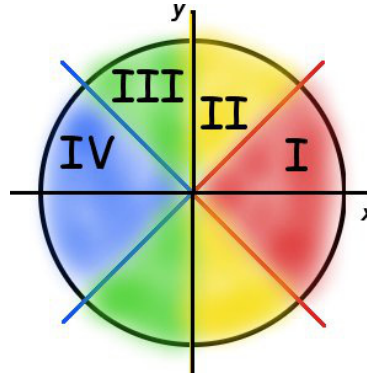


Fig. 3.7. Different ϕ regions

The momentum resolution is plotted for $\cos \theta = 0.65$ for momenta from 2–20 GeV/c in Fig. 3.9. It can be seen that initially (upto about 6 GeV/c), the resolution improves as momentum increases. This is because, at such small momenta, as the momentum increases, the number of RPC layers crossed by the muons also increases, thus increasing the number of layers with hits. The magnetic field causes appreciable bending so the accuracy of momentum reconstruction also increases. Thus the resolution improves.

As the input momentum increases further, the particle begins to exit the detector, so that only a partial track is contained in the detector. The part of the tracks inside the detector is relatively straight since the radius of curvature increases with momentum, which results in a poorer fit. Due to this the resolution then worsens as the input energy increases. In particular, muons in the ϕ regions II and III exit the detector from the y -direction earlier than those in regions I and IV due to the larger x dimension of

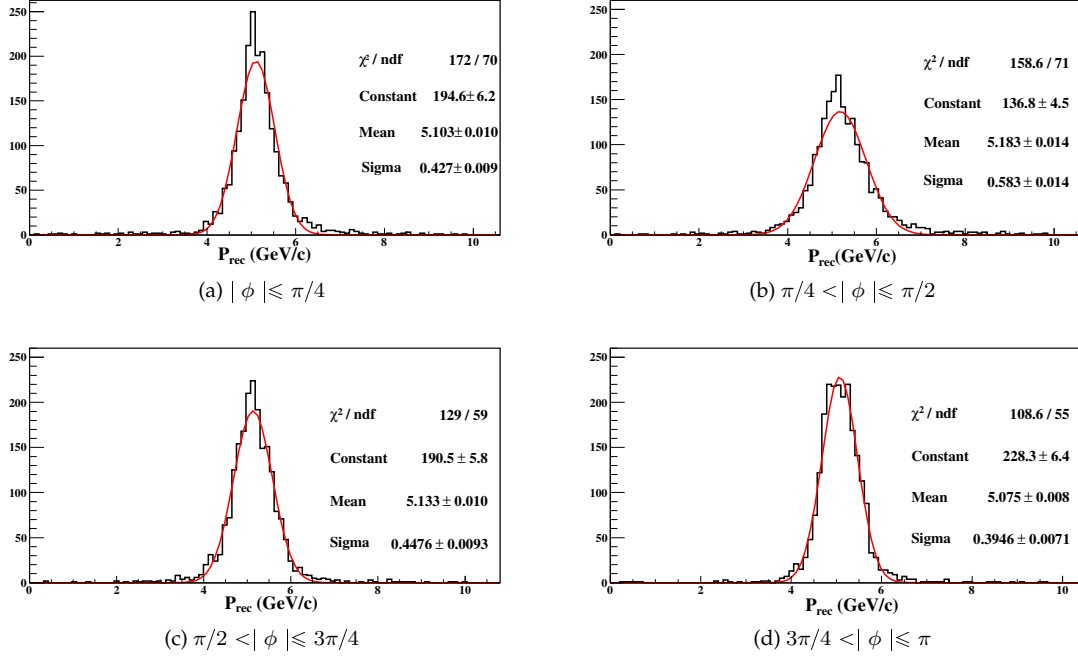


Fig. 3.8. Gaussian fits to momentum distributions for muons with fixed momentum $(P_{in}, \cos \theta) = (5 \text{ GeV}/c, 0.65)$ in four different bins of azimuthal angle as described in the text.

the detector. Hence, at higher energies, the resolutions in regions I and IV are better than those in regions II and III.

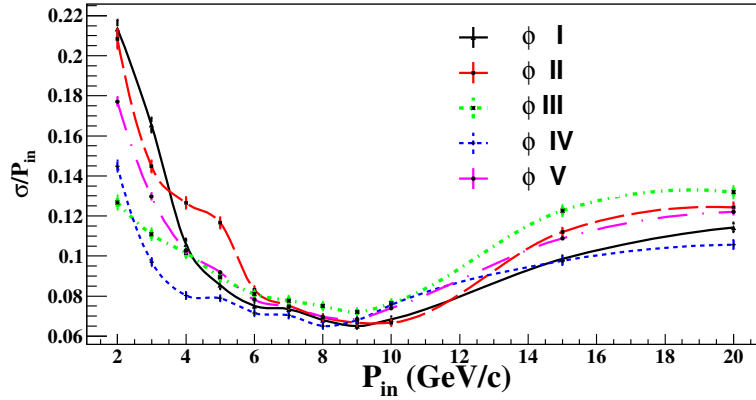


Fig. 3.9. Momentum resolution as a function of energy for $\cos \theta = 0.65$ in four different bins of azimuthal angle as described in the text. The curve labelled V corresponds to the resolution of the fully smeared ϕ data.

3.3 Smeared Vertex Muons

Having understood the response of the fixed vertex muons, the response of the muons with vertex uniformly located in the central region of central module is studied. The fixed energy muons are generated in a $8 \text{ m} \times 8 \text{ m} \times 10 \text{ m}$ volume of the central module where the magnetic field is uniform and maximum. For the analysis only events with

the z coordinate of the input vertex position to be $z_{\text{in}} \leq 400$ cm are selected. This is done to neglect the events which are very near to the edge and are mostly partially contained with only a small portion of the track inside the detector. Though the events are generated in the central region, the particles may travel outside this region where the magnetic field varies drastically and exit the detector altogether as well. The effect of the peripheral region of the detector, including the edge events, is studied separately [41].

The μ^- and μ^+ events are analyzed separately. It is observed that in the case of muons with fixed energy and angle, the results for μ^- is identical to that of μ^+ . It can be seen from the Fig. 3.10 that the track reconstruction efficiency ($\sim 95\%$) and the RMS values are nearly same for both cases. There may be slight differences for particle with very vertical zenith angle and high energy particles or horizontal zenith angle. Only results for μ^- are presented here later in the section.

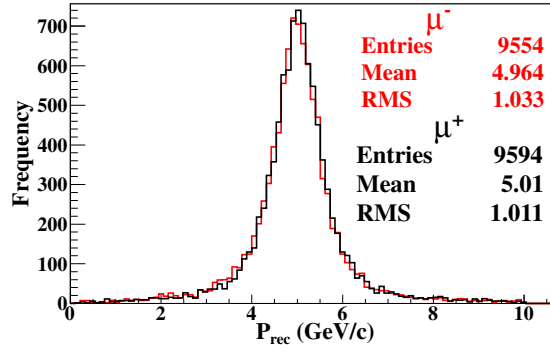


Fig. 3.10. Reconstructed momentum distributions for $(P_{\text{in}}, \cos \theta) = (5 \text{ GeV/c}, 0.65)$ smeared over the central volume of the detector for μ^- and μ^+ particles.

Fig. 3.11 shows the comparison of the histogram with fixed and smeared vertices.

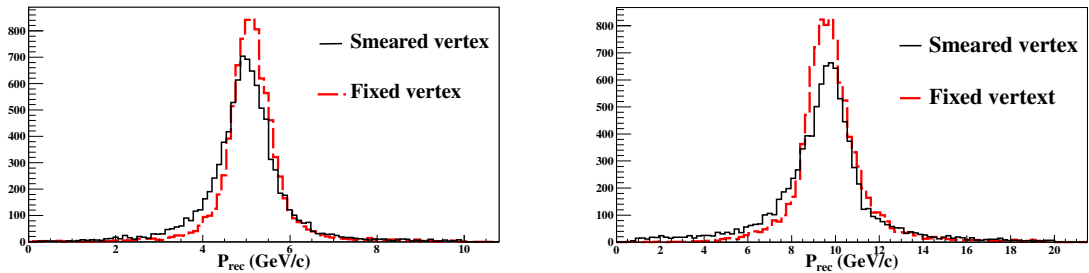


Fig. 3.11. Reconstructed momentum distributions for $(P_{\text{in}}, \cos \theta) = (5 \text{ GeV/c}, 0.65)$ (left panel) and for $(10 \text{ GeV/c}, 0.85)$ (right panel) are compared when the vertex is fixed around $(100, 100, 0)$ and smeared over the central volume of the detector.

Apart from the small shift in the mean, it is seen that the distribution is significantly

broadener in the case of smeared vertex events. The distribution of the smeared vertex events are not symmetric. This is the effect of detector support structures, gaps for magnetic field coils, etc. since the smeared vertex events pass through the dead spaces more compared to the fixed vertex events. Both fully contained and partially contained events (where only a part of the track of a muon is contained in the detector since it exits the detector without stopping) are considered for analysis. At low energies, the tracks are fully contained while particles start to leave the detector region by $P_{\text{in}} \sim 6$ GeV/c, depending on the location of the vertex.

Only those events that are reconstructed as single tracks as described earlier are selected. As before, the quality of fit further improves when the tracks are separated into different ϕ regions.

3.3.1 Track Reconstruction Efficiency

The track reconstruction efficiency is the ratio of events with successfully reconstructed track to the total number of events. In order to calculate this, all events with the quality of fit $\chi^2/\text{ndf} < 10$ are considered.

Except for very horizontal events with $\cos \theta < 0.4$, the track reconstruction efficiency for events with momentum $P_{\text{in}} > 2$ GeV/c is around 90% and rises to 95% by 5 GeV/c or more. For very horizontal events and low energy events, the number of layers with hits is very small because of which the track finder fails to find proper track candidate. This results in worsening the track reconstruction efficiency.

3.3.2 Direction (Up/Down) Reconstruction

The proper separation of the up-going and down-going events is crucial for the matter effect studies since only neutrinos coming from below experience matter effect. This can be achieved with the help of active detector having good time resolution. But still if the number of layers with hits are less, which happens for very horizontal or low energy events, the direction reconstruction fails.

The zenith angle is also the polar angle, θ , where $\cos \theta = 1(-1)$ indicates an up-going (down-going) muon. The reconstructed zenith angle distribution for muons with $P_{\text{in}} = 1$ GeV/c at small and large angles, $\cos \theta = 0.25$ and $\cos \theta = 0.85$, are shown in Fig. 3.12.

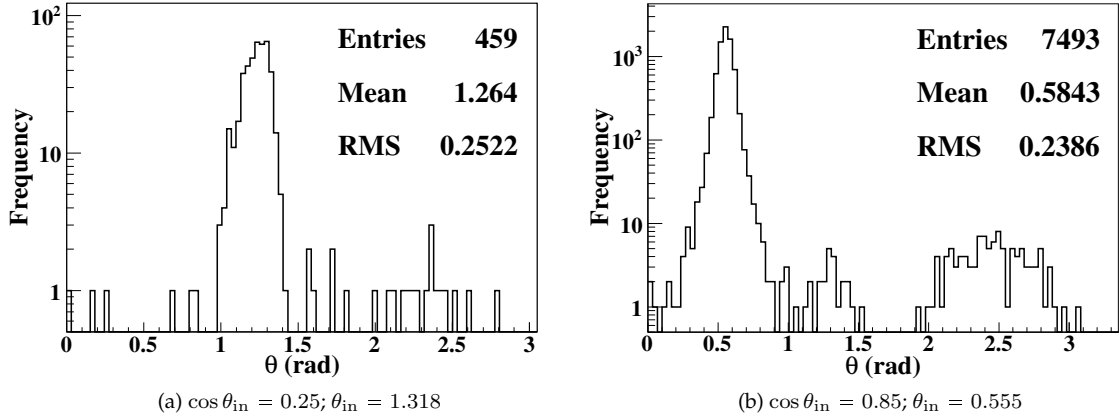


Fig. 3.12. Reconstructed angular distribution for $P_{\text{in}} = 1 \text{ GeV/c}$ at two different input angles.

It can be seen that a few events are reconstructed in the opposite direction to the input direction θ_{in} , i.e., with reconstructed zenith angle $\theta \sim \pi - \theta_{\text{in}}$. Since we are injecting only up-going muons, this means that the reconstructed muons are in the down-going direction. For muons with $P_{\text{in}} = 1 \text{ GeV/c}$ at large angles with $\cos \theta_{\text{in}} = 0.25$, this fraction is about 4.3%. But this improves for small angles. For example at $\cos \theta_{\text{in}} = 0.85$, it is about 1.5%. The fraction of events reconstructed in the wrong direction reduces sharply as energy increases; for example, this fraction is 0.3% for muons with $P_{\text{in}} = 2 \text{ GeV/c}$ at $\cos \theta_{\text{in}} = 0.25$. This is due to more number of layers with hits as energy increases.

The number of tracks reconstructed are very small at large angles because of the smaller number of layers with hits. We therefore restrict our analysis in what follows to $\cos \theta = 0.35$ or larger.

3.3.3 Zenith Angle Resolution

The distance traveled by neutrinos through Earth is directly related to their zenith angle. So the accurate determination of the angle is very necessary in order to understand neutrino oscillation. The zenith angle resolution is the width obtained when the reconstructed zenith angle distribution is fitted with Gaussian probability distribution functions (pdf). The reconstructed zenith angle distribution is shown in Fig. 3.13 for a sample input $(P_{\text{in}}, \cos \theta_{\text{in}}) = (5 \text{ GeV/c}, 0.65)$. It is seen that the distribution is very narrow, with a width less than a degree, indicating a good angular resolution for muons.

The θ resolution as a function of input momentum for different zenith angles is shown in Fig. 3.14. The resolution rapidly improves with input momentum, being better than a degree for all input angles for $P_{\text{in}} > 4 \text{ GeV/c}$. Beyond 10 GeV/c , the

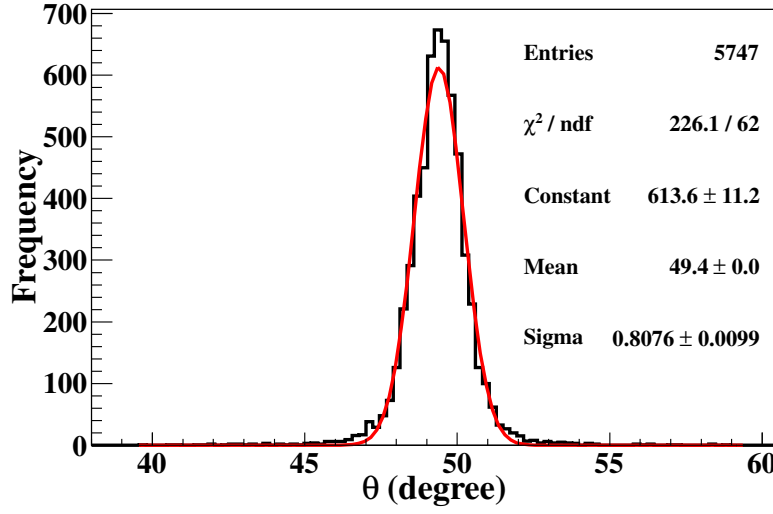


Fig. 3.13. Reconstructed angular distribution for input $(P_{\text{in}}, \cos \theta_{\text{in}}) = (5 \text{ GeV}/c, 0.65)$; $\theta = 49.46^\circ$.

curves approximately coincide for all the angles. As the momentum of the particle increases, the number of layers with hits increases. This helps in reconstructing the angle accurately from the initial part of the track. Though the particle goes out of the detector as energy increases, it does not affect the angle determination.

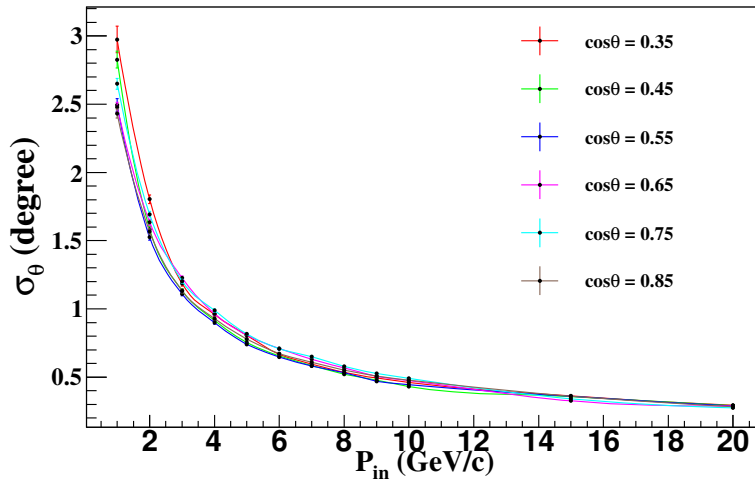


Fig. 3.14. Angular resolution in degrees as a function of input momentum.

3.3.4 Muon momentum resolution

The momentum resolution is determined as described earlier in Section 3.2.1. The reconstructed momentum distributions for low energy events show a clear asymmetric tail (as shown in Fig. 3.15) and so are fitted with a convolution of Landau and Gaussian probability distribution functions (pdf). The momentum distributions at low energy

are broader and there is a shift in the mean. For muons with $P_{in} \geq 2$ GeV/c, fits are with purely Gaussian pdf. In the case of Landau-Gauss fits, the width is defined as $\sigma \equiv \text{FWHM}/2.35$, where FWHM = Full Width at Half Maximum, in order to compare with the Gaussian fits at higher energies, where the square root of the variance or the RMS width equals FWHM/2.35.

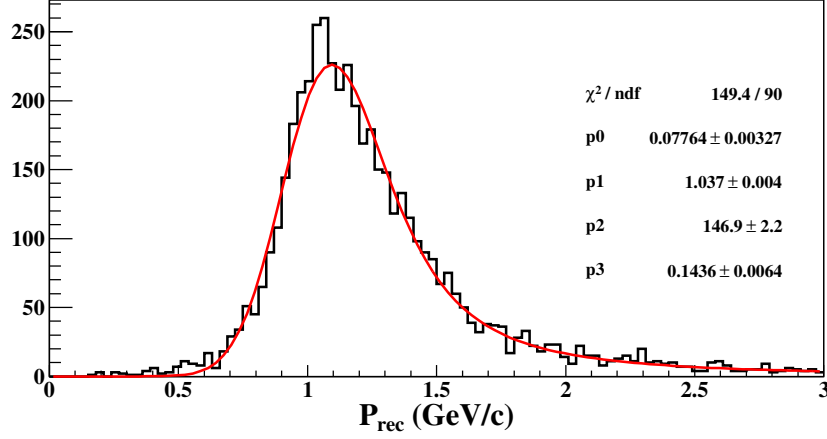


Fig. 3.15. Momentum distributions for $(P_{in}, \cos \theta) = (1 \text{ GeV/c}, 0.65)$ fitted with Landau convoluted Gaussian; this fits better than a pure Gaussian at lower energies, $P_{in} \leq 2 \text{ GeV/c}$.

Though the histograms at higher energies show no asymmetric tails, they fit poorly to Gaussian distributions, with $\chi^2/\text{ndf} \geq 6$ or more as seen from Fig. 3.16. This is because of the presence of detector dead spaces and the effect of magnetic field as discussed in Section 3.2.1. These dead spaces generically worsen the quality of reconstruction.

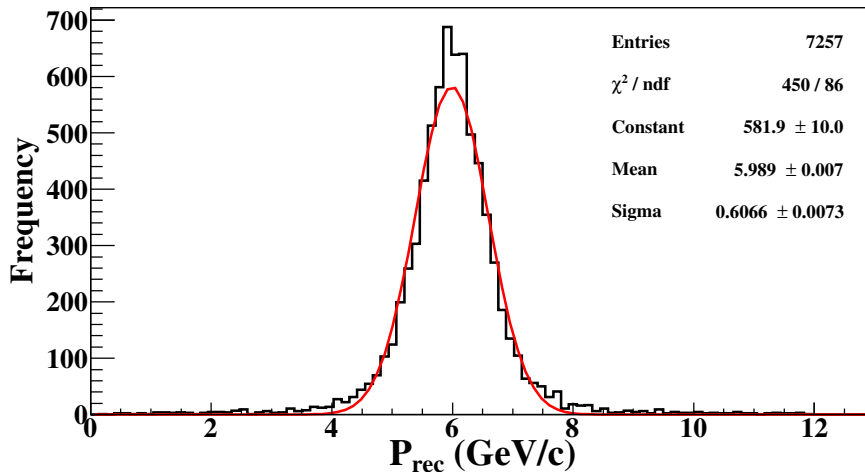


Fig. 3.16. Momentum distributions for $(P_{in}, \cos \theta) = (6 \text{ GeV/c}, 0.65)$ fitted with Gaussian

The resolution as a function of input momentum (or energy) and polar (here also the zenith) angle has a similar behaviour to that of the case of fixed-vertex muons, but is somewhat worse. The effect of the presence of the support structure is more in the case smeared vertex events.

As discussed in the Section 3.2.1, different ϕ regions have different detector response. Therefore the momentum resolution is calculated for different ϕ region separately.

3.3.4.1 Muon Resolution in Different Azimuthal Bins

As discussed earlier, the muon sample is separated into four ϕ bins: Bin I with $|\phi| \leq \pi/4$, Bin II with $\pi/4 < |\phi| \leq \pi/2$, Bin III with $\pi/2 < |\phi| \leq 3\pi/4$, and Bin IV with $3\pi/4 < |\phi| \leq \pi$.

Fig. 3.17 shows the Gaussian fits for the reconstructed histogram of the reconstructed momentum P_{rec} for input values of $P_{\text{in}} = 4 \text{ GeV}/c$ and $\cos \theta = 0.65$ in different ϕ regions. When separated into different ϕ regions, the quality of the fits improves considerably as can be seen from the reduced chi-square.

The momentum resolution as a function of input momentum for different values of $\cos \theta$ in the different ϕ regions is shown in Fig. 3.18. The behaviour is similar to that with fixed-vertex muons. The variation of resolution with P_{in} for a range of $\cos \theta$ in different ϕ bins are shown in Fig. 3.19.

At lower energies the resolution improves as $\cos \theta$ increases, as expected, but at higher energies the dependence is complicated. For instance, at higher energies, the muons injected at larger zenith angles in ϕ regions I and IV have better resolutions than their counterparts at more vertical angles (as an example, $\cos \theta = 0.45$ versus $\cos \theta = 0.85$) because larger portions of the tracks, being more slanted, are still contained within the detector. In contrast in ϕ regions II and III, muons with larger zenith angles have worse resolution than those at smaller zenith angles because the former exits the detector from the y direction and are partially contained.

In general, at angles larger than about 75° ($\cos \theta = 0.25$), the resolution is relatively poor since there are several times fewer hits than at more vertical angles. This is due

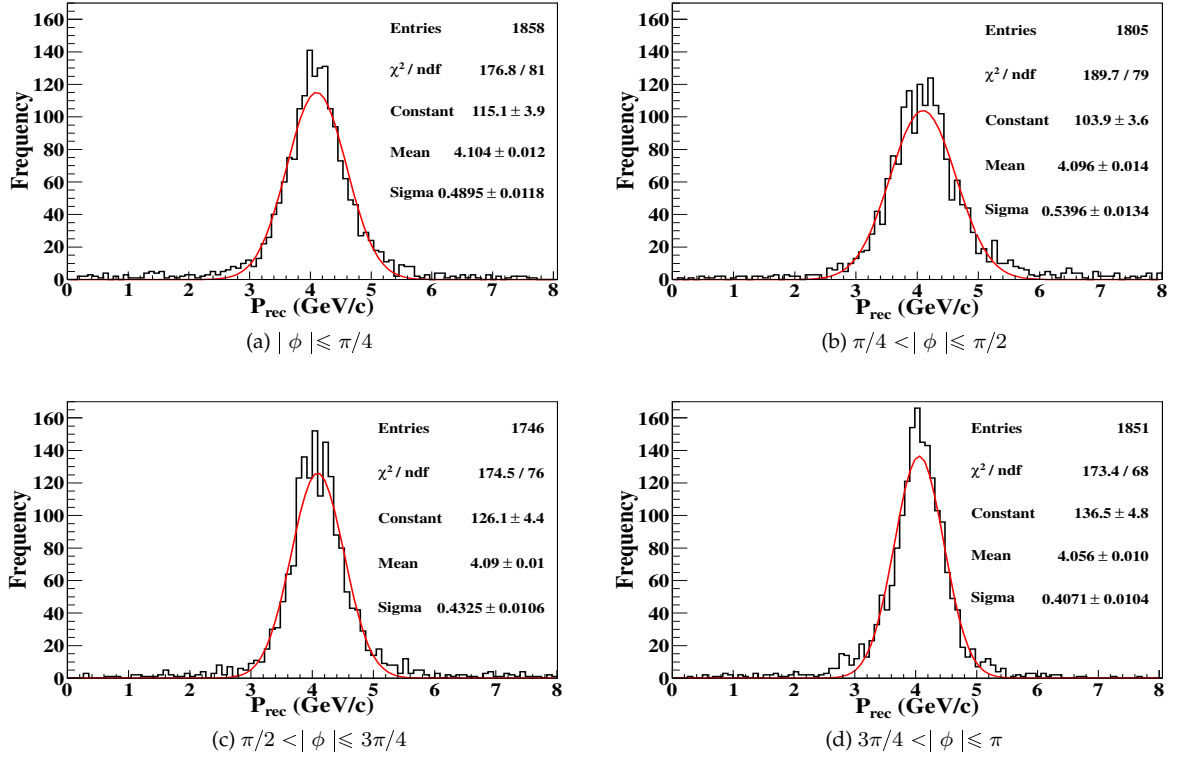


Fig. 3.17. Reconstructed momentum distribution for $(P_{\text{in}}, \cos \theta) = (4 \text{ GeV/c}, 0.65)$ in different ϕ bins, fitted with a Gaussian distribution.

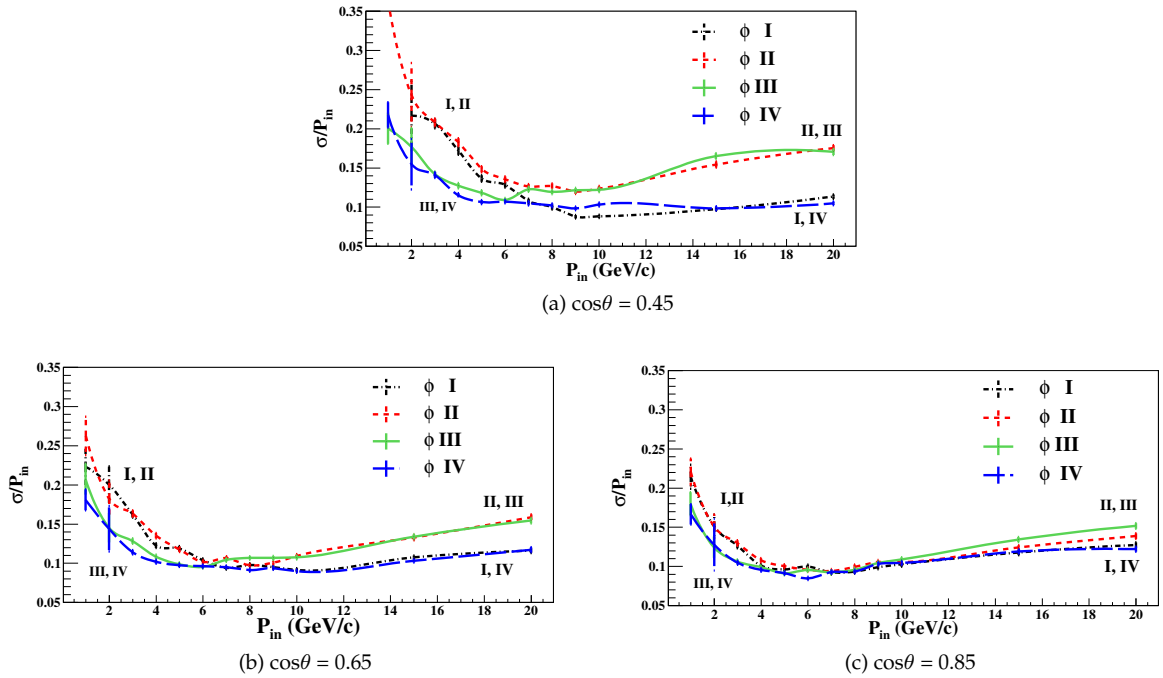


Fig. 3.18. Muon resolution as a function of muon energy for different (fixed) values of $\cos \theta = 0.45, 0.65, 0.85$, from top to bottom respectively, shown for different ϕ regions.

to the detector geometry, with its horizontal layers of iron plates where most of energy is lost. Hence ICAL is not so sensitive to very horizontal muons.

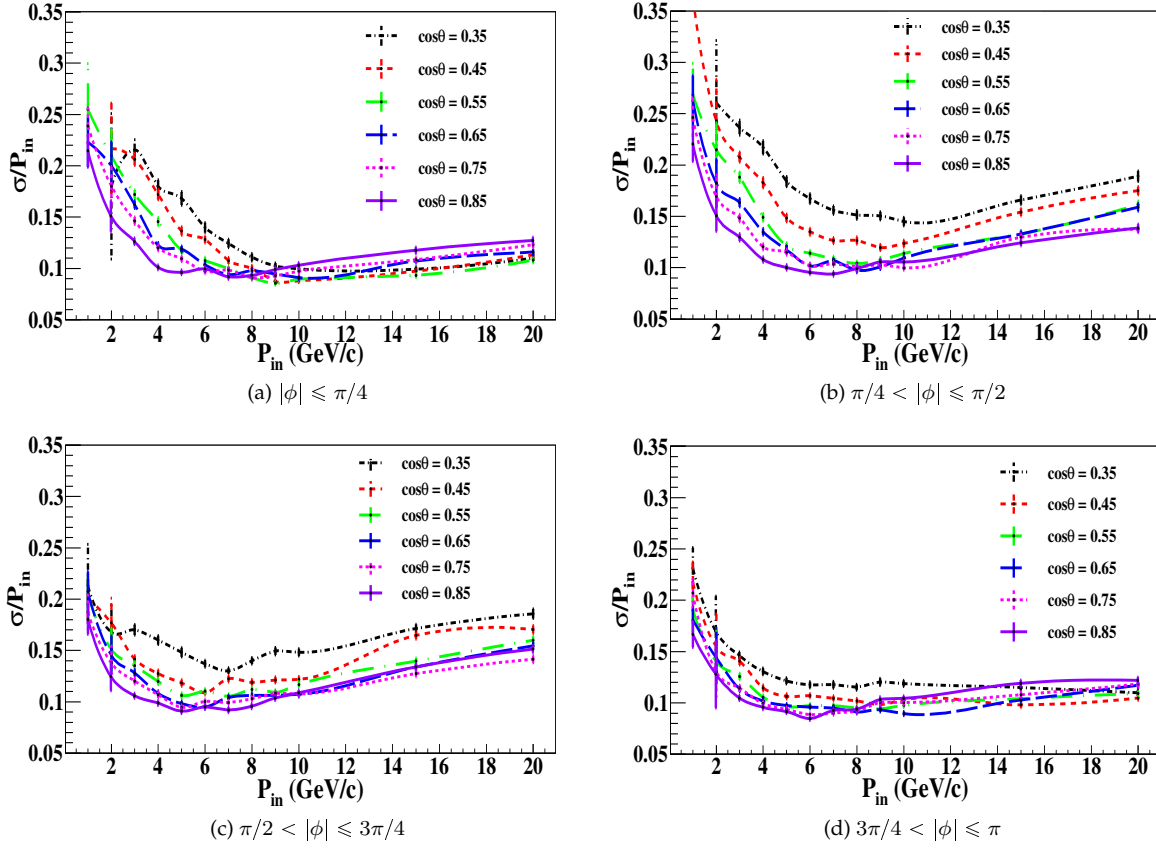


Fig. 3.19. Muon resolution as a function of input momentum and $\cos \theta$, in different bins of azimuthal angle ϕ .

The other parameters of interest such as reconstruction efficiency and charge identification efficiency are not very sensitive to the azimuthal angle; hence, all the ϕ bins are combined and calculated ϕ -averaged quantities.

3.3.5 Mean Shift

The mean of the reconstructed momentum (P_{rec}) distribution is almost independent of both the polar and azimuthal angles. Fig. 3.20 shows the shift in the mean of reconstructed momentum (shift = $P_{in} - P_{rec}$), as a function of the input momentum.

The shift can arise due to multiple scattering, effect of magnetic field etc., and is roughly linear beyond a few GeV/c. For a particular energy value, the mean shifts for all the zenith angle bins are almost same though as energy increases the differences are more visible.

3.3.6 Momentum Reconstruction Efficiency

Since neutrino cross sections are very small, event rates are small. So it is important to reconstruct all the possible events. The reconstruction efficiency (ϵ_{rec}) is defined as the

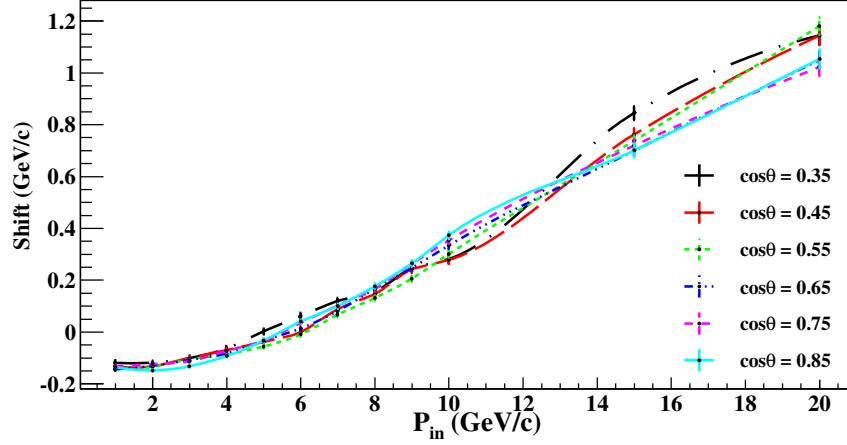


Fig. 3.20. Shift in the mean of reconstructed momentum as a function of the input momentum.

ratio of the number of reconstructed events, n_{rec} (calculated with cuts, irrespective of charge), to the total number of generated events, N_{total} .

$$\epsilon_{\text{rec}} = \frac{n_{\text{rec}}}{N_{\text{total}}}, \quad (3.3.1)$$

$$\text{and its error, } \delta\epsilon_{\text{rec}} = \sqrt{\epsilon_{\text{rec}}(1 - \epsilon_{\text{rec}})/N_{\text{total}}}.$$

Fig. 3.21 shows the muon reconstruction efficiency as a function of input momentum for different $\cos \theta$ bins. It is seen that the efficiency of momentum reconstruction depends on the energy of the incident particle, the angle of propagation etc. It was also found to depend on the strength of the magnetic field [30].

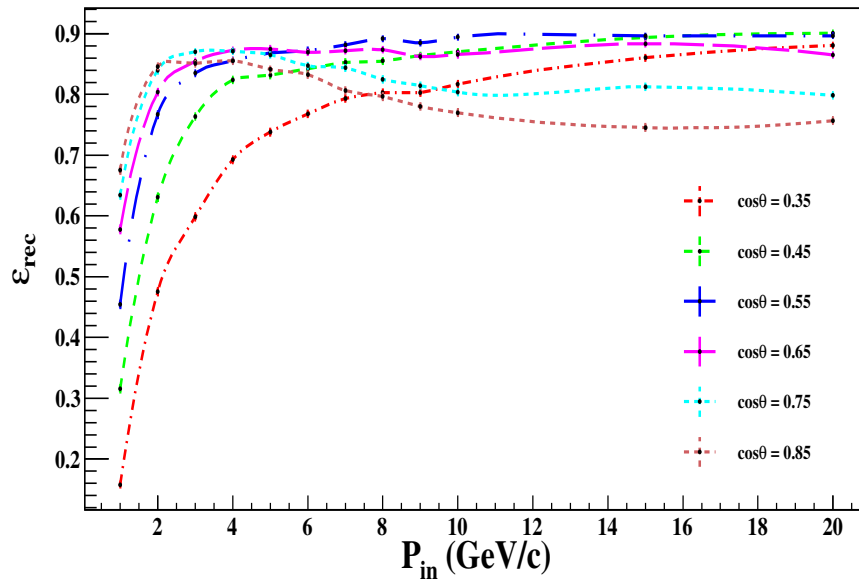


Fig. 3.21. Reconstruction efficiency as a function of the input momentum for different $\cos \theta$ values.

For momentum values below 4 GeV/c, as the input momentum increases, the reconstruction efficiency increases for all angles. This is due to the increase in the number of layers with hits as the momentum increases. At larger angles, the reconstruction efficiency for small energies is smaller compared to vertical angles since the number of layers with hits for reconstructing tracks is less. But as the input energy increases, since the particle crosses more number of layers, the efficiency of reconstructing momentum also increases and becomes comparable with vertical angles. At higher energies the reconstruction efficiency becomes almost constant. The decrease in efficiency at high energies for vertical muons is due to the partially contained tracks as well as the requirement of single track being reconstructed.

3.3.7 Relative Charge Identification Efficiency

The charge identification of the particle plays a crucial role in the determination of the neutrino mass hierarchy since the determination of mass hierarchy requires the separation of neutrino events from anti-neutrino induced events and these have different matter effects as they propagate through the Earth. The charge of the particle is determined from the direction of curvature of the fitted track in the magnetic field. Relative charge identification efficiency is defined as the ratio of number of events with correct charge identification, n_{cid} , to the total number of reconstructed events, i.e.,

$$\epsilon_{\text{cid}} = \frac{n_{\text{cid}}}{n_{\text{rec}}} , \quad (3.3.2)$$

with error, $\delta\epsilon_{\text{cid}} = \sqrt{\epsilon_{\text{cid}}(1 - \epsilon_{\text{cid}})/N_{\text{rec}}} .$

Fig. 3.22 shows the relative charge identification efficiency as a function of input momentum for different $\cos\theta$ values.

The muon undergoes multiple scattering during propagation in the detector. For muons with small momentum, since the number of layers with hits is small, this may lead to an incorrectly reconstructed direction of bending, which results in the wrong charge identification. An error in the reconstruction of the up/down direction also results in wrong charge identification. Hence the charge identification efficiency is relatively poor at lower energies. As there are more number of layers with hits as the energy increases, the charge identification efficiency also improves. Beyond a few GeV/c, the charge identification efficiency becomes roughly constant, about 98%.

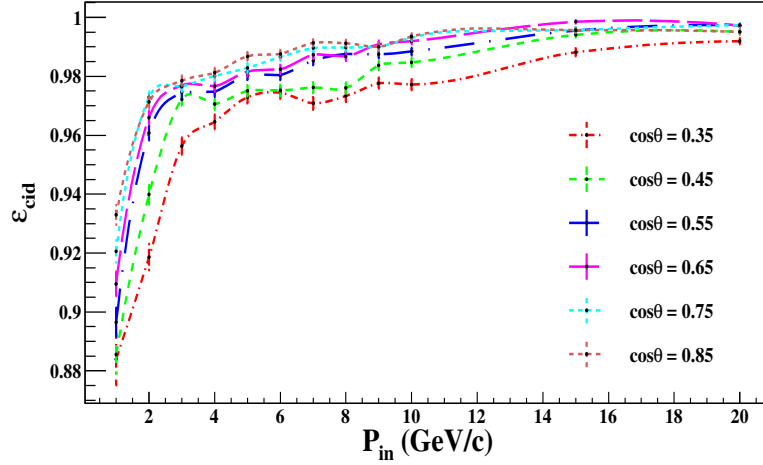


Fig. 3.22. The relative charge identification efficiency as a function of the input momentum for different $\cos \theta$ values. Note that the y -axis range is 0.87–1 and does not start from zero.

3.4 The muon response at other energies

The atmospheric neutrino flux peaks around few hundreds of MeVs and falls very sharply above 1 GeV. Hence there are a large number of events at low energies, ie., for $E \leq 1$ GeV. In order to include these events in the oscillation physics studies, the response of muons is studied at these lower energies. A typical result is shown in Fig. 3.23 (left panel) for $(P_{in}, \cos \theta) = (0.6 \text{ GeV}/c, 0.65)$. Here the momentum is determined from the range calculation rather than the Kalman Filter since the track is very short. While the charge identification efficiency, calculated using Kalman Filter, is small, 70%, there is still reasonable sensitivity at these values with the large number of events compensating for the smaller reconstruction efficiency.

In addition the study of muon charge ratio from high energy cosmic ray muons include muon with energy upto 100 GeV and beyond. Since all these high energy muons are not stopped inside ICAL, only partially contained tracks are available for analysis. This may reduce the charge identification efficiency. Fig. 3.23 (right panel) shows a typical result for $(P_{in}, \cos \theta) = (50 \text{ GeV}/c, 0.65)$. It is seen that μ^- and μ^+ show similar response with a reconstruction efficiency of $\sim 70\%$. The charge identification efficiency is found to be about 98% at this energy.

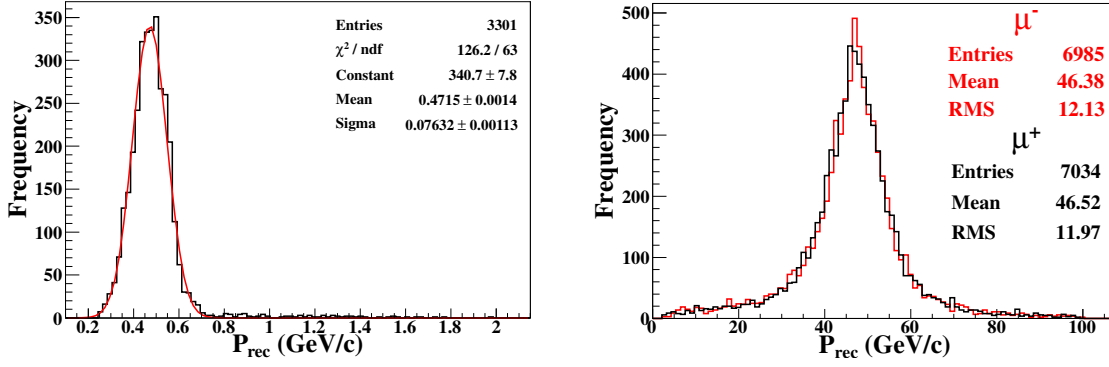


Fig. 3.23. Reconstructed momentum distributions for $(P_{\text{in}}, \cos \theta) = (0.6 \text{ GeV/c}, 0.65)$ (left panel) and for $(50 \text{ GeV/c}, 0.65)$ (right panel) with the vertex smeared over the central volume of the detector.

3.5 Peripheral and Side region

The response of the peripheral and side region have also been studied in detail in a separate analysis [41]. Since part of these results are used in Chapter 4 to analyze the muon charge ratio from high energy muons, this section is included for completeness. The events are generated in the side and peripheral region. Both fixed vertex and smeared vertex results are analyzed. The peripheral region is affected by the varying magnetic field and edge effects. In both side and peripheral regions the strength of the magnetic field is less compared to central region. Apart from the cuts used in the analysis of central region data, additional cuts are needed to select the events. It was found that the partially contained events were poorly reconstructed. Sometimes such events are reconstructed with energies less than the actual energy causing a low energy tail in the distribution. In order to remove such events, a cut on N_{hits} is used (Fig. 3.24). This will be useful for the study of high energy cosmic ray muons which will be presented in next chapter.

The results in the side and peripheral regions are worse compared to the central region. The angular resolution in side and peripheral region is comparable with that obtained in the central region. As expected the central region gives the best momentum resolution compared to side and peripheral regions, whereas side region is slightly better than peripheral region. At very low energies the momentum resolution of all the regions are comparable since the events are mostly fully contained. The reconstruction efficiency is comparable for side and peripheral regions but $\sim 10\%$ less compared to central region. The relative charge identification efficiency is nearly similar for central

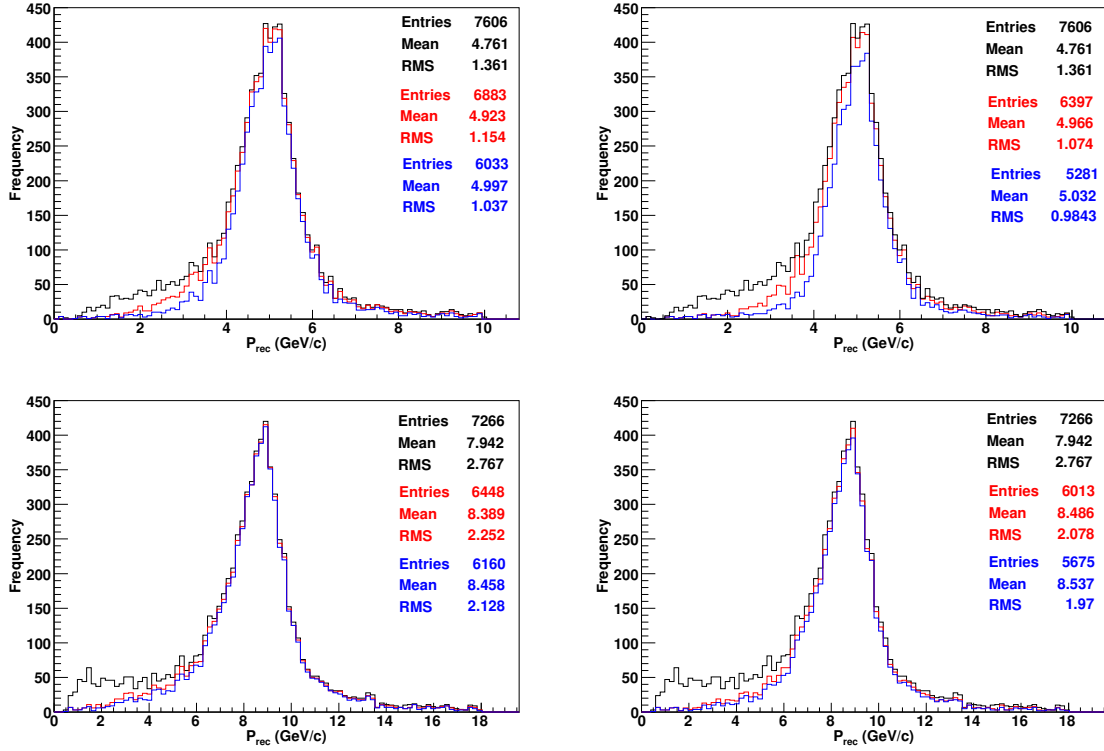


Fig. 3.24. Top (bottom) figures show the reconstructed momenta P_{rec} using selection criteria $N_{hits} > n_0$ for partially contained events in the peripheral region with $(P_{in}, \cos \theta) = (5 \text{ GeV/c}, 0.65)$ (top) and $(9 \text{ GeV/c}, 0.85)$ (bottom) with $n_0 = 15$ (20) in the left (right) figure. Fully contained events have no N_{hits} constraint. In each figure, the black curve is without constraints on N_{hits} , red is with $N_{hits} / \cos \theta > n_0$ and blue is for $N_{hits} > n_0$.

and side regions for $E < 10 \text{ GeV}$, but for peripheral region it is 1–2% less.

3.6 Summary

When the muon neutrino interacts via charge current interaction, muons and often associated hadrons are produced. In order to understand the neutrino properties, the neutrino energy and angle have to be reconstructed accurately. The hadrons shower in the detector and therefore the individual hadrons cannot be reconstructed. The ICAL detector is more sensitive to muons. It is important to understand the response of muons.

First the response of fixed energy muons is studied. The muon with fixed momenta from 1–20 GeV/c and with direction $\cos \theta > 0.25$ are generated and propagated through ICAL using a GEANT4 based code in which ICAL geometry is described. In the current study, the muons are generated in the central region of the central module where the magnetic field is maximum and uniform. Since it is found that the μ^+ and

μ^- give similar results with these inputs, only μ^- results are presented. Both fully contained and partially contained (with muons exiting the detector) events were analyzed.

In order to understand the behaviour of muons, the fixed vertex events are studied first. The effect of the support structure and the magnetic field can be understood clearly with the fixed energy events where the fluctuations are less. Having understood the fixed vertex results, the smeared vertex events are studied.

It was found that clean tracks were obtained in the detector for muons with momenta from few to 10s of GeV/c in all zenith angles smaller than $\cos \theta = 0.25$. The momentum of the muons was reconstructed using a Kalman filter based algorithm that makes use of the bending of the tracks in the magnetic field. Hence the presence of the magnetic field is crucial to this study.

Different ϕ regions were analyzed separately in order to find the dependence of resolution on azimuthal angle. The presence of the magnetic field as well as the coil gaps and support structures break the azimuthal symmetry. Although neutrino oscillations as well as the neutrino flux (for energies considered here) are independent of ϕ , a strong east-west effect ($\phi = 0$ versus $\phi = \pi$) being visible [42] only at sub-GeV energies. Hence it was important to understand the response of muons in different azimuthal regions.

The direction and momentum resolution, reconstruction efficiency, charge identification efficiency and angular resolution of muons are studied. The momentum resolution was about 9–14% and the reconstruction efficiency was about 80% in most of the regions. The angular resolution was found to be very good, being better than a degree for all angles for momenta greater than about 4 GeV/c. The direction (up/down) discrimination was also very good. The relative charge identification efficiency was also about 98% over this range.

The effect of magnetic field strength on muon response was briefly studied using maximum value of magnetic fields of 0.7 T, 1.28 T, 1.5 T and 1.9 T. The momentum resolution and the efficiencies were found to be nearly the same for all the field strengths beyond 1 T. This behaviour was studied in detail and completed later by S. P. Behera et. al [30].

In summary, ICAL simulations show that the detector has a good response to muons, including identifying their momentum, direction, and charge, with good ef-

ficiency. These results have already been used to perform the physics analysis of atmospheric neutrinos with ICAL [37], [38].

Atmospheric Muon Charge Ratio using ICAL detector

4.1 Introduction

Cosmic rays are high energy particles that originate in outer space. They get accelerated in the intergalactic space and strike the earth's atmosphere from all directions. Cosmic rays are mostly nuclei of atoms such as H, He and heavier elements. They also include e^+ , e^- and other subatomic particles. The energy of cosmic rays varies from few MeVs to TeVs and beyond.

The primary cosmic rays interact with the atoms and nuclei in the atmosphere. The hadrons undergo strong interactions with the atmospheric nuclei such as nitrogen and oxygen and produce hadron showers containing mainly π s and K s. Out of the secondary particles π s are the most abundant due to its lower mass.

If the secondary particles have sufficient energy they initiate new interactions. The unstable particles like π s and K s decay through the channels,

$$\pi^+ \rightarrow \mu^+ \nu_\mu ,$$

$$\pi^- \rightarrow \mu^- \bar{\nu}_\mu ,$$

$$K^+ \rightarrow \mu^+ \nu_\mu ,$$

$$K^- \rightarrow \mu^- \bar{\nu}_\mu .$$

Since muons are minimum ionizing particles they can penetrate large amounts of matter whereas weakly interacting neutrinos pass through matter with hardly any interaction. Muons are the most abundant charged particles at the sea level. They lose about 2 GeV before reaching the ground. The mean energy of the muons at the sea level is about ≈ 4 GeV. The vertical muon intensity at the sea level is about $1 \text{ cm}^{-2} \text{ min}^{-1} \text{ sr}^{-1}$ for horizontal detectors. These muons have energies ranging from MeVs to TeVs. The low energy muons decay into electrons and neutrinos:

$$\begin{aligned}\mu^+ &\rightarrow e^+ \nu_e \bar{\nu}_\mu, \\ \mu^- &\rightarrow e^- \bar{\nu}_e \nu_\mu.\end{aligned}$$

The knowledge of cosmic ray muon flux plays a significant role in understanding of atmospheric neutrinos, chemical composition of primary cosmic rays, etc.

Since the primary cosmic rays mainly contain positively charged particles (protons), there are more positive π s and K s. The charge ratio of π s (π^+/π^-) is estimated to be 1.27 [43]. The K^+/K^- ratio is also larger than 1, mainly due to associated production. The study of the atmospheric muon charge ratio can help in improving cosmic ray air shower models and hence better determination of the atmospheric neutrino flux, which is a crucial input to the study of neutrino oscillations through atmospheric neutrinos.

The atmospheric muon charge ratio has been measured by different groups. All the published vertical atmospheric muon fluxes above 10 GeV have been collected and studied in Ref. [44] and the charge ratio was found to be $1.268 \pm [0.008 + 0.0002 \frac{p}{\text{GeV}}]$ with 68% CL in the momentum range 10 – 300 GeV. The MINOS Near detector at a depth of 225 mwe (metre water equivalent) has also measured this charge ratio [45]. Using 301 days data, the charge ratio was found to be $1.266 \pm 0.001(\text{stat.})_{-0.014}^{+0.015}(\text{syst.})$; however, it was also observed that the charge ratio increased as surface energy increased. The absolute muon flux from 20 GeV—3 TeV was measured with the L3 Magnetic muon spectrometer and the average muon charge ratio is found to be $1.285 \pm 0.003(\text{stat.}) \pm 0.019(\text{syst.})$ [48]. The MINOS Far detector which at a depth of 2070 mwe measured a somewhat higher charge ratio of $1.374 \pm 0.004(\text{stat.})_{-0.010}^{+0.012}(\text{syst.})$ for muons with surface energy in the range 1–7 TeV [46]. The OPERA underground detector has also observed an increase in charge ratio with underground muon momentum [47]. This increase has been attributed to the opening up of the K production and decay channel and can thus help to determine details of these processes. It was also observed [49] from MINOS data analysis that the ratio can be more properly described as a function of the product $(E_\mu^{\text{surface}} \cos \theta)$ than of E_μ^{surface} alone although this may be a feature of the location of the detector in a mine with a flat topography above it. They also studied the energy loss of the muon as it propagated through the Earth and its dependence on the sign of its charge.

The ICAL detector is optimized to study muons produced in neutrino interactions. Since it is a magnetized detector the charge of the muon can be determined. The de-

tector can also be utilized for the study of cosmic ray muons. Due to the depth of the INO cavern at which the ICAL detector will be located, it can be used to study the the atmospheric muon charge ratio at high energies and thus complement the existing measurements.

4.2 Cosmic ray muon flux at sea level

The surface muon flux can be described by Gaisser's formula [50],

$$\frac{dN_\mu}{dE_{\mu,0}d\Omega} \approx \frac{0.14E_{\mu,0}^{-2.7}}{\text{cm}^2.\text{sec.sr.GeV}} \times \left\{ \frac{1}{1 + \frac{1.1E_{\mu,0} \cos \theta_z}{\epsilon_\pi}} + \frac{\eta}{1 + \frac{1.1E_{\mu,0} \cos \theta_z}{\epsilon_K}} \right\}. \quad (4.2.1)$$

This parametrization is valid when the decay of the muon is negligible and the curvature of earth can be neglected (zenith angle $\theta < 70^\circ$). The two terms in the brackets describe the contribution from pions and kaons respectively, that is, from production processes, $C + A \rightarrow M + X$, where C is a cosmic ray primary, mostly p or n , A is an average air nucleus of mass about $A \sim 14.5$, M is a meson, either π or K , and X can be anything else. The nucleon mean free path in air is $\lambda_N \sim 80\text{g/cm}^2$ or about 650 m. Hence cosmic primaries interact over most of the thickness of the atmosphere. These mesons can either interact or decay; the choice is determined by the critical energy, which is determined by the path length traversed by these mesons. The decay mean free path of the meson M in units of slant depth is given by

$$d_M = \gamma(c\tau_M) \frac{X}{h_0/\cos \theta}, \quad (4.2.2)$$

where γ is the Lorentz factor, $\gamma = E/m_M c^2$, for a meson M with energy E in the laboratory frame and mass M_M , and τ_M is its average life-time in its rest frame. The quantity X is the atmospheric depth (measured in g/cm^2 or in cm when multiplied with the density of air) or the total density-weighted height of the atmosphere above the observational level, h :

$$X = \int_h^\infty \rho(h')dh' \approx X_0 \exp(-h/h_0), \quad (4.2.3)$$

where ρ is the height dependent density of the atmosphere, $X_0 = 1030\text{g/cm}^2$ is the atmospheric depth at sea level and $h = 6.4\text{ km}$ is the scale height of the atmosphere [51, 52].

The factor $1/\cos \theta$ rescales the scale height to $h_0/\cos \theta$ which is the equivalent scale

height for a particle travelling at a zenith angle θ , valid in a flat-Earth approximation, that is, for $\theta \lesssim 70^\circ$.

Hence the decay mean free path can be expressed as

$$d_M = \frac{E}{\epsilon_M} X \cos \theta , \quad (4.2.4)$$

where the ϵ_M , $M = \pi, K$, are the critical energies at which the interaction probability of the meson with the atmosphere become equal to their decay probability,

$$\epsilon_M = \frac{m_M c^2 h_0}{c \tau_M} . \quad (4.2.5)$$

Sometimes $\epsilon_M / \cos \theta$ are referred to as the zentih-angle dependent critical energies. When the value of $E_{\mu}^{surface} \cos \theta$ exceeds ϵ_K , the contribution of kaons to the muon flux, and therefore to the charge ratio, will be more significant. Using the standard values of masses and lifetimes of π and K , we get $\epsilon_{\pi} \sim 115$ GeV and $\epsilon_K \sim 850$ GeV.

The parameter η in Eqn. 4.2.1 is related to the relative contribution to muon decay from K and π decay and is estimated to be around $\eta = 0.054$. In particular the value of η depends on the contribution to kaon production from associated production. This in turn affects the value of the muon charge ratio at high energies. We will discuss this in detail in the following section.

4.2.1 Kaons and the rise of the muon charge ratio

It is well-established that the rise of the muon charge ratio at high energies is due to the increasingly dominant contribution of K meson decay beyond $E \cos \theta \gtrsim \epsilon_K$. Just as in the case of charged pions, K^+ exceed K^- since there are more protons than neutrons in the primary cosmic ray composition. However, in addition, there is an extra contribution from kaons that arises due to associated production:

$$p + A \rightarrow K^+ + \Lambda + X , \quad (4.2.6)$$

where A is an average air nucleus as before, whose interaction with protons in the cosmic ray gives rise to K^+ through the underlying quark process: $(uud) \rightarrow (u\bar{s}) + (uds)$. The analogous interaction with neutrons however, does not give rise to K^- but to K^0 :

$$n + A \rightarrow K^0 + \Lambda + X , \quad (4.2.7)$$

through the undeg quark process: $(udd) \rightarrow (d\bar{s}) + (uds)$. The production of K^- (containing the strange quark rather than the strange anti-quark would require the associated production of an anti-baryon which is suppressed. Due to this, there is an increased excess of μ^+ , arising when these excess K^+ decay, compared to μ^- in the cosmic ray secondaries. The measurement of the muon charge ratio at high energies is therefore sensitive to this associated production cross section, which appears in η through the term Z_{pK^+} [51] which is the spectrum-weighted moment of the inclusive cross section for this process.

Measurements at MINOS seem to indicate that the anticipated value of $Z_{pK^+} = 0.0090$ are too large and that a value of $Z_{pK^+} = 0.0079 \pm 0.0020$ is a better fit to the data. Hence it is crucial to measure the muon charge ratio at high energies (of a TeV or more) to better determine this ratio.

In addition, the kaon production (and decay) processes are also important from the point of view of the atmospheric neutrino spectrum. Due to the kinematical differences between a light pion decaying to a muon or a heavier kaon decaying to muon, it can be seen that the energy of the decaying kaon is equally shared, on the average, between the products μ and ν_μ of the interaction. In contrast, the muon carries away most of the energy of the decaying pion, so that on average, higher energy (few hundred GeV) neutrinos mostly arise from Kaon decay. Determination of the kaon contribution and in particular the contribution of the associated production process thus becomes an important factor in determining the high energy atmospheric neutrino spectrum.

4.3 Propagation of the surface muons to the detector

When a charged particle passes through matter, it loses energy by ionization and radiative processes including bremsstrahlung, $e^+ e^-$ pair production and photonuclear interactions. At higher energies radiation loss becomes more important.

The energy loss, dE/dx , due to ionization for a relativistic muon can be described by the Bethe-Bloch formula,

$$-\frac{dE_\mu}{dx} \approx K \frac{Z}{A} \frac{1}{\beta^2} z^2 \left[\ln \frac{2mc^2 \beta^2 \gamma^2}{I} - \beta^2 \right], \quad (4.3.1)$$

where,

$K = 4\pi N_A r_e^2 m_e c^2$, N_A is the Avogadro's number ($6.022 \times 10^{23} \text{ mol}^{-1}$), r_e is the classical

electron radius (2.817 fm), m_e is the mass of electron (0.511 MeV/c²), c is the velocity of light, Z is the atomic number of the absorber, A is the atomic mass of the absorber, z is the atomic number of the incident particle and I is the mean excitation energy. The average rate of muon energy loss can be written as,

$$-\frac{dE_\mu}{dX} = a(E_\mu) + b(E_\mu)E_\mu, \quad (4.3.2)$$

where $a(E_\mu)$ is the ionization loss, and $b(E_\mu)$ is the fractional energy loss by the three radiation processes and X is the slant depth. These parameters are slowly varying functions of energy. Only muons with surface energies greater than 1 TeV will reach ICAL detector since the cavern will be 1.3 km underground. At these energies a and b can be considered as constants. The values for muon with ~ 1000 GeV surface energy are $a = 2.7 \times 10^{-3}$ GeV/(gm/cm²) and $b = 4.0 \times 10^{-6}$ /(gm/cm²).

The underground muon energy spectra can be determined from the muon energy at sea level and the energy loss as the particle passes through rock. The Eqn. 4.3.2 can be integrated to find the energy of the muon at a slant depth X as a function of surface muon energy, $E_{\mu,0}$,

$$E_\mu = \{E_{\mu,0} + \epsilon\}e^{-bX} - \epsilon, \quad (4.3.3)$$

where $\epsilon = a/b$. This is known as the muon critical energy, i.e., the energy at which ionization and radiation energy losses are equal. Below ϵ the ionization losses dominate and above ϵ radiation effects dominate.

4.4 Atmospheric muon Charge Ratio

The μ^+ and μ^- have been generated using the ‘‘pika’’ model described by P. A. Schreiner et al. [49]. The Gaisser’s equation is modified to study μ^+ and μ^- separately using the energy independent positive fraction parameters f_π and f_K . According to this model, the muon charge ratio can be expressed as,

$$r_\mu = \frac{\left\{ \frac{f_\pi}{1+1.1E_\mu \cos \theta_z / \epsilon_\pi} + \frac{\eta \times f_K}{1+1.1E_\mu \cos \theta_z / \epsilon_K} \right\}}{\left\{ \frac{1-f_\pi}{1+1.1E_\mu \cos \theta_z / \epsilon_\pi} + \frac{\eta \times (1-f_K)}{1+1.1E_\mu \cos \theta_z / \epsilon_K} \right\}}. \quad (4.4.1)$$

While the dependence on f_π and $(1 - f_\pi)$ for the π^+ and π^- terms arises from isospin symmetry, there is no such symmetry in the case of K^\pm ; however, a similar parametrisation can be used [51] with an error of just about 1%.

In this parametrisation, the muon ratio depends on $(E_\mu \cos \theta_z)$ rather than on the surface energy and zenith angle separately. At a fixed value of $E_\mu \cos \theta_z$, the intensity ratio of muons from π and K will be constant; this needs testing from data. Both π and K contribute to the charge ratio for all the energies from 1 GeV to 10 TeV.

A chi-square fit to the data of MINOS Near detector and Far detector gave a value of $f_\pi = 0.5538 \pm 0.0070$ and $f_K = 0.693 \pm 0.027$ [49].

This parametrization has been used to generate μ^+ and μ^- separately in this study.

4.5 Muon event generation

A code was written to generate the surface muon flux with energy $E_{\mu,0}$ and zenith angle θ according to Gaisser's formula. The generated muons were propagated to the underground detector using the energy loss formula and the detailed topography of the mountain. The muons reaching the detector were reconstructed using the ICAL GEANT4 code for their energy/momentum and direction (θ, ϕ) . These reconstructed values were used to propagate the muons "backwards" to the surface and thus obtain the reconstructed surface muon energy and direction.

4.5.1 Mountain Profile of INO site

The INO is proposed to be located at the Bodi West Hills near Pottipuram village in the Theni district of Tamil Nadu. The elevation profile of the 10 km area around INO peak at Bodi West Hills, Theni is generated from the topographical map provided by the Geological Survey of India (GSI) [53]. The latitude and longitude of the cavern location are: latitude $(77^\circ 15' 0'' E - 77^\circ 30' 0'' E)$ and longitude $(9^\circ 57' 30'' N - 10^\circ 0' 0'' N)$. The peak height is 1589 m above msl (the elevation has an error of ± 30 m) while the cavern will be located at 289 m above mean sea level (msl), giving a vertical overburden 1,300 m and at least 1,000 m in all upward directions. The latitude, longitude and elevation are converted to r, θ, ϕ for the calculation of slant depth with respect to the origin of the ICAL detector. The mountain 3D plot of 10 km distance around the INO peak is shown in Fig. 4.1. Note the very irregular azimuthal profile with heights to the West and the plains/plateau to the East.

4.5.2 The muon event generation

Since the minimum overburden is 1 km, the muons are generated with energies in the range 700–15,000 GeV; the polar angle θ is generated in the range $0^\circ - 70^\circ$ since the

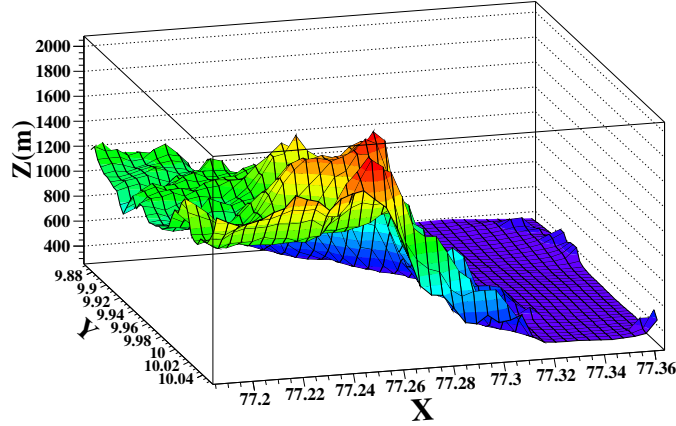


Fig. 4.1. Mountain 3D plot of 10 km distance around the INO peak. Here X and Y are the longitude and latitude in degrees while Z is the elevation in meters

flux formulae that were used are valid in this “flat Earth” approximation alone. In any case, the ICAL detector has very little sensitivity for angles $\cos \theta \lesssim 0.35$ or $\theta > 70^\circ$. The azimuthal angle, ϕ , is generated uniformly.

The cosmic ray muons generated pass through the material of the Earth and reach the detector at any of the five faces of the ICAL detector: top, left (west), right (east), front (south) and back (north). Since there are no cosmic ray muons from below, the bottom face does not contribute. For each face of ICAL, the range of ϕ is selected accordingly. The vertex of the events are generated uniformly (randomly) at all five faces of the ICAL.

The muons at the surface are passed through the mountain. The slant depth traversed by muons has been calculated from the digitized topographical map using the θ and ϕ information. The standard rock with density 2.65 g/cc is assumed. As the muons pass through matter they lose energy. Very low energy muons are stopped in the rock. It is found that only muons having surface energies greater than 1600 GeV reach the detector.

Only muons having energy less than 100 GeV at the detector are included in the analysis. Apart from reducing the computing time, in addition, the efficiency with which the charge of muons with energies higher than 100 GeV is measured falls below 98%; this will affect the determination of the charge ratio. Such events can be included by including additional systematics that take care of charge mis-identification, but this is not done in the present analysis. Hence the analysis is restricted to muons which reach the detector with at most 100 GeV energy, thus cutting out most of the very high

energy events at the surface. For instance, a cut of 100 GeV on the energy of muons detected at the detector corresponds to muons with surface energy about 2400 GeV in the vertical direction.

The distribution of the energy of the muons reaching the detector, the zenith and the azimuthal angle of the muons at the detector are shown in the figures Fig. 4.2a, Fig. 4.3a and Fig. 4.4a. The zenith angle distribution peaks around 28° . The ϕ distribution peaks around $\pi/2$ i.e., the east side of the mountain, due to the geography of the location.

4.6 Reconstruction of simulated events

The details of the ICAL detector can be found in Chapter 3. The design of the ICAL detector is ideal for studying muons. When muons with sufficient energy pass through the detector, they leave a long track. The cosmic ray muons and the muons from neutrino interaction can be distinguished from the event pattern. The vertex of the neutrino interaction will be inside the detector. Typically the charged current muon neutrino interaction gives a long muon track and an associated hadron shower near the vertex. The cosmic ray muons will only enter the detector from above through one of the five faces.

4.6.1 Reconstruction of muons inside ICAL using GEANT4

The underground atmospheric muon events generated using the Monte Carlo simulation are passed through the Geant4 based ICAL code in which the detailed geometry of the detector is described. The details of the code can be found in Ref. [36]. As described earlier the detector has three modules placed along x axis. The events are generated such that the three modules are placed in East-West direction. As the muon passes through the detector, it leaves hits in each layer. The muon events are reconstructed using the Kalman filter algorithm as described in Chapter 3. Earlier studies have shown that ICAL has good muon momentum reconstruction efficiency and charge identification efficiency even at high energies.

The vertices of the cosmic ray muon events are mostly in the so-called peripheral (including side) regions. Since the muons can have very high energies upto 100 GeV, their tracks are mostly not fully contained within the detector—these are the partially contained events. The response of the ICAL to muons in the peripheral region

has already been studied [41] and the events selection criteria have been optimized for fixed energy peripheral muons. The same criteria are used here to select the well-reconstructed events. First of all, a constraint on the number of hits, $N_{hits} > 20$, has been applied to the partially contained events. This removes events which are reconstructed with energies much smaller than the actual energies. For example, see Fig. 3.24 and its explanation in Chapter 3. In order to improve the quality of the selected events, the condition on reduced chi-square, $\chi^2/ndf < 10$, has also been used.

Only muons reconstructed with momentum greater than 0.5 GeV and less than 100 GeV are considered for analysis; with this constraint, only 73% of the total events remained. When including the condition on N_{hits} , the fraction of reconstructed events is reduced to 60.5%. After applying the selection criteria, 60% of μ^+ and 61% of μ^- have been selected.

The distribution of reconstructed energy at the detector, zenith angle and the azimuthal angle are shown in figures Fig.4.2b, Fig.4.3b and Fig.4.4b respectively. It is seen that ICAL has excellent angular resolution so that the *shape* of the flux distribution as a function of angle (both θ and ϕ) is well-preserved even after reconstruction.

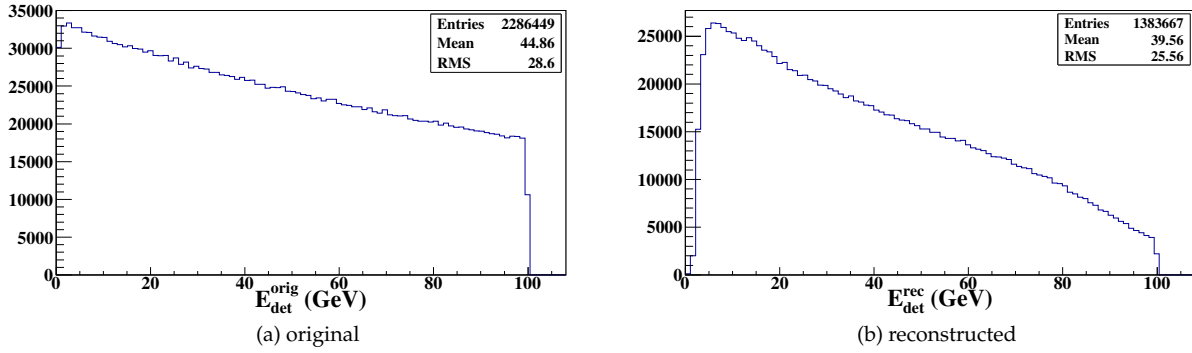


Fig. 4.2. The distribution of energy of muons at the detector for one year

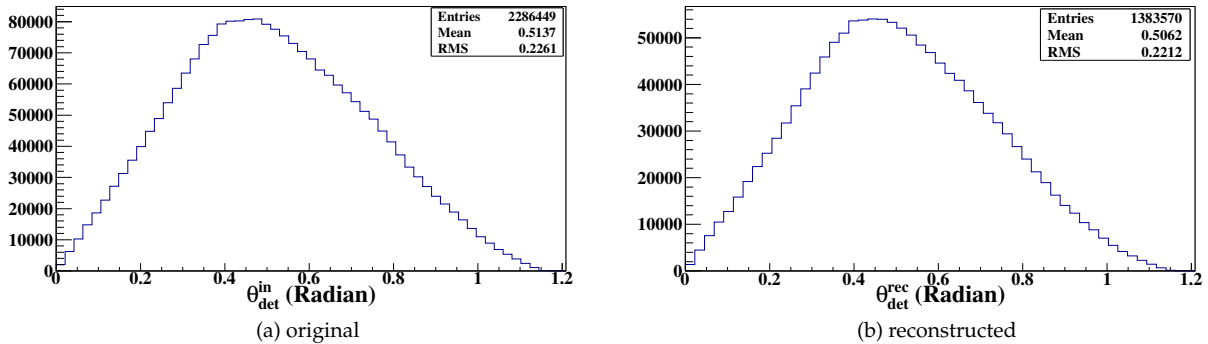


Fig. 4.3. The zenith angle distribution of muons at the detector for one year

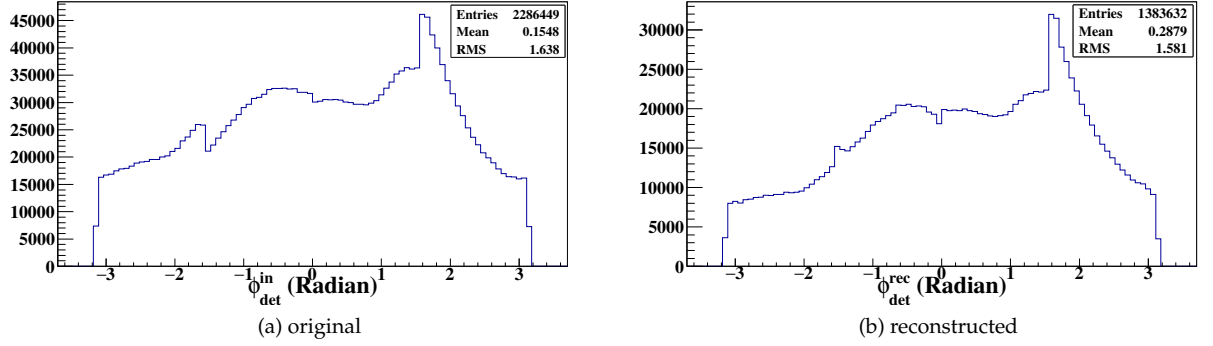


Fig. 4.4. The ϕ distribution of muons at the detector for one year

4.6.2 Reconstruction of surface energy of events

The surface energy of the muons can be calculated from the reconstructed detector energies and angles. The slant depth is first calculated using the zenith and azimuthal angle information using the local topography to locate the “surface point” from where the detected muon should have originated. Then the surface energy is calculated using the equation,

$$E_{sur}^{rec} = \{E_{\mu, det}^{rec} + \epsilon\} e^{bX} - \epsilon. \quad (4.6.1)$$

The distribution of the original and reconstructed surface energy is shown in Figs. 4.5a and 4.5b. The notation E_{μ}^0 has been replaced by E_{sur}^{orig} to distinguish the surface muon energy from the detector muon energy.

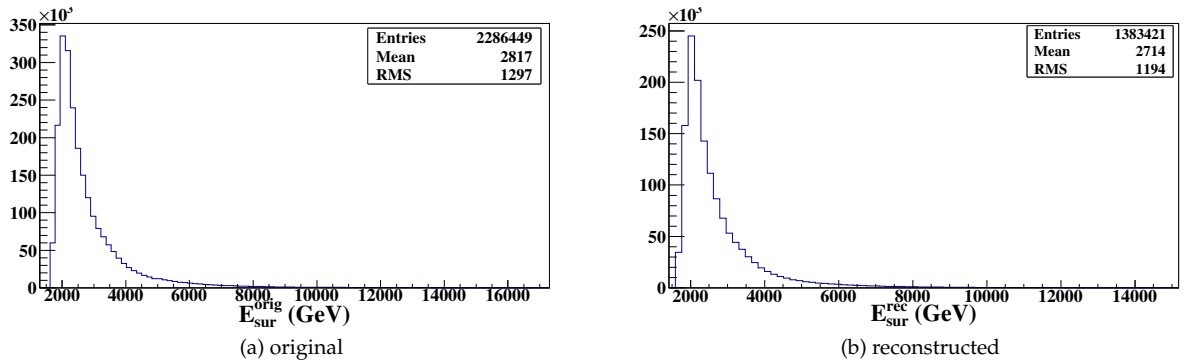


Fig. 4.5. The distribution of surface energy of muons reaching the detector for one year

4.7 Results and Discussion

The reconstructed events are separated into μ^- and μ^+ events according to the sign of the reconstructed charge. Since the charge identification efficiency of the sample as a whole is about 96–97%, no attempt was made to account for charge misidentified

events and correct for them. The muon charge ratio (R_μ) was then studied as a function of surface energy (E_{sur}), zenith angle (θ), azimuthal angle (ϕ) and the product of surface energy and $\cos \theta$. It was found that the results improved by redefining the charge ratio with an efficiency correction, i.e., if ϵ^+ and ϵ^- are the reconstruction efficiencies of μ^+ and μ^- respectively, the charge ratio $R_\mu = N_{\mu^+}/N_{\mu^-}$, is redefined as

$$R_\mu = \frac{N_{\mu^+}/\epsilon^+}{N_{\mu^-}/\epsilon^-}, \quad (4.7.1)$$

where N_{μ^+} (N_{μ^-}) is the number of μ^+ (μ^-) reconstructed with a years' exposure at ICAL. Here ϵ is a function of E_{det} , θ_{det} and ϕ_{det} . Because of the detector resolution the ϵ 's can be more than one in some bins; this occurs especially because of the steeply falling flux as a function of energy so that the larger flux at lower energy can smear out into the higher energy bins due to finite detector resolution. The Kalman filter is also more likely to overestimate momenta of high energy muons because it depends on determining the track curvature which is very small at larger energies.

The pure charge ratio (not weighted with efficiency) as a function of surface muon energy for different θ bins is given in Fig. 4.6 as calculated from the top surface events alone. It is seen that the original and reconstructed R_μ match very well even without the efficiency correction. The number of muons reaching the top surface is almost double compared to the total events at the other surfaces because of the acceptance effect. Since most of the top surface events go through large number of layers in the detector the reconstruction of events is very good compared to other surfaces. The zenith angle is divided into six bins: 0–0.2, 0.2–0.4, ..., 1–1.2. It can be seen that the low energy events are coming from nearly vertical angles. As θ increases, the events having large surface energy also increase. At higher energies the number of events is small since the flux falls as energy increases and the 100 GeV cut on detector energy also plays a role. So the error bars are large. All the events from 10 TeV to 15 TeV are added together to give the events in the last energy bin. The R_μ is seen to slightly increase as E_{sur} increases.

Fig. 4.7 shows the muon charge ratio determined from all the events in one year exposure at ICAL. Since different parts of the ICAL detector have very different angular dependence of resolutions, simply adding events with the same energies but detected from different angles lead to large fluctuations. Hence the efficiency-weighted charge ratio is plotted in this case. The errors are smaller than in the case with top-surface

events only.

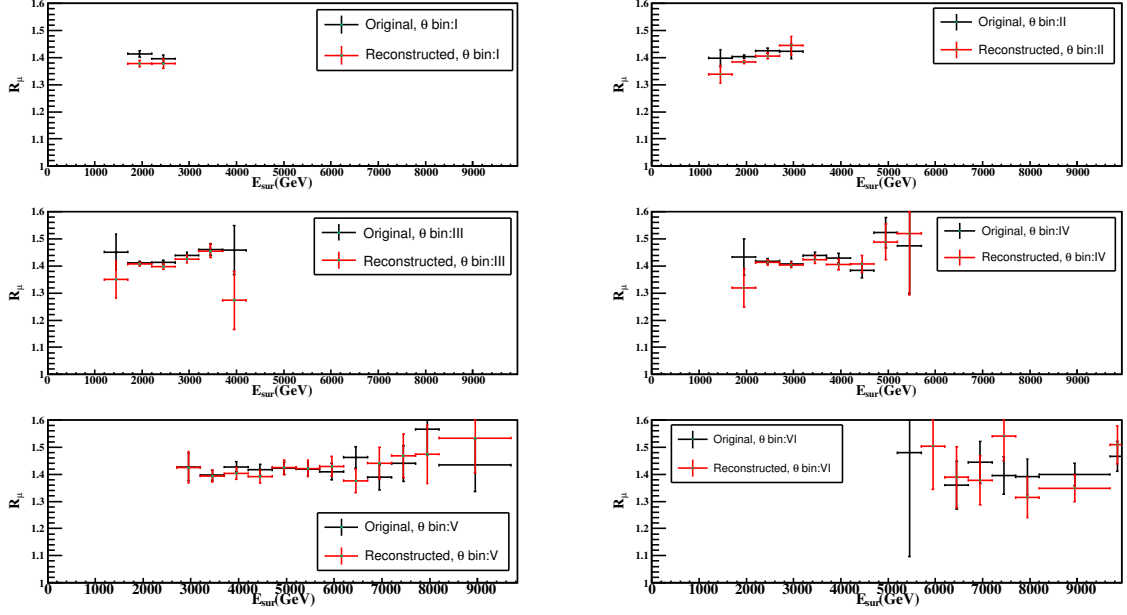


Fig. 4.6. Charge ratio $R_\mu = N_{\mu^+}/N_{\mu^-}$ as a function of surface energy of the muons detected at the top surface of ICAL alone.

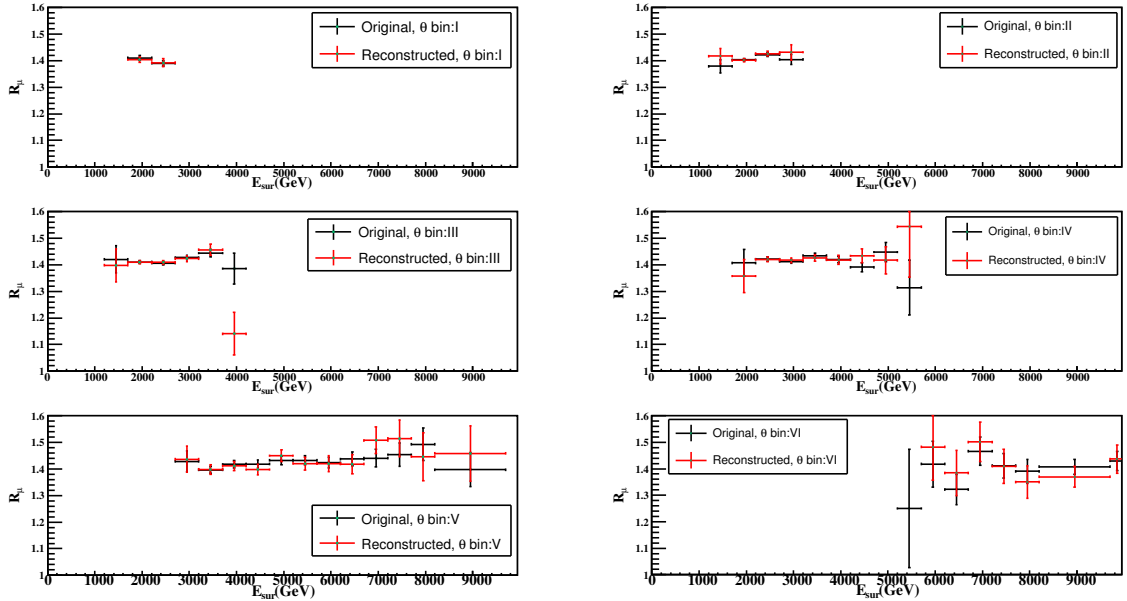


Fig. 4.7. Efficiency weighted charge ratio as a function of surface energy of the muons detected over the entire detector.

4.7.1 Angular dependence of the charge ratio

The charge ratio as a function of azimuthal angle is shown in Fig. 4.8. It can be seen that the R_μ is almost constant around 1.41 for all the ϕ bins and within statistical fluctuations the original and reconstructed R_μ are same for both top surface (without effi-

ciency correction, Fig. 4.8a) and the whole ICAL detector (Fig. 4.8b). The ϕ dependence of the detector is nontrivial because of the mountain profile and the magnetic field.

The charge ratio as a function of the zenith angle is given in Fig. 4.9 for the whole detector. The R_μ is almost constant for all the angles around 1.4. The ICAL detector has a very good angular resolution which is better than a degree for most of the energies and angles. In addition, the INO cavern is proposed to be located in a region which has a non-trivial topography with respect to azimuthal angle dependence. For the *same* zenith angle, for example, in bin V with $\theta = 0.8\text{--}1.0$ radians ($46^\circ\text{--}57^\circ$), the variation in azimuthal angle ϕ samples very different slant depths so that it is sensitive to surface muon energies ranging from 3–9 TeV. In fact, because of the azimuthal variation, different zenith angles are sensitive to different ranges of surface muon energies, in contrast to MINOS which has a flat topography (since it is located in a mine) with a high correlation between zenith angle and surface muon energy. Since the flux is a rapidly falling function of the energy, this means that every direction/bin in (θ, ϕ) is dominated by events with a different (lowest) energy, thus allowing the measured charge ratio to be sensitively measured as a function of both energy and angle. This means that assumptions such as energy and angle dependence of various parameters in Eq. 4.2.1 can be tested at ICAL.

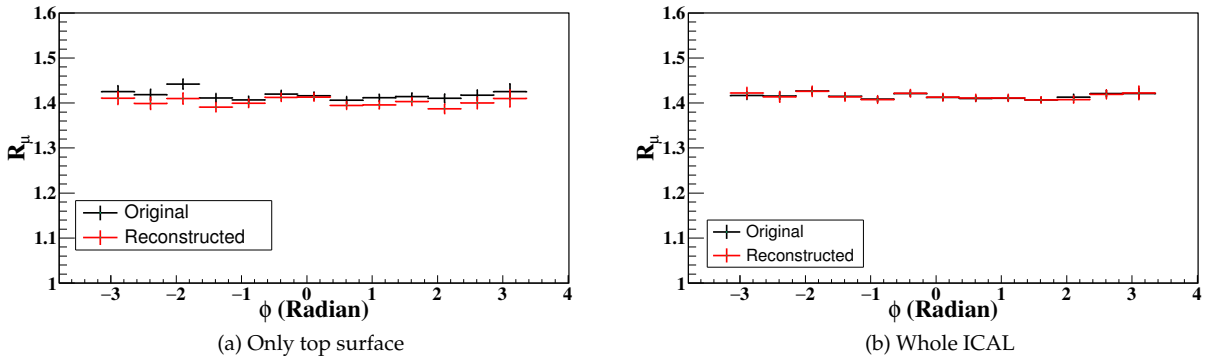


Fig. 4.8. Charge ratio as would be measured by ICAL over 1 year as a function of azimuthal angle.

Figures Fig. 4.10 and 4.11 show the charge ratio as a function of the product $(E_\mu^{surface} \cos \theta)$. According to the “ πK ” model, the charge ratio depends not separately on the surface energy and zenith angle but on the product $(E_\mu^{surface} \cos \theta)$. Fig. 4.10a shows the result for the top surface without efficiency correction. The lowest value of $E_\mu^{surface} \cos \theta$ that ICAL can probe with the existing configuration is ≈ 1500 GeV. Fig. 4.10b shows the comparison of results with the efficiency-corrected value of R_μ calculated using

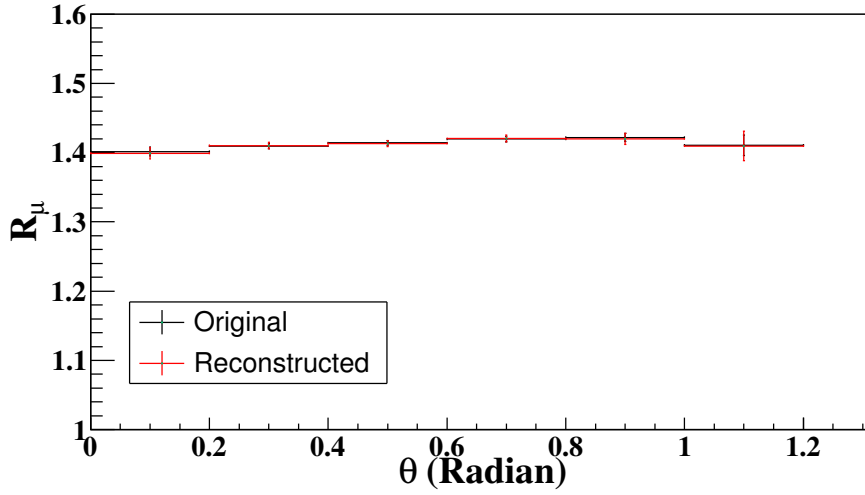


Fig. 4.9. Charge ratio as would have been measured by ICAL over 1 year as a function of zenith angle.

Eqn. 4.4.1. The reconstructed charge ratio matches very well with the theoretical value. As $E_{\mu}^{surface} \cos \theta$ increases, R_{μ} slightly increases.

In Fig. 4.11 the results with 1 year of simulation at ICAL are compared with the results of existing experiments. It is seen that ICAL has good sensitivity (due to the depth of the INO cavern) to cosmic muons with surface energies in the region beyond $E_{\mu}^{surface} \cos \theta \gtrsim 3$ TeV where there is very little data available. In addition, it will have significantly better quality data even down to 1.5 TeV. Finally, it has sensitivity to *uncorrelated* values of $E_{\mu}^{surface}$ and $\cos \theta$ which the MINOS data does not. Hence it will be able to determine with good precision the various parameters that the cosmic ray muon flux depends on, such as the K/π fraction, η , and in turn the contribution of the associated production process to K production in cosmic ray interactions.

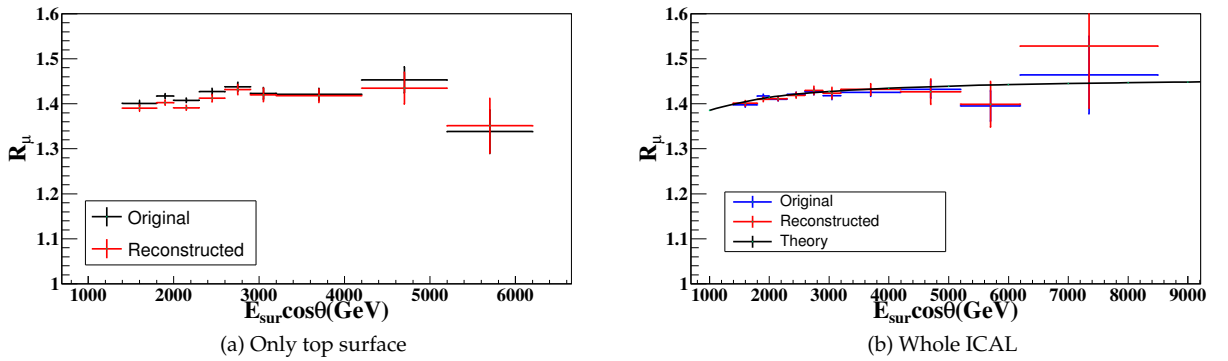


Fig. 4.10. Charge ratio as a function of $E_{\mu}^{surface} \cos \theta$ from simulated data with 1 year exposure at ICAL.

Finally, it must be noted that the energy loss mechanism of muons through the Earth has been modeled here to be charge-independent. In case this is not so, a cor-

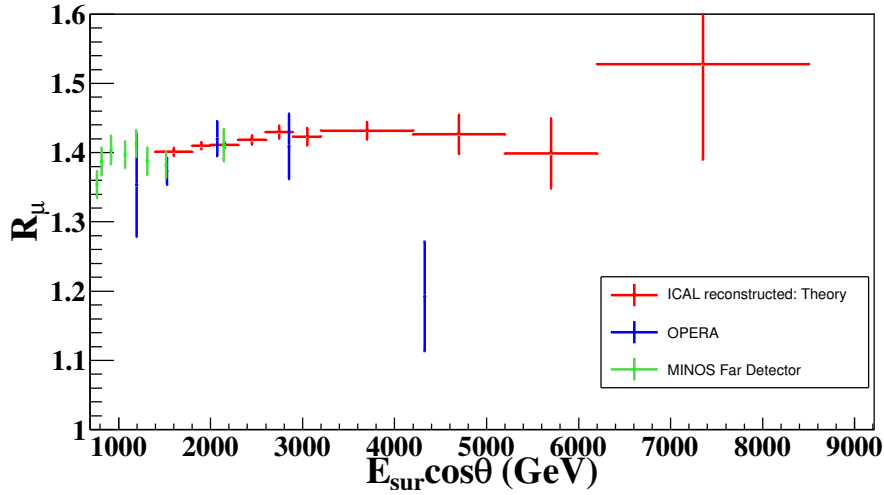


Fig. 4.11. Charge ratio expected to be measured over 1 year at ICAL as a function of $(E_\mu^{\text{surface}} \cos \theta)$ in comparison with other experiments.

rection has to be applied. An analysis of the resulting data is beyond the scope of this work.

4.8 Summary

The ICAL detector at INO, optimized to study muons from neutrino interactions, can also be used to study the cosmic ray muons. Being a magnetized detector, the ICAL can distinguish between μ^+ and μ^- . It is found through simulation studies that the ICAL has a good charge identification efficiency. The ICAL detector has a rock overburden of minimum 1 km from all directions which helps to study the muon charge ratio at higher energies.

Here the sensitivity of the ICAL detector to observe the atmospheric muon charge ratio was studied. The muon energy and angular spectra at sea level were generated using standard Gaisser's formula. These muons were propagated through rock. The topographical map of the Bodi West Hills was used to calculate the slant depth. The muons lose energy while passing through Earth. It was observed that only muons having minimum surface energy of about 1600 GeV reach the detector. The μ^+ and μ^- have been generated using the "pika" model described.

Events were generated for five sides of ICAL detector: top, left, right, front, and back. These events were passed through the GEANT4 based ICAL code and reconstructed using Kalman filter. The surface energy of the muons was calculated from the reconstructed detector energy and angle. The muon charge ratio, calculated with effi-

ciency correction, was studied as a function of surface energy (E_{sur}), zenith angle (θ), azimuthal angle (ϕ) and the product of surface energy and $\cos \theta$. The results of the top surface and the whole detector were studied separately. The charge ratio for the top surface was calculated without efficiency correction. It was observed that the reconstructed and the original charge ratio match well within statistical fluctuations. The charge ratio was nearly constant around 1.4 for all the θ and ϕ bins since ICAL is not sensitive to lower surface muon energies due to its depth. The reconstructed charge ratio as a function of $E_{\mu}^{surface} \cos \theta$ was compared with the theoretical value and it was observed that within the fluctuations they are identical.

The ICAL detector is sensitive to the atmospheric muon charge ratio for the surface muon energies above ~ 1600 GeV and for the $E_{\mu}^{surface} \cos \theta$ values above ~ 1500 GeV. Here the analysis was done using data for one year. With more data the fluctuations at higher energies can be reduced. The correction on the charge misidentification is not included in this analysis since the charge identification efficiency is above 96–97%.

When primary cosmic rays interact with the atmospheric nuclei, secondary particles like pions and kaons are produced. These unstable particles decay to produce particle like muons, neutrinos, etc. While π^+ , K^+ give μ^+ , the π^- , K^- give rise to μ^- in their decays.

The weakly interacting neutrinos travel through the atmosphere and Earth without much interaction. The low energy muons decay before reaching the sea level and produce electrons and neutrinos. The average energy of muons at sea level is ~ 4 GeV. Studies have shown that the ratio of number of μ^+ to μ^- is more than one. This is mainly due to the excess of protons in the primary cosmic rays. In addition, it is observed that this ratio increases as the muon energy increases. This has been attributed to the opening up of the K production and decay channel due to higher energy cosmic primaries, in particular, the associated production process $pA \rightarrow K^+ \Lambda X$, where A is an average air nucleus, and X can be anything. The corresponding interaction initiated by neutrons produces K^0 and not K^- , thus leading to an eventual excess of μ^+ over μ^- in the observed secondary cosmic ray flux. While the muon charge ratio appears to depend on the product ($E_{\mu}^{surface} \cos \theta$) rather than $E_{\mu}^{surface}$ alone, this has so far been tested with a detector (MINOS) that has correlated values of $E_{\mu}^{surface}$ and $\cos \theta$. Hence this can be tested at ICAL.

In addition, the very non-trivial azimuthal angle dependence of the muon flux at

ICAL due to the topography of the proposed INO cavern implies that various parameters that determine the cosmic ray muon flux, including its zenith angle dependence and the contribution from K mesons, can be precisely determined at ICAL. This in turn will help to improve the understanding of atmospheric neutrinos at higher energies (beyond a few hundred GeV) which dominantly arise from the decays of such K mesons.

Finally we note that there is a possibility that μ^+ and μ^- have different energy loss mechanisms when propagating through the Earth on their way to the detector [49]. This will affect the determination of the muon charge ratio; such a study is beyond the present scope of this thesis.

Part II

Detector studies

Fabrication and Testing of Bakelite Resistive Plate Chambers

5.1 Introduction

Particle or radiation detectors are devices used to detect, track or identify the particle/radiation produced in the interaction. They can be used as calorimeters to measure the energy or momentum of the particle. They may also be used to measure the charge, spin etc. of the particle. The particles are detected through their interaction with the detector. According to the type and energy of the particle, different detection methods are used like gaseous detectors, scintillation detectors, semiconductor detectors etc.

The working principle of gaseous detectors is the ionization of the gas medium as a particle passes through it; the primary ionization is amplified by a strong electric field. The ionization is localized with a suitable gas composition. The signal collected may be used to get the position information of the incident particle. The history of gaseous detectors started with proportional counters. There are different kinds of gaseous detectors depending on the nature of gas filled and the strength of the electric field. Gas filled detectors are widely used in high energy physics experiments (eg. CMS, ATLAS, ALICE, STAR, Belle). Since they are cheap and easy to make compared to the other detectors like scintillation detectors, they are used in large scale experiments. Good time and position resolution make them a good choice for tracking detectors.

The modern gaseous detectors include Multi-Wire Proportional Counter (MWPC), Resistive Plate Chambers (RPC), Gas Electron Multiplier (GEM), micromegas etc. The micropattern detectors provide very good position resolution. Due to the small distance between the electrodes they have good time-resolution and counting rate capability.

The Resistive Plate Chambers (RPC) are gaseous detectors first introduced by R. Santonico and R. Cardarelli [54]. They were developed by using the principle of spark counters by Pestove et al. [55]. These are made of high resistivity plates ($10^9 - 10^{12}\Omega$), such as bakelite or glass. The electrodes are coated with conductive graphite to provide constant electric field. The gap between the electrodes is filled with the gas mixture which contains ionization gas and quenching gas.

The recent developments in the detector technology of RPCs resulted in improving the time resolution and the rate capacity of RPCs. Other than the single gap RPCs, double gap RPCs and then the multigap RPCs were also introduced [56]. Many experiments use RPC as tracking or triggering detectors. The large experiments using RPC include L3 at CERN, BABAR at SLAC, BELLE at KEK, OPERA at LNGS etc. The main experiments in CERN, ATLAS and CMS use RPCs for muon trigger system [57, 58]. Their advantages are simplified and robust structure for coverage of a large area, ease of operation, and at the same time, they can deliver very good time resolution (reported up to ~ 80 ps [59]) with one of its variants. The single gap RPCs are mostly used as trigger and tracking detectors for the small transverse momentum (p_T) region of these experiments. Long term stable operation and capability to handle high fluence rates are the major characteristics demonstrated by the RPCs, which make them preferred detectors in many such experiments.

RPCs have been chosen as the active detector elements in the massive iron calorimeter (ICAL) experiment at the upcoming India-based Neutrino Observatory (INO) [26]. Prototype RPC detectors of different sizes and configurations have been fabricated and characterized for its suitability in the ICAL experiment environment during the past few years [67–71]. Constructional details of the bakelite RPCs and the characterization of electrical properties of the materials [68–70], characterization of surface roughness and its effect on the operation of bakelite RPCs, and effect of inner surface coating of various types were already reported [69]. Long term stability of operation in streamer mode was successfully demonstrated using a cosmic muon telescope test bench [68]. The same detector, operated in avalanche mode, was also exposed to the gamma irradiation facility (GIF; ^{137}Cs source, 570 GBq) at CERN for 23 days at a stretch [72]. No

significant degradation of performance was noticed in this study even after exposure resulting in equivalent charge accumulation of 30 C.m^{-2} . This may be considered as equivalent to approximately 2 years of exposure to average atmospheric muon flux at the mean sea level.

5.2 Working Principle of Resistive Plate Chambers

When a charged particle passes through the gap, the gas is ionized which produces primary electrons and ions. The electrons, under the influence of the applied electric field, acquire sufficient drift velocity and move towards the anode causing secondary ionization in the gas. Recombination processes, which occur during the avalanche development produce photons. These photons can cause further ionization which produces large amount of free charges in the gas. This is the streamer regime. If the avalanche is so large that it can connect two electrodes, it is called a spark. The electric field in the gas gap drops locally around the discharge due to depletion of localized charges from the anode surface near the avalanche. The detector is dead until the electrodes are recharged. The high resistivity of the electrodes prevents the discharge from spreading over the entire area.

The Argon in the gas mixture acts as an ionizing gas. The isobutane is used to quench further ionization by the photons and limit the production of secondaries. The electronegative gas Freon (R134A) limits the abundance of free charges in the gas and prevents the streamer from spreading in the transverse direction.

5.2.1 Modes of operation

The RPCs can be operated in avalanche mode or streamer mode. The two modes significantly differ in characteristics as stated below. In the avalanche mode, quenching of secondary ionization by photons and electrons are done to limit the size of avalanche and prevent formation of streamer. On the other hand, in streamer mode, photon quenching is done but controlled streamer formation is allowed. Generally, the effective charge generated per event in the streamer mode is much larger than that in the avalanche mode. By changing the gas composition and the applied electric field to bias the detector, the RPCs can be operated in either of the two modes.

5.2.1.1 Avalanche Mode

The charged particle passing through the gaseous medium produces primary ions. These primary ions get accelerated by the strong electric field and produce secondary ionisation by colliding with the gas molecules. The external electric field opposes the electric field due to the ionising particles and the ionisation stops after some time. The charge which drifts towards the electrodes gets collected there.

The amplitude of the signal produced by this mode is a few mV and hence the signal has to be amplified before passing to the read-out system.

5.2.1.2 Streamer Mode

In streamer mode, the secondary ionisation continues until there is a break down of gas and a continuous discharge takes place. This mode results in high gain and the pulse amplitude is of the order of 100 mV. So the signal from RPC need not be amplified which simplifies the read-out electronics.

If n_0 is the number of primary electrons, the number of electrons reaching the electrode is,

$$n = n_0 e^{(\alpha - \beta)x}, \quad (5.2.1)$$

where α is the Townsend coefficient and β is the attachment coefficient and x is the distance between the points where the electrons are produced and the anode. If the gain of the RPC, n/n_0 , is larger than 10^8 , then it is streamer mode and if n/n_0 is much smaller than 10^8 , then it is avalanche mode.

5.3 Fabrication of RPCs

A schematic representation of a single gap RPC is shown in Fig. 5.1. Two RPCs of dimension 22.5 cm \times 30 cm are fabricated for the experiment. The P-120 grade bakelite, manufactured by Bakelite Hylam, India, is used for the high resistive electrode. It has good electrical properties under humid conditions. The thickness of the bakelite plate is 2 mm. It has a density of 1.22 g/cc and bulk resistivity $3.67 \times 10^{12} \Omega\text{cm}$. earlier[68].

After cleaning with alcohol the inner surfaces of the electrodes have been coated with thin silicone in order to make the surface smoother. The effect of the silicone coat-

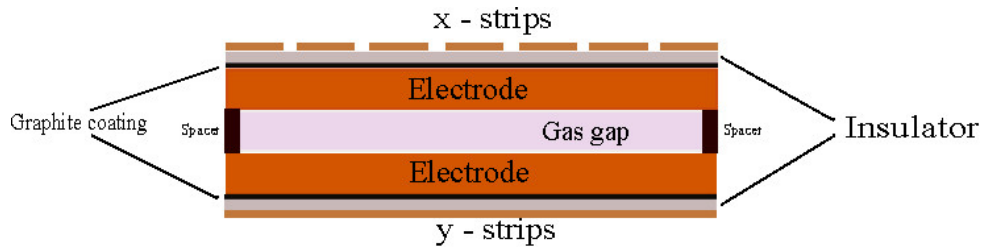


Fig. 5.1. Schematic representation of a RPC

ing on the performance of RPC has been reported earlier [68, 69]. The surface resistivity of the bakelite surface coated with silicone is two times less compared to the uncoated surface. It is also necessary for the stable performance of the RPC.

One button spacer of thickness 2 mm and diameter 1 cm is used to provide equal separation between two electrodes. Two gas nozzles are glued diagonally as a part of edge spacers. All these are made of polycarbonate; see Fig. 5.2. After proper cleaning using alcohol, graphite is coated on the two sides of the bakelite. A gap of 2.5 cm is maintained from all edges to the graphite layer in order to avoid external discharge. Surface resistivity is measured and found to be 1-2 M Ω /square. Two small copper foils are pasted by kapton tapes on both the outer surfaces for application of high voltages. The high voltage connectors are soldered on these copper strips. Equal high voltages with opposite polarities are applied on both the surfaces in small steps. A completed RPC is shown in Fig. 5.3. The surface resistivity measurement set-up is shown in Fig. 5.3. The gas used for the streamer mode is a mixture of Ar (55%), isobutane (7.5%) and

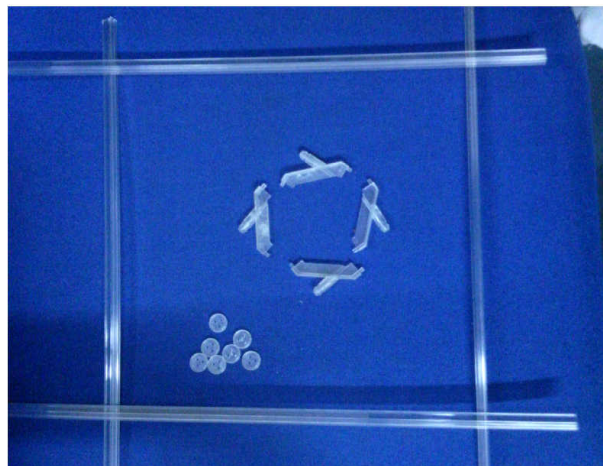


Fig. 5.2. Gas nozzles, edge spacers and button spacers

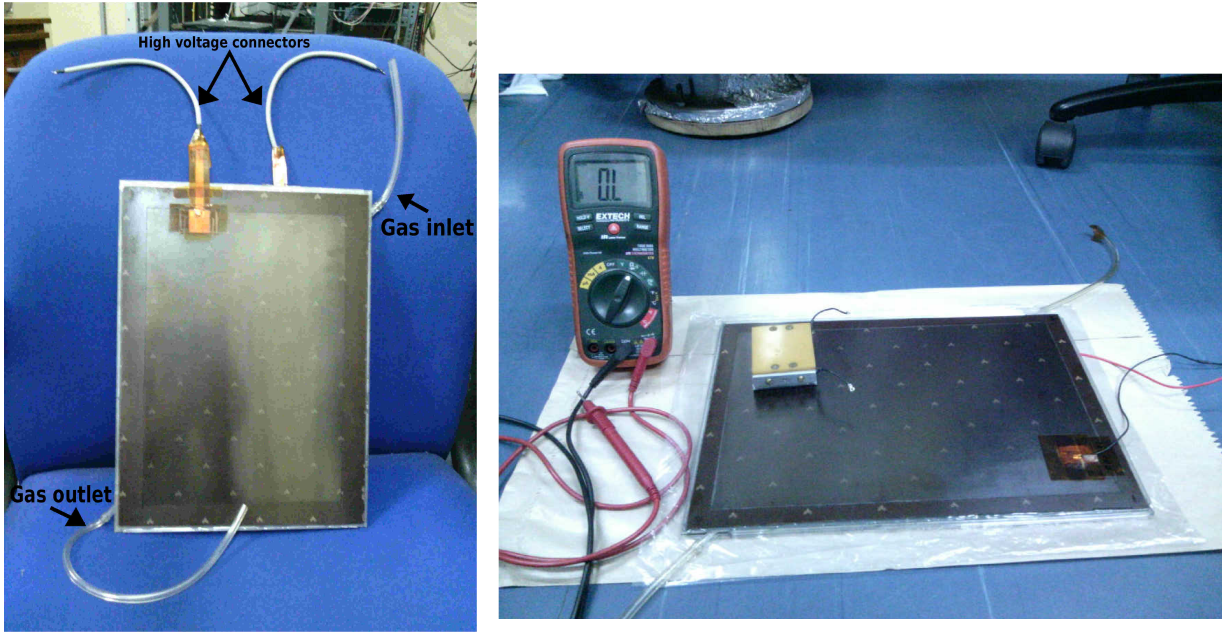


Fig. 5.3. Left: Completed RPC. Right: Surface resistivity measurement set-up.

tetrafluoroethane (37.5%) and that for the avalanche mode operation was a mixture of tetrafluoroethane (95%) and isobutane (5%). The gases are premixed and stored in a stainless steel container (Fig. 5.4).

In order to collect the induced signals, pick-up strips are placed above the graphite coated surfaces on either side of the RPC.

5.4 Fabrication of Pick-up panel

The pick-up strips are made of 16 conductor ribbon cables of width 2 cm and thickness 1 mm which are glued on a Mylar sheet of thickness 0.1 mm. Out of 16 conductors of the cable, 15 consecutive conductors are shorted together to form the pick-up strip, while the remaining one is grounded. There are 10 pick-up strips on the top pick-up panel and the bottom one has 14 pick-up strips. Adhesive double-sided foam tapes of 2 mm thickness are used to fix a grounded aluminium plate on top of each of the pick-up panels (Fig. 5.5). The signal from the strips are taken to the front-end electronics using coaxial cables. The impedance analysis of the pick up panel is done using Instek LCR meter. The inductance of the ribbon cable is $L \sim 11600$ pH/cm. The capacitance of each strip (C) is measured using LCR meter. Then the impedance is measured using



Fig. 5.4. Gas mixing unit.



Fig. 5.5. Ribbon cable pick up panel

the formula:

$$Z = \sqrt{L/C}. \quad (5.4.1)$$

The measurement is repeated for three times and the average impedance and standard deviation are calculated. The impedance along with the standard deviation is plotted in Fig. 5.6 . Almost 10% variation in impedance can be seen across the strips.

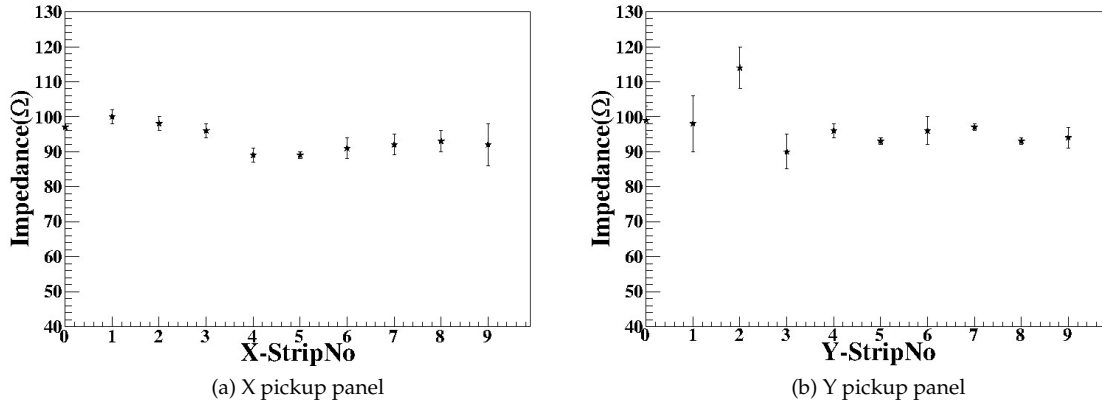


Fig. 5.6. Impedance of different Strips

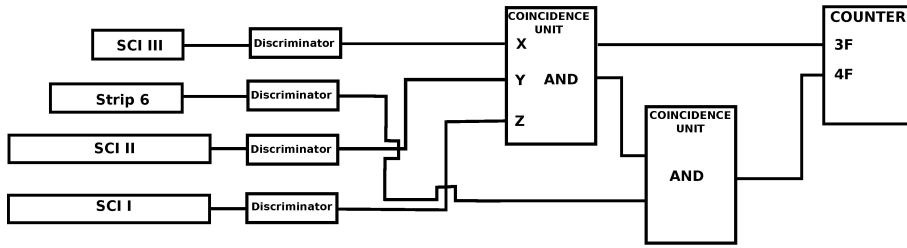


Fig. 5.7. Schematic view of efficiency measurement set up

5.5 Cosmic ray test set up

The Fig. 5.7 shows the schematic of the experimental set-up in a cosmic muon telescope test bench which was used in earlier measurements as well [68]. Two scintillators (SC I and SC II) were placed below the RPC and one (SC III) was placed above. The coincidence between SC I (93.5 cm \times 19.5 cm), SC II (82.5 cm \times 19.5 cm) and SC III (17 cm \times 4 cm) gives the 3-fold trigger as the cosmic muons pass through them which is treated as the Master Trigger. Based on a Monte Carlo simulation of the above set-up, it is found that two adjacent pick-up strips of RPC are in coincidence with the 3-scintillator muon telescope. Therefore, the signals from the two adjacent pick-up strips were OR-ed and the coincidence between this signal and the 3-fold was taken as the 4-fold coincidence trigger. The cosmic ray test was done in the streamer mode.

The high voltage was applied to the RPC on both the electrodes at a ramp-up rate of 5 V/s. The pulses in the streamer mode start appearing when the high voltage reached \sim 5 kV. The signal from the RPC and the scintillators were sent to the leading edge discriminators. Different thresholds were tried and the RPC threshold for the

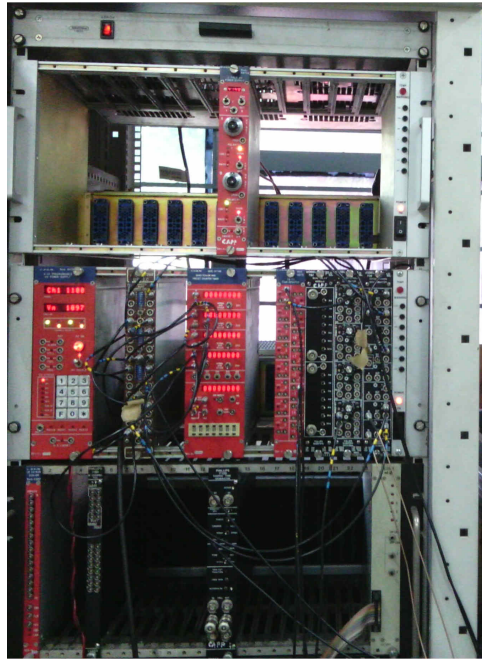


Fig. 5.8. The front-end electronics and DAQ

experiment was fixed to 10 mV. A CAMAC-based data acquisition system LAMPS, developed by the Electronics Division, Bhabha Atomic Research Centre [73] is used for collecting data (Fig. 5.8).

Storage oscilloscope trace of a typical induced pulse on a pick-up strip at 8 kV detector bias voltage is shown in Fig. 5.9.

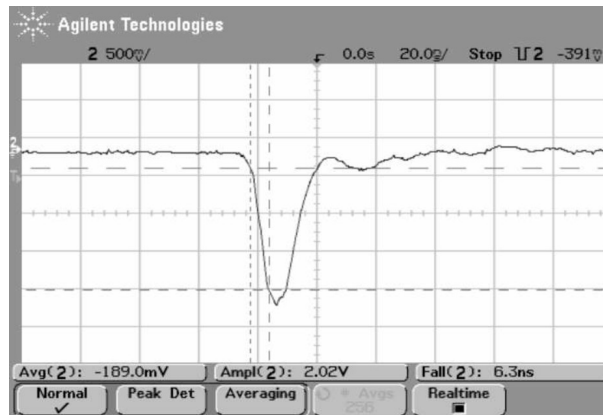


Fig. 5.9. Typical induced pulse on a pick up strip at 8 kV

5.6 Results

The performance of the RPC was tested using the cosmic ray muon test setup. The leakage current across the the electrodes, noise rate and efficiency were measured. The

data were collected for 15 minutes at each point as voltage is increased.

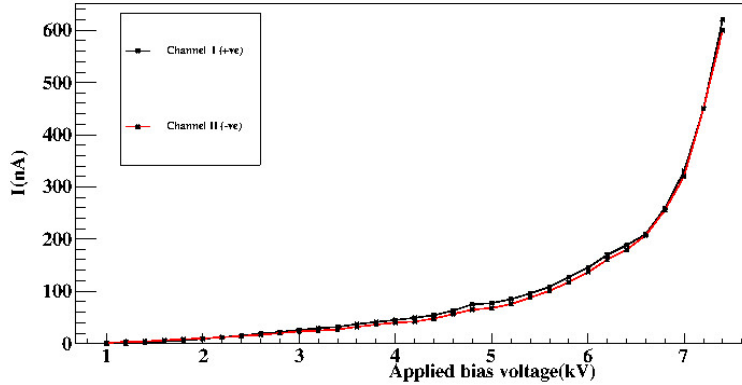


Fig. 5.10. Leakage current as a function of voltage

The leakage current through the RPC was measured as a function of the applied voltage (Fig. 5.11). The current vs. applied bias voltage plot shows a two-slope behaviour with 'knee' region around 6 – 7 kV, where the slope changes. At low voltage the gas gap has infinite resistance since the avalanche does not develop. The current flows through the spacers. But after the knee voltage, the gas starts conducting. It can be seen from the figure that for both positive and negative electrodes, the knee voltage is around 6.5 kV.

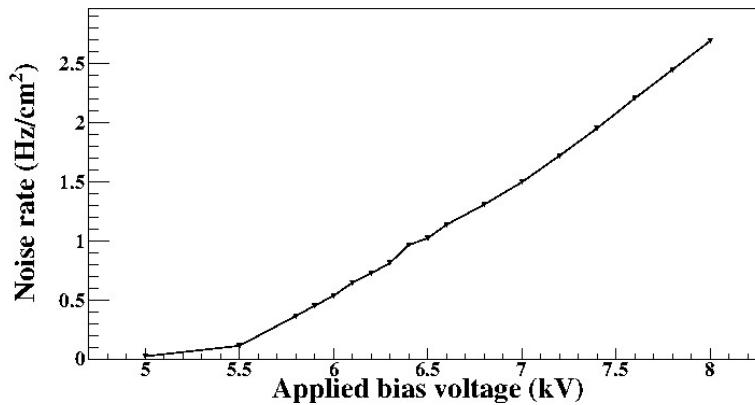


Fig. 5.11. Noise rate as a function of voltage

The noise rate of RPC is the total counting rate of all the signals above the discriminator thresholds. This include the signals from cosmic rays and other background signals. The noise rate increases as voltage increases since even the signals due to low energy particles get amplified. The increase in noise rate can reduce the field across the

electrodes which results in the reducing the efficiency. The Fig. 5.11 shows the noise rate as a function of applied voltage.

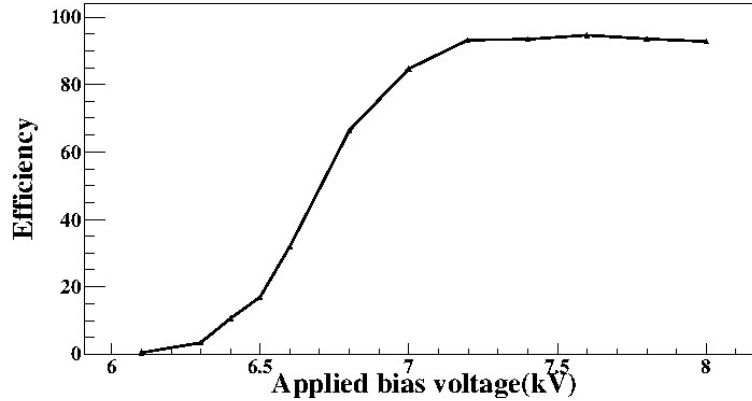


Fig. 5.12. Efficiency(%) as a function of voltage

The efficiency of a detector determines its ability to see the particles passing through it. In low rate experiments, the efficiency has a crucial role. Here the efficiency is defined as the ratio of 4-fold signals to 3-fold signals. The efficiency is plotted as a function of applied voltage (Fig. 5.12). Beyond the break down voltage the efficiency starts increasing from about 20% and in the plateau region to about 90%. This high efficiency of RPC helps in detecting the charge particles more accurately.

5.7 Summary

The bakelite based RPCs of dimension $22.5 \text{ cm} \times 30 \text{ cm}$ were fabricated using locally available bakelite. The inner side of the RPC was coated with silicone fluid for stable performance of RPC. A ribbon cable pickup panel was fabricated for collecting the signals from RPC. The characteristic impedance of the strips were found to be about 100Ω . The RPC was operated in streamer mode. The pulse from the streamer mode shows good rise time and amplitude.

The RPC was tested using a cosmic ray test set-up. The RPC threshold was set to be 10 mV. The signals were counted for 15 minutes for measuring noise rate and efficiency. The I-V characteristics of the RPC was also studied. In the plateau region the efficiency is found to be nearly 90%.

The operating voltage and the threshold have been optimized for the further studies of RPC. The detailed study of these properties and timing characteristics will be presented in the following chapter.

Effects of variation of environmental parameters on the performance of Resistive Plate Chamber detectors

6.1 Introduction

Recent studies have shown that external environmental conditions can influence the performance of RPC detectors. It is important to understand the variation of the detector parameters in different external environmental parameters. Especially in the experiments with low event rate, influence of external environmental parameters on stable RPC operation, with a view to specify a safe window for such operation and understanding the physical reasons behind such dependence, are important research goals being pursued by several groups [61–66]. Understanding the behaviour of RPCs under different environmental conditions is more important when the detector is placed underground where such environmental conditions are more critical than in a normal laboratory.

Relative humidity and temperature dependence on the performance of RPCs have been studied earlier by different groups [61–66]. Decrease of bulk resistivity of the electrodes with relative humidity and increase in the threshold of reaching the efficiency plateau has been observed by Icroty et al. [61]. A. Moshaii et al. [62] have studied the effect of water vapour on the performance of RPC in the avalanche mode of operation by Monte Carlo simulation. They have shown that the humidity in the gas has no effect on avalanche multiplication at room temperature. But at higher temperature ($\sim 40^\circ\text{C}$), the charge content increased with increase of humidity. In another work [63], the effect of temperature on the performance of RPC was studied using Monte Carlo simulation. It was observed that the charge content increased with increase of temperature. Decrease of plate resistance with increase in temperature was observed, which resulted in the improvement of efficiency. Long term stability of RPC under elevated

temperature and operated in streamer mode was studied by M. De Vincenzi et al. [64]. It was found that there was a permanent drop in efficiency when RPC was kept at higher temperature and voltage for a longer period of time. S.H. Ahn et al. [65] had studied the dependence of temperature and relative humidity on the bulk resistivity of bakelite plate under controlled environment. It was found that the bulk resistivity has a strong dependence on both the temperature and humidity. The resistivity decreased significantly as temperature and relative humidity were increased. Effect of temperature variation on efficiency and time resolution on streamer mode operation of RPC were investigated by M. Abbrescia et al. [66]. The experimental results showed that the effective voltage across the gap increased as the temperature was increased and as a result, higher voltage had to be applied at lower temperature to reach the efficiency plateau. It was also shown that the time resolution improved with increase in temperature.

The aim of this study is to establish the operating zone of the environmental parameters like temperature and relative humidity for safe, stable and reproducible operation of the RPCs over a significantly long time period as required for the underground experiments like the ICAL at INO. The effect of environmental temperature and humidity on the performance of RPCs, made of different electrode materials and operated in different modes, is investigated in the present work. The measurable key parameters related to the intrinsic property of the detector materials, such as bulk resistance and those related to detector performance, such as efficiency, noise rate (singles counting rate) and time resolution are measured, and their inter-dependence are investigated in an attempt to understand the systematic behaviour.

6.2 Experimental Details

Two bakelite RPCs (RPC I and RPC II) and one glass RPC of approximate size $30\text{ cm} \times 22\text{ cm}$ are operated under controlled environment in this experiment. The bakelite gas gaps are made of 2 mm thick P-120 grade bakelite plates, while the glass gas gap is made of 3.6 mm thick glass. The constructional details, specification of the materials and initial performance studies have already been described in Chapter 5. One of the major differences between the bakelite RPCs and the glass RPC is that the electrode surfaces for the bakelite RPCs are dry graphite coatings made from 99.999% pure –200 mesh graphite powder, while the electrodes of the glass RPC are made of a special resistive paint. The

surface resistivity of the bakelite RPC electrodes are fairly uniform within the range $0.8 \text{ M}\Omega/\square - 1.3 \text{ M}\Omega/\square$, while that of the glass RPC is in the range 0.7 to $1.4 \text{ M}\Omega/\square$. The measurements on the bakelite RPCs are done by operating them in both avalanche and streamer modes. The glass RPC is operated only in avalanche mode.

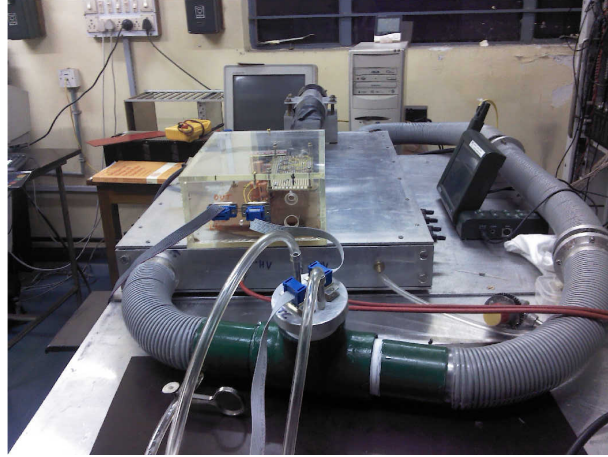


Fig. 6.1. Experimental setup

The RPCs are placed inside a sealed weather control box made of aluminium in which constant temperature and relative humidity (RH) are maintained during the measurement (Fig. 6.1). The temperature inside the box can be varied and stabilized using a blower fan and a resistive heater operated under feedback control using a PID controller with a PT100 sensor. The sensor measures the temperature inside the box which is an input to the PID controller and if the temperature is less than the set temperature, the coil starts heating up and the hot air is circulated using the blower fan. Humidity is maintained by passing moist air or dry air inside as and when needed. Temperature inside the control box was measured using another miniature PT100 sensor and the relative humidity (RH) was measured using a Honeywell HHH-4000 series humidity sensor which has an accuracy of $\pm 3.5\%$. The temperature and humidity value inside the box have been continuously monitored during the measurement using LabViewTM based data acquisition system. The calibration of the sensors are done by applying moisture continuously and increasing the temperature. For each humidity and temperature value, the sensor output is noted. The temperature-humidity recorder has been refreshed in every 0.5 minutes and the LabViewTM has been taking reading in every 10 seconds. The calibration curves of the sensors are shown in Fig. 6.2. Temperature and RH could be maintained within 0.3°C and $2-3\%$ respectively during the measurement. Electrical signals and high voltage feed-throughs, gas feed lines, blower

fan and heater enclosures, airflow ducts were sealed against permeation of moist air from outside.

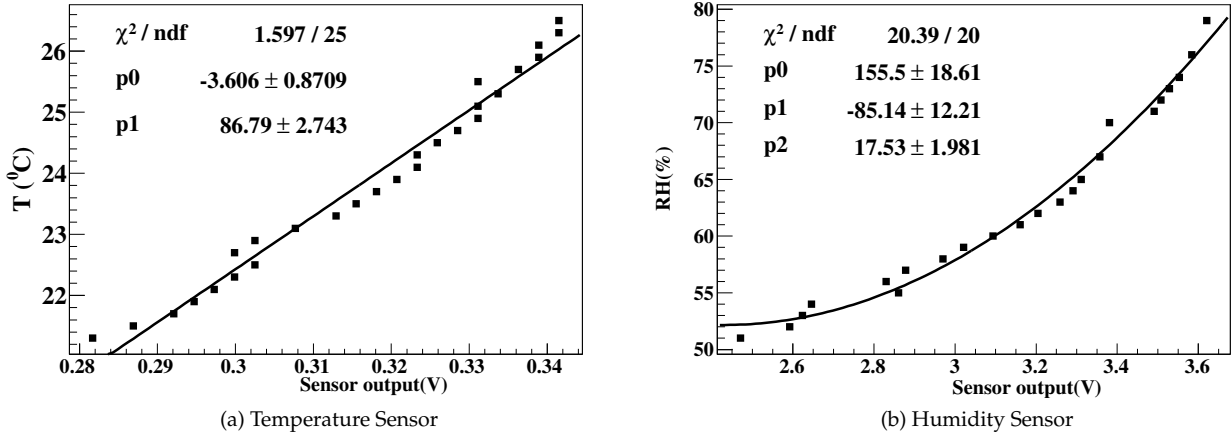


Fig. 6.2. Calibration curves for the sensors.

The Fig. 6.3 shows the schematic of the experimental set-up. The details are given in Chapter 5. Two scintillators (SC I and SC II) were placed below the RPC and one (SC III) was placed above. The coincidence between SC I (93.5 cm \times 19.5 cm), SC II (82.5 cm \times 19.5 cm) and SC III (17 cm \times 4 cm) gave the 3-fold trigger, which is the Master trigger, as the cosmic muons passed through them. Since the two adjacent strips are in coincidence with the 3-scintillator muon telescope, the signals from them are OR-ed and the coincidence between this signal and the 3-fold was taken as the 4-fold coincidence trigger.

The measurements have been carried out over 6 months at different temperatures in the range 20°C – 30°C and RH in the range 50%–70%. The leakage current of RPC I (RPC I is older than RPC II) is larger than that of RPC II and the rate of increase of leakage current as a function of temperature and humidity of RPC I is also larger compared to RPCII (Fig. 6.4). For the measurement at higher temperature and humidity, only RPC II is used. The results of bakelite RPC discussed here are obtained using RPC II. The results for temperatures 21°C, 24°C and 28°C and RH 53%, 60% and 66% are shown here. The leakage current, noise rate, efficiency and the time resolution of RPC are measured. At each voltage the data is collected for fifteen minutes for measuring noise rate and efficiency and during the measurements the temperature and RH are monitored continuously. All the measurements except timing data are taken with RPC threshold of 10 mV. Time resolution measurements are done for two different RPC

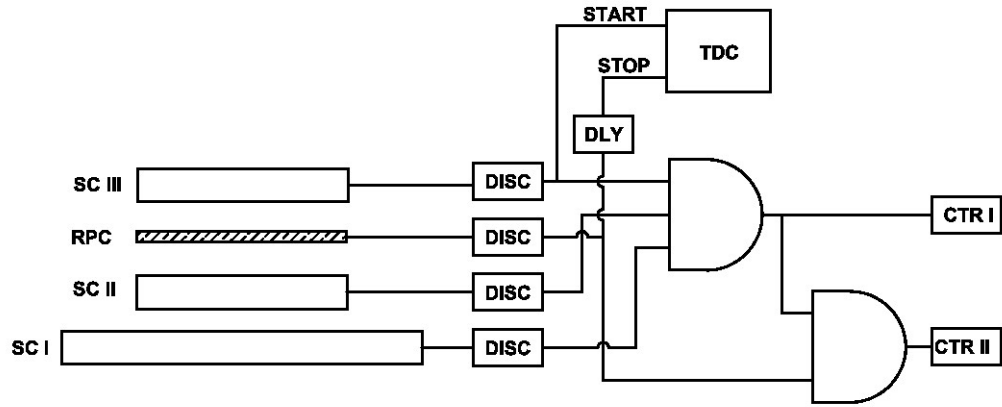


Fig. 6.3. Schematic view of experimental setup

thresholds which will be discussed later. The relative humidity and temperature as a

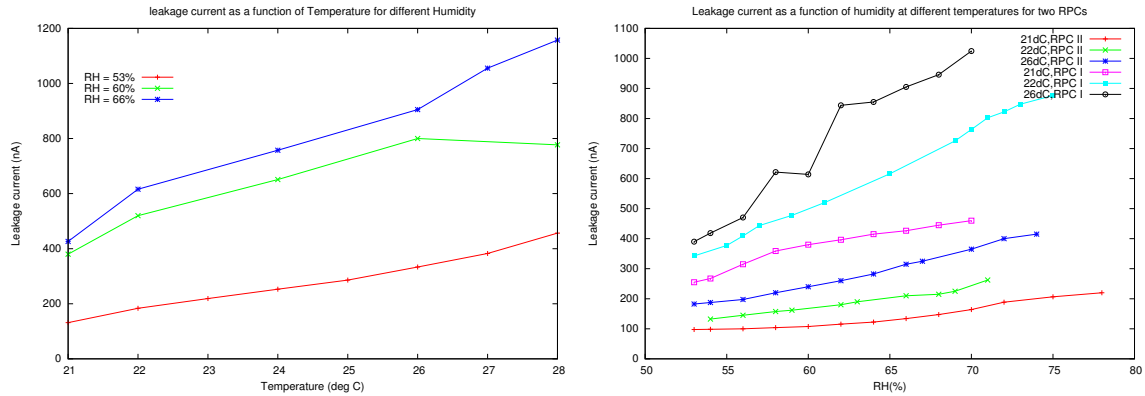


Fig. 6.4. The leakage current for different bakelite RPCs, RPC I (left) and RPC II (right) at 7.4 kV

function of time during a measurement are given in Fig. 6.5.

6.3 Results and interpretation

6.3.1 Leakage Current

Leakage current is an important parameter that is used to determine the effective potential drop across the gas gap. It is highly dependent on the variation of plate re-

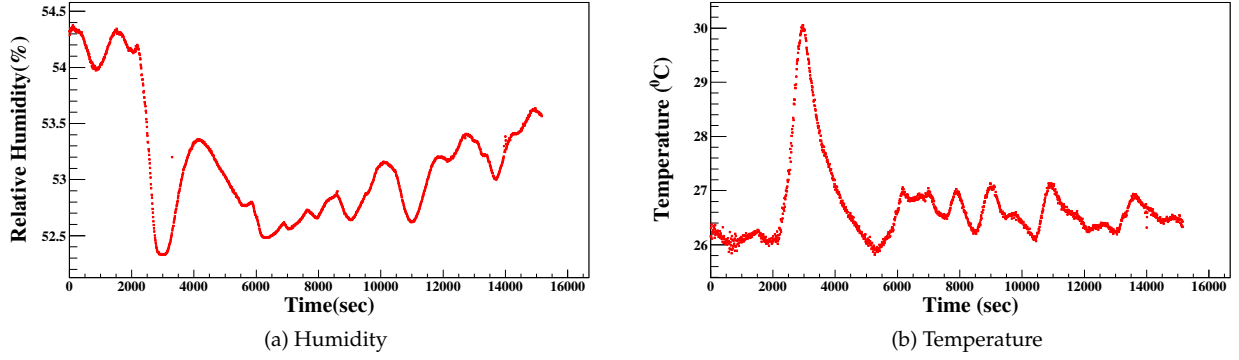


Fig. 6.5. Relative humidity and temperature as a function of time during measurement

sistance with environmental parameters. In addition, the current through the external surfaces of RPCs and the adjacent layer of air also adds to the measured leakage current. The leakage current of RPC is monitored as the applied potential difference between the electrodes is increased for different values of temperature and RH.

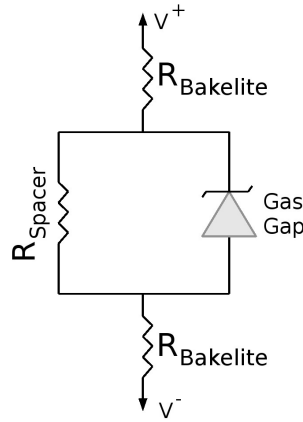


Fig. 6.6. Electrical representation of an RPC gas gap

The electrical representation of RPC is shown in Fig. 6.6. At lower voltages, the primary electrons cannot produce avalanche, so the gas gap has infinite resistance. Hence, the current flows through the spacers. Hence,

$$R_{Gas\ gap} \approx \infty, \quad (6.3.1)$$

$$\frac{dV}{dI} \approx R_{Spacer}, \quad (R_{Spacer} \gg R_{Bakelite}). \quad (6.3.2)$$

Beyond the break-down voltage, the gas starts conducting providing a low resistance

path. Then the current is determined by the electrode resistance, i.e.,

$$R_{Gas\ gap} \approx 0, \quad (6.3.3)$$

$$\frac{dV}{dI} \approx R_{Bakelite}. \quad (6.3.4)$$

A plot of leakage current as function of the potential difference (also called the $I-V$ curve) shows the typical two-slope behavior as explained above. For smaller voltage, the increase in current is less as the voltage increases. But after the knee voltage the slope changes which indicates the onset of avalanche. This results in the generation of measurable signals from the RPC. Here the data for the applied potential drop starting from this 'knee' region of the $I-V$ curve is plotted.

Fig. 6.7 shows the $I-V$ curve as explained above for 53% RH. Overall leakage current in the streamer mode is less compared to that in the avalanche mode for the same temperature and humidity. It is found that the leakage current increases with increase in temperature and humidity (Figs. 6.7 & 6.8). At higher RH (66%), the leakage currents seem to have significant fluctuations as applied voltage increases. It shows a strong dependence on RH, which is difficult to maintain constant value.

6.3.2 Plate Resistance

The slope of the $I-V$ curve for applied voltages above the knee region can be used to determine the plate resistance if the leakage resistance of the spacers is known as well as the gas in the gas gap can be considered to provide a low resistance path between the electrodes. The resistance of the spacer can be obtained from the slope of the $I-V$ curve below the knee region, where the gas is treated as an insulator with infinite resistance.

It was observed in previous studies that the bulk resistivity of the bakelite depends on external temperature and humidity [61, 65]. Since bakelite has a negative temperature coefficient [66], the bulk resistivity decreases with increase of temperature. It was also shown that the bulk resistivity reduces with increase in humidity [65]. The Figs. 6.9 and 6.10 show the variation of the plate resistance as a function of temperature and humidity respectively both in streamer and in avalanche mode. It is found that the resistance decreases with the increase in temperature and more marginally with humidity.

The electrode plate resistance decreases from $\sim 6G\Omega$ to $\sim 3G\Omega$ as temperature in-

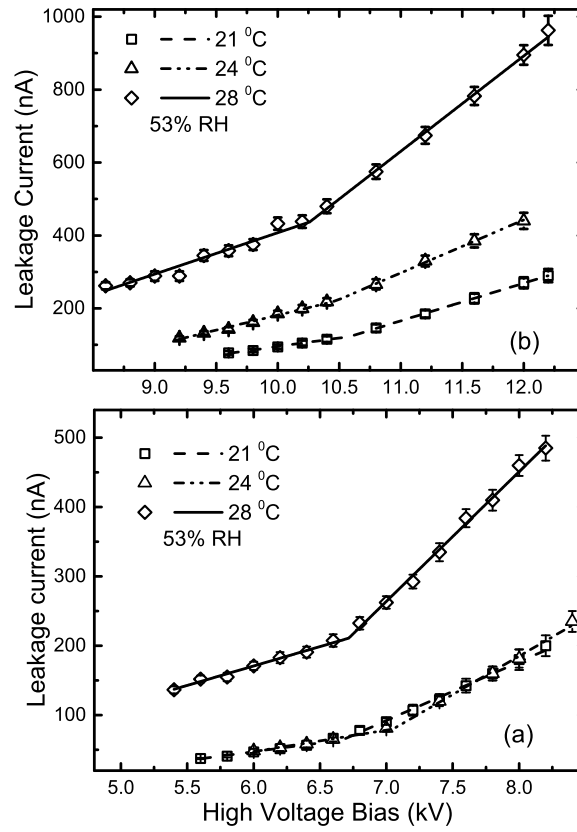


Fig. 6.7. Leakage current as a function of voltage at 53% RH for different temperatures for (a) streamer, and (b) avalanche modes of operation. Lines are drawn through the data to indicate the trend.

creases from 21°C to 28°C for 53% RH. Similarly, it decreases from $\sim 6\text{G}\Omega$ to $\sim 4\text{G}\Omega$ as RH increases from 53% to 66%. The resistance of the bakelite plate is dependent more on temperature than on humidity. At higher temperature (eg. 28°C), the plate resistance is found to be almost independent of relative humidity.

Variation of plate resistance with temperature is found to be more prominent in the streamer mode operation than in the avalanche mode. However, for both the modes, the variation appears to be less prominent at relative humidity 66%. At this humidity value the average resistance is consistently less than that at lower humidity values.

This behaviour can be due to the decrease of plate resistance with increase of temperature and increase of RH as discussed in the previous section. The decrease of plate resistance with increase of RH indicates that there can be permeation of moisture into the bulk of bakelite paper laminates through the external surfaces. The leakage current can increase due to the surface leakage which provides a parallel leakage path. Then the leakage current is expected to increase with the increase of temperature and

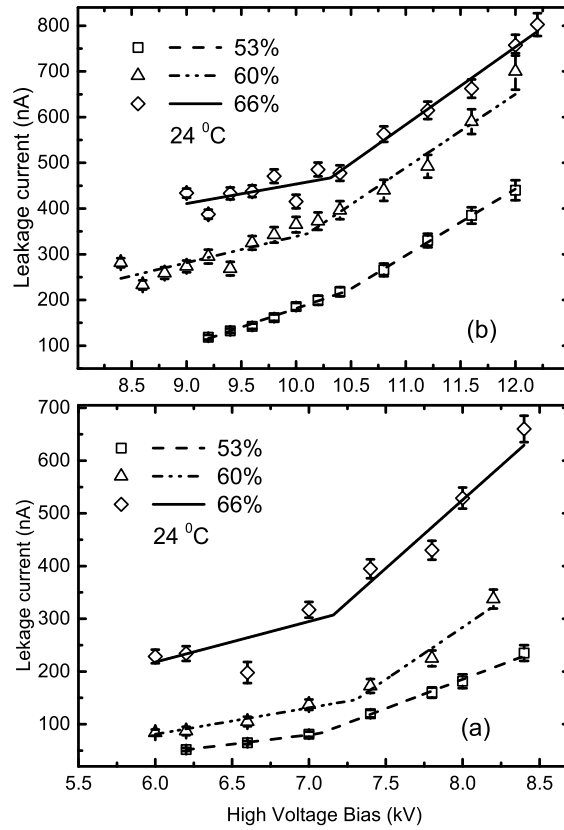


Fig. 6.8. Leakage current as a function of voltage at 24°C at different RH values for (a) streamer, and (b) avalanche modes of operation. Lines are drawn through the data to indicate the trend.

the RH. Such surface leakage can also contribute to spurious discharges which can increase the noise rate. A comparative study of the dependence of noise rate on the environmental parameters reasonably correlates with this observation. The details will be presented in the following sub-sections.

6.3.3 Noise Rate

The noise of RPC is caused mostly by spurious discharges or sparks. This also includes signals from cosmic rays and other background events. Such sparks may take place within the gas gap due to the non-uniformities present on the inner electrode surfaces. It may also take place on the external faces of the gas gap, which are in contact with the environment. The properties of the pulses caused by such sparks are very similar in nature to the genuine pulses caused by the passage of cosmic charged particles through the RPC. The demand of fast coincidence (with time coincidence window set to as low as possible) between the RPCs on a stack mostly filters out the spurious events caused by the sparks. However, the noise rate must be kept as low as possible. The sensitivity

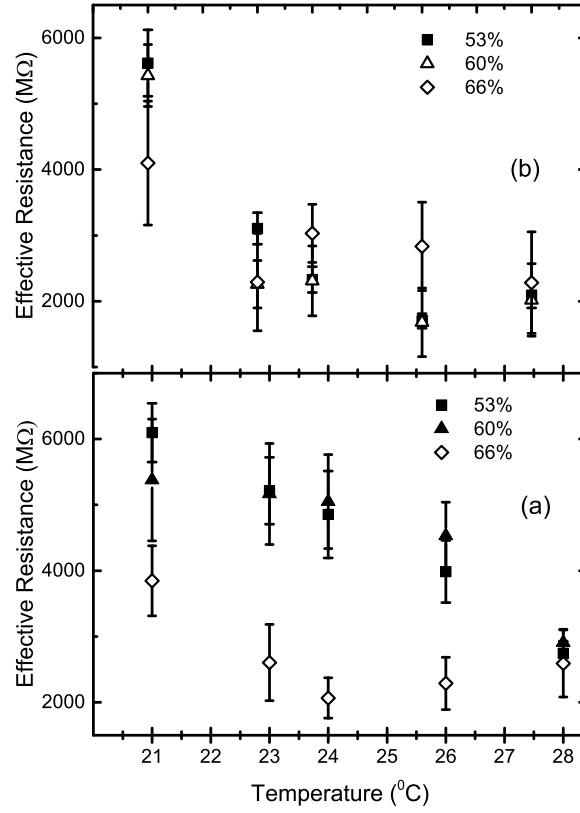


Fig. 6.9. Plate resistance as a function of temperature for different RH values for (a) streamer, and (b) avalanche modes of operation.

of the RPC noise rates to the variation of environmental parameters has to be closely monitored for stable and long term operation of the RPCs.

As explained earlier, the OR of the pulses from the two adjacent RPC strips, recorded for a single event, is counted for measuring the noise rate. At each applied bias voltage, the data is taken for 15 minutes duration. The RPC area covered in this set-up is $\sim 28 \text{ cm} \times 4 \text{ cm}$. The noise rate is measured as a function of the applied bias voltage for different temperatures and RH. The results for both the modes of operation are plotted as function of the RPC bias voltages for different temperatures for a given RH in the Fig. 6.11. Similar graphs are also plotted for different RH values at a given temperature.

For a particular RH value, the noise rate is found to increase with temperature both in streamer and avalanche modes of operation (Fig. 6.11a and b). The dependence is

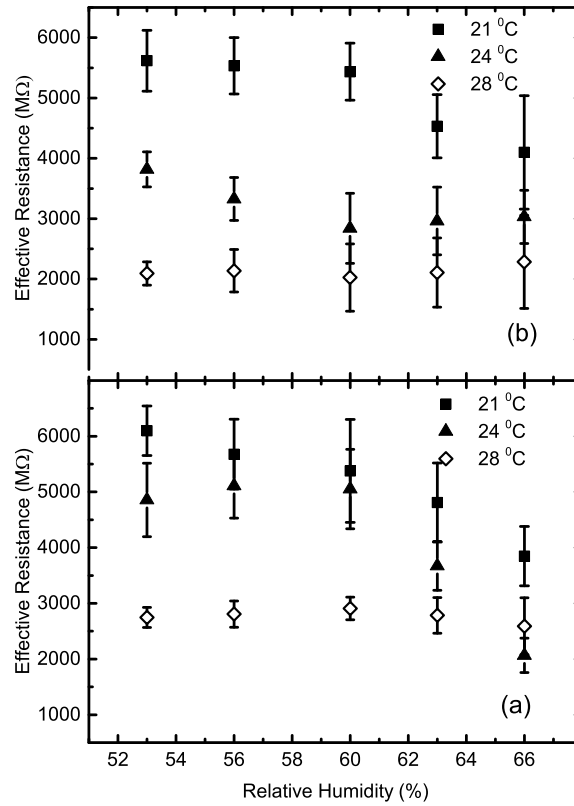


Fig. 6.10. Plate resistance as a function of RH at different temperatures for (a) streamer, and (b) avalanche modes of operation.

nonlinear and more visible above the knee voltage (~ 6.5 kV in streamer mode and ~ 9.5 kV in avalanche mode). Below the knee voltage region, the noise rate is found to be independent of temperature and RH for both the modes of operation. Above the knee voltage, discharges start taking place in the gas gap, which is reflected in the increase of leakage current following a faster slope (dI/dV) of the $I - V$ curve (Figs. 6.7 & 6.8).

Correlation of noise rate with the plate resistance can be physically explained as follows. The discharges taking place in the gas gap result in temporary neutralization of charges on the inner electrode (anode). These charges are quickly replenished from the connected voltage source to bring the electrode back to its normal configuration. The recovery time depends on the plate resistance. Thus, a decrease in plate resistance results in decrease of recovery time because of which the noise rate increases.

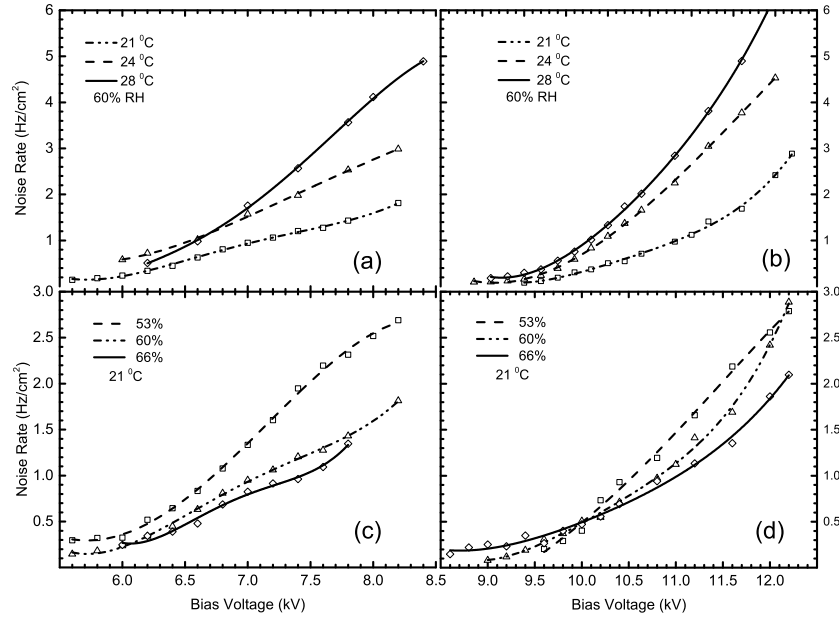


Fig. 6.11. Noise rate as a function of applied voltage at the same RH for different temperatures for (a) streamer and (b) avalanche modes of operation. The same is plotted at the same temperature (21 °C) for different RH (c) streamer and (d) avalanche modes of operation. Lines drawn through the points indicate the trend of the experimental data.

It is found that the variation of noise rate with applied bias voltage is more prominent at the highest temperature (28° C) for both the modes of operation. As explained before, increase in the noise rate is due to more discharges taking place in the RPC. It is, therefore, not desirable to operate the RPCs at higher temperature. An upper limit of 24-26 °C appears to be a reasonable limit for stable operation of the RPCs.

It is also observed that the noise rate decreases as RH increases (Fig. 6.11 c and d) for both the modes of operation. For increase in RH from 53% to 66% at a fixed temperature, the noise rate decreases almost by a factor of 2 at the typical operating bias voltage ($\sim 7.5 - 8$ kV) for the streamer mode, while the decrease is by $\sim 50\%$ under similar situation for the avalanche mode operation. But, plate resistance cannot be correlated with this observed effect. Permeation of moisture into the bulk of RPC bakelite electrodes can reduce the plate resistance as RH increases, and therefore, will result in increase of noise rate with increasing RH values. This is contrary to what has been observed.

The anomalous dependence of noise rate on RH is most likely to be due to the contribution of spurious discharges taking place on the external surface of the RPC gas gap. In the presence of moisture in the ambient air, a continuous charge leakage may occur between the electrodes externally resulting in an increase of the measured

leakage current. The effect would be more prominent at higher RH. As a result, the other mode of discharge that contributes directly to the noise rate, viz., the possibility of multiple spurious discharges that occur due to build-up of charges at portions of the inside electrode surfaces with increased curvatures or sharp points, would be reduced. However, for the bakelite RPCs operating in both the modes, the noise rate is more sensitive to variation of temperature rather than on RH.

Based on the observations from this experiment, it can be concluded that, though the bakelite RPCs can be safely operated for humidity values up to $\sim 66\%$ at the cost of increase of leakage current and the subsequent power dissipation in biasing the RPCs, it is better to operate the RPCs at relatively lower RH ($\sim 52-55\%$) for significant power saving.

6.3.4 Efficiency

Detection efficiency of the RPC is the most important characterization parameter that establishes suitability of it for the targeted experiment. The quality of the reconstruction of an event is determined by the number of RPC layers crossed by the particle. The efficiency is strongly related to the applied bias voltage across the gas gap. As the applied bias voltage is increased, the electrons produced by primary ionization lead to increase of secondary ionization and reduces recombination of the electrons and ions. The amplitude of signal induced in the pick-up panel also increases with applied bias. Since the amplitude increases, the signal is induced starting from the low voltage plateau decided by the signal discrimination threshold. This occurs as a function of the bias voltage until it reaches the high voltage plateau or efficiency plateau region corresponding to the maximum of efficiency, acceptable at values $\geq 90\%$.

The efficiency, defined as the ratio of 4-fold (RPC coincidence signal) to 3-fold (master trigger), is measured using the cosmic muon telescope set-up described in Section 6.2. The efficiency is measured while increasing the high voltage bias of the RPC. At each voltage, the data are collected for 15 minutes, and the measurements are repeated for different values of temperature and humidity.

The efficiency, plotted as a function of applied voltage for different temperatures, is shown in Fig. 6.12 for 53% RH value. The dependence on temperature is more prominent in the avalanche mode than in the streamer mode. In operation with both the modes, the bias voltage at which the efficiency plateau is reached is higher at lower temperatures. This behaviour is due to the dependence of bakelite resistance on tem-

perature. The effective voltage across the gap is determined by the plate resistance. Because of negative temperature coefficient of bakelite resistivity, the effective voltage across the gas gap is more at higher temperature ($V_{eff} = V - R_+ I - R_- I$, where V is the applied bias voltage and R_{\pm} are the bulk resistance of the respective bakelite electrodes).

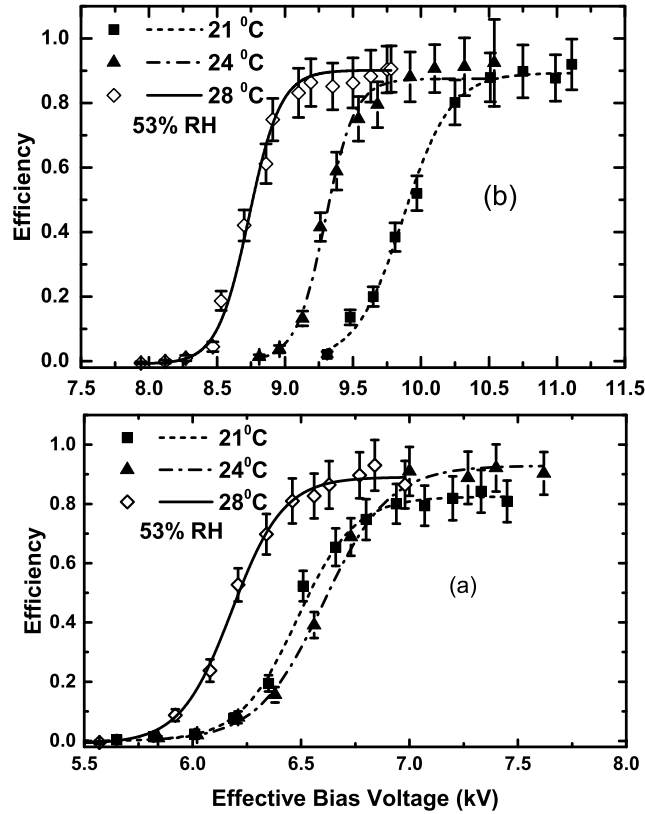


Fig. 6.12. Efficiency as a function of voltage for the same RH at different temperatures for (a) streamer and (b) avalanche modes of operation.

The efficiency as a function of applied voltage for different RH values at a fixed temperature (21° C) are plotted in the Fig. 6.13. The behaviour is found to be similar. For lower value of RH, the efficiency plateau is reached at higher bias voltage. For example, at 53% RH, the voltage at which the efficiency reaches a plateau is ~11 kV, whereas at 66% RH, it is ~10.3 kV in the avalanche mode. The effect is similar for the streamer mode operation, where the difference in bias voltage at which efficiency plateau is reached at 53% and 66% RH values is ~ 1 kV. This is also due to the total

voltage drop occurring across the two electrodes because of the variation in the plate resistance. The leakage through the bulk or the outer surface can also affect efficiency which has to be studied in detail. An increase in surface leakage current due to increase in RH results in decrease of potential drop across the gas gap and hence can reduce noise rate. This can also contribute to the change in efficiency.

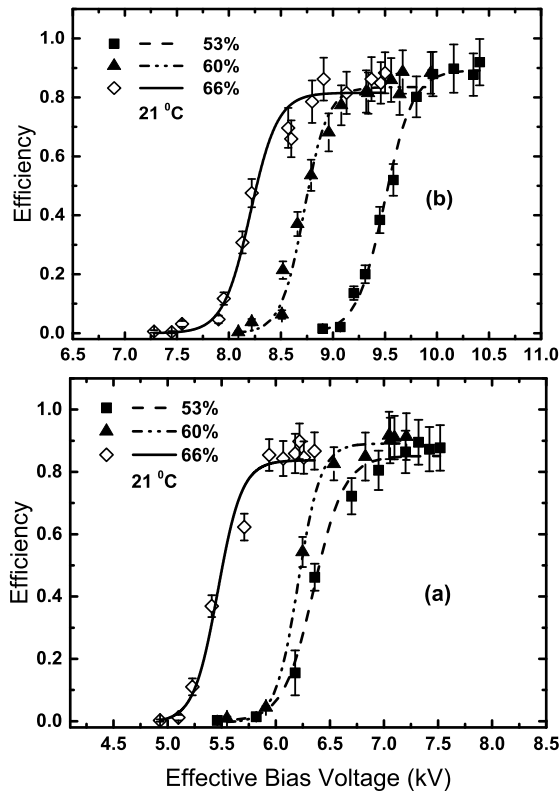


Fig. 6.13. Efficiency as a function of voltage for the same temperature at different RH values for (a) streamer and (b) avalanche modes of operation.

6.3.5 Time Resolution and Arrival Time

The time resolution of a detector determines the accuracy of the measurements of the time at which the particle crossed the detector. The dead time of the detector is the minimum time separation between two hits. The fluctuations in the timing response of the detector, the time spread coming from the electronics etc., affect the time response of the detector. The time resolution is one of the crucial parameters of a tracking detector.

In the case of ICAL detector of INO [26], where the direction of muons (whether up going or down going) needs to be precisely known for probing the matter effects of neutrinos, the time resolution of RPCs play an important role. The schematic diagram of the time resolution measurement set-up is shown in Fig. 6.3. The same set-up was used for time resolution measurements of the RPCs operated in streamer mode and reported earlier [71] The RPC is operated in avalanche mode for this study.

A Phillips Scientific 7186 Time to Digital Converter (TDC) is used for the measurements. The trigger signal from the finger scintillator (SCI III) is taken as the START signal of the TDC and the signal from one strip of RPC is taken as the STOP signal. The TDC calibration is found to be 0.1 ns/channel. The TDC calibration curve is shown in Fig 6.14. The time spectra of the RPC are measured for different temperature and humidity values at fixed voltage 12 kV and with two different RPC signal threshold (10 mV and 70 mV). The measurements have been repeated three times for each threshold setting and the duration of each run has been fixed as an hour. The time spectrum is fitted with Gaussian distribution to find out the mean and the standard deviation of the distribution. The mean is taken as the average arrival time(T), and the standard deviation of the distribution is the time resolution(σ_{time}).

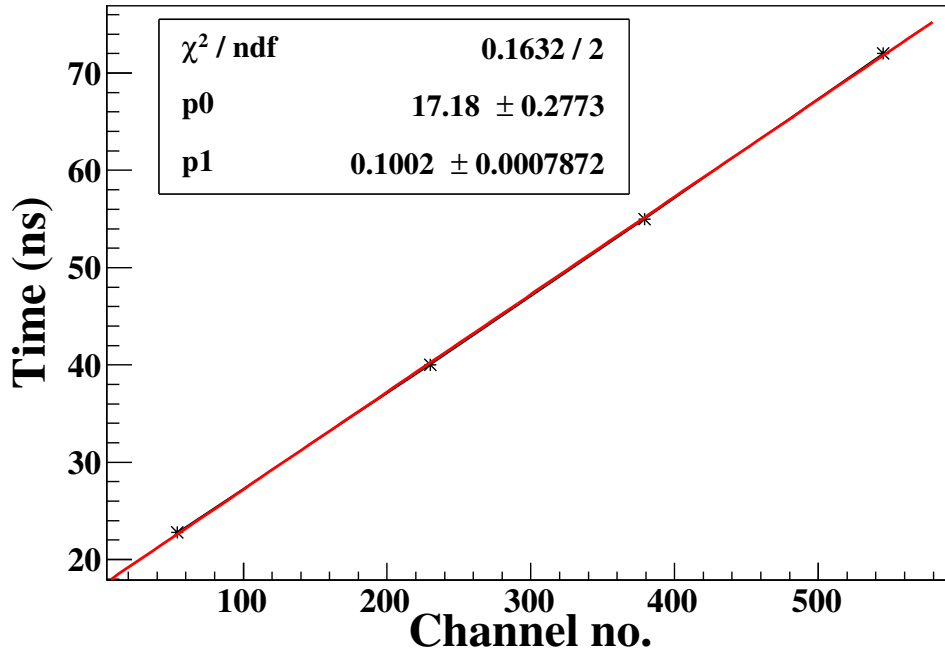


Figure 6.14. TDC Calibration curve.

The distribution of the time difference between the master trigger and the signal

from one RPC strip fitted with Gaussian distribution is shown in Fig. 6.15.

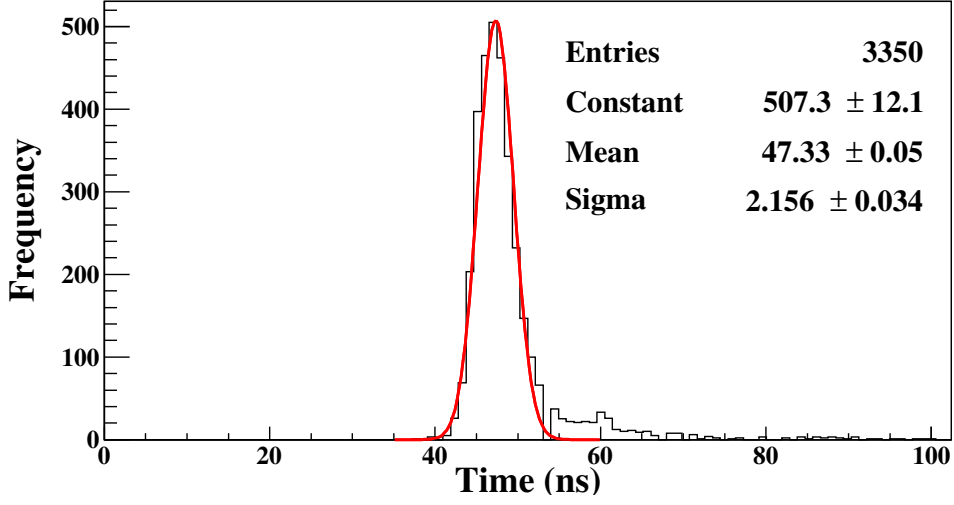


Figure 6.15. The distribution of the time difference between the RPC and the master trigger.

The average arrival time (T) is the sum total of (a) the difference in time delay (ΔT_{dly}) between the triggers from the scintillator and the RPC pick-up strip, (b) time (ΔT_{av}) elapsed in the evolution of avalanche to register a pulse in the pick-up strip, and (c) the travel time (ΔT_v) of the incident particle from the finger scintillator to the RPC. However, $\Delta T_v \ll \Delta T_{\text{dly}}$ or ΔT_{av} . The time delay ΔT_{av} is related to the drift time of the electrons inside the gas gap.

The average arrival time and time resolution (σ_{time}) as a function of temperature for fixed relative humidity of 53%, are shown in Figs. 6.16 (a) and 6.16 (c) respectively. The arrival time is decreased by $\sim 5 - 10\%$ as temperature is increased for both the thresholds. For 10 mV RPC signal threshold, the time resolution improved to 2.15 ns at 28°C from 2.85 ns at 21°C. The time resolution is nearly constant for all the temperatures for 70 mV threshold. As described earlier, the resistivity of the bakelite decreases as the temperature increases. This results in the increase of effective voltage across the gas gap with temperature. The drift velocity of the electrons increases. This can be the reason for the improvement in time resolution and the decrease in the arrival time as temperature increases. Similar behaviour has been reported earlier [66].

The time delay ΔT_{av} is dependent on the drift time of the electrons, which is typically $\sim 12 - 16$ ns for the 2 mm gap of RPC [74]. From the Fig. 6.16 it is clear that the estimated ΔT_{av} makes only $\sim 30\%$ contribution. Hence, the dependence of the arrival time on the environmental parameters is most likely to be due to both ΔT_{av} and

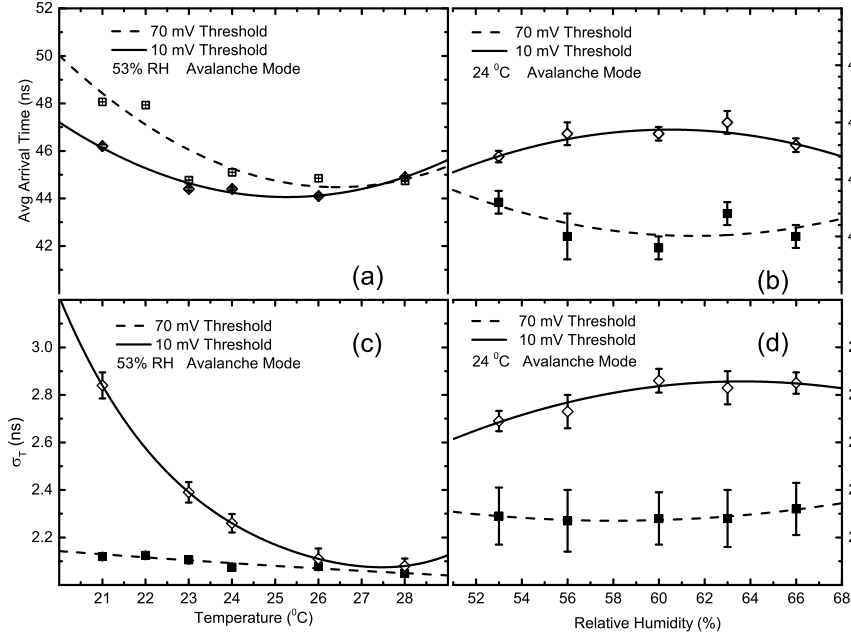


Fig. 6.16. Plots of (a) average arrival time T and (c) time resolution σ_{time} as function of temperature, measured for the avalanche mode operation of the RPC at 53% RH. The same observable parameters are plotted in (b) and (d) respectively as function of RH at 24°C temperature.

ΔT_{dly} . The ΔT_{dly} depends on the properties of the signal cables and the pick-up strip materials such as permittivity, dimension, etc. The detailed study of these properties with external environmental parameters need to be done in order to understand the behaviour of the ΔT_{dly} as a function of temperature.

The propagation delay of the pick-up strip can be calculated using the stripline impedance model for the pick-up strips. For a stripline transmission line, the relation between the propagation delay τ_d and the permittivity of the medium is given as follows[75]:

$$\tau_d = A\sqrt{B\epsilon_r + C}, \quad (6.3.5)$$

where ϵ_r is the dielectric constant of the medium, A , B and C are suitable constants. The temperature dependent variation of permittivity of the dielectric medium may be a reason for variation of the propagation delay with temperature. An estimate of temperature dependence shows that for a $\sim 10\%$ variation of ϵ_r , the propagation delay would change by $\sim 3\%$. This is clearly not enough to account for the variation of the average arrival time ($\sim 10\%$) with temperature as observed in our experiment over a temperature range of 20 – 30°C. Therefore, it is expected that the variation of electron drift time with temperature is the possible cause of variation of the arrival time. A de-

tailed study of the temperature dependence of electron propagation in the avalanche through simulation, using realistic electric field distribution, will be necessary to understand this effect. This is beyond the scope of this thesis.

The T and the σ_{time} , as functions of RH at 24°C, are shown in Figs. 6.16b and 6.16d. Within uncertainty limits, the parameters are found to be nearly constant for different RH for a particular temperature. There is a small ($\sim 10\%$) increase in σ_{time} as the RH increases. The decrease in plate resistance (see Fig. 6.10b) as RH increases results in increasing the effective bias voltage across the gas gap. Thus the drift velocity increases and hence the time resolution improves. Also, it is found that the noise rate is decreased marginally with increase in RH (see Fig. 6.12c and d), which does not support increase in σ_{time} due to addition of random noise within the coincidence window. Detailed study has to be done in order to understand this apparently anomalous behavior. Again this is beyond the scope of this thesis.

6.4 Glass RPC in Avalanche Mode

The tests with glass RPC are done only in avalanche mode. The RPC is placed in the same set-up as described in the Section 6.2. The threshold of the RPC is set to 10mV. The pulse height is $\sim 400\text{mV}$ which is lower compared to the bakelite RPCs in avalanche mode. The overall noise rate is also decreased. The measurements are done with different values of temperature and humidity.

By fixing humidity at 53%, measurements are done for three values of temperature. The efficiency and noise rate plotted as a function of voltage is given in Fig. 6.17. As compared to bakelite RPC the dependence of glass RPC on temperature is smaller. But the behavior is same as that of bakelite RPC. The voltage at which efficiency reaches plateau is higher for smaller temperature and the noise rate is slightly higher for larger temperature. As explained in the Section 6.3.4, this might be due to the increase in effective voltage for higher temperature.

At fixed temperature $T = 24^\circ\text{C}$, the measurements are done for two humidity values 53% and 60%. The results are shown in Fig. 6.18. The leakage current of the RPC was going up when the humidity was increased further. The noise rate also increased when the humidity increased. The efficiency does not show any dependence on humidity. But unlike the bakelite RPC, the noise rate increases with humidity.

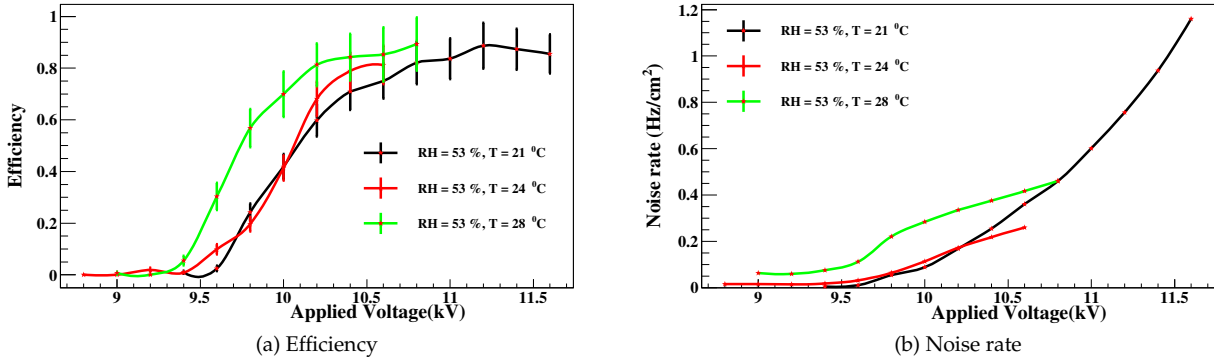


Fig. 6.17. Efficiency and noise rate as a function of voltage for different temperature at RH = 53%

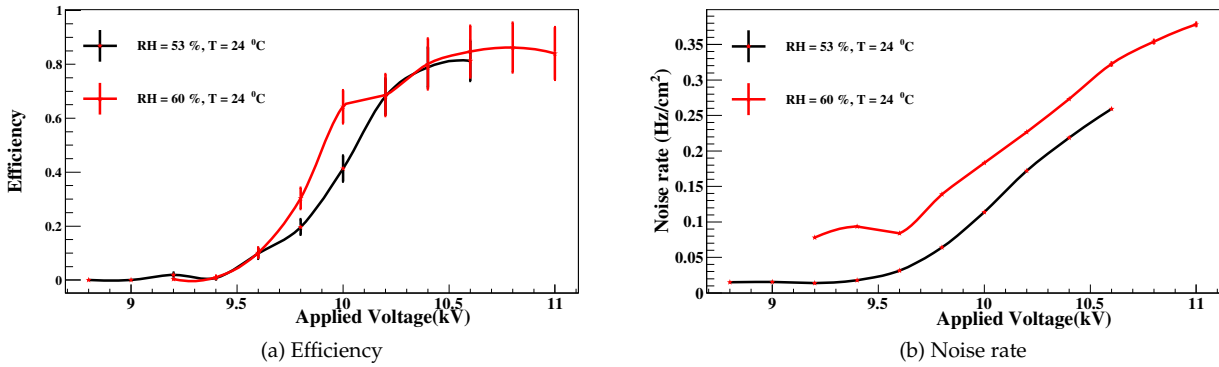


Fig. 6.18. Efficiency and noise rate as a function of voltage for different humidity for T = 24 °C

6.5 Summary

The performance of two bakelite and one glass resistive plate chambers under different environmental temperature and relative humidity was studied. The temperature was varied in the range (21 – 28)°C and relative humidity was varied between 53% and 66%. The bakelite RPCs were operated in both the avalanche and the streamer modes for comparative study of their sensitivities to the environmental parameters and the glass RPC was operated only in avalanche mode. A preliminary study on the dependence of glass RPC on the external environmental parameters was also done. But further investigations have to be done in order to understand the behaviour of glass RPC under different conditions.

From the detector leakage current measurements, the plate resistance (R_p) of the bakelite as function of temperature and relative humidity was determined. The equivalent circuit model of RPC operation was used for this. The plate resistance was found to decrease with increase in temperature and relative humidity. The sensitivity of the

plate resistance to the environmental parameters was found to be more for avalanche mode than the streamer mode of operation. The noise rate was relatively larger in the avalanche mode than in the streamer mode and it was found to increase with increase in temperature. The dependence is visible above the 'knee' voltage, which is ~ 6.5 kV for the streamer mode operation and ~ 9.5 kV in the avalanche mode operation. The noise rate was found to decrease as the relative humidity was increased, though the dependence on relative humidity was less compared to that on the environmental temperature. The detection efficiency of both the bakelite and glass RPCs was nearly 90% in the plateau region for operation in the streamer mode and also in the avalanche mode. The voltage at which the efficiency reached the plateau decreased as temperature was increased, which can be due to the decrease in the plate resistance of the RPC, leading to the increase of effective voltage.

The average arrival time and the time resolution were measured at the fixed RPC bias voltage of 12 kV, using coincidence with a plastic scintillation detector. This is done for two different RPC voltage pulse threshold values. The data were taken by varying the temperature from 21°C to 28°C at 53% RH condition and the humidity is varied from 53 – 66% at constant constant temperature 24°C . It is observed that the average arrival time decreased as temperature was increased for both the signal threshold values. For 10 mV threshold time resolution (σ_{time}) decreased from 2.9 ns to 2.1 ns as the temperature was increased, whereas for 70 mV threshold, it remained nearly constant around 2.1 ns. The arrival time is not affected much by the environmental humidity, however, the time resolution (σ_{time}) had worsened by 10% with increase in relative humidity.

It was observed that most of the bakelite RPC parameters were relatively sensitive to the temperature, rather than relative humidity. The dependence was more prominent for the avalanche mode of operation rather than for the streamer mode. Operation of the bakelite RPC detector was found to be reasonably stable at the temperature around $21\text{--}25^{\circ}\text{C}$ and relative humidity $\sim 53\text{--}60\%$. The dependence of noise rate on the relative humidity was not fully understood and needs further study.

This study is part of an on-going attempt to characterise the bakelite RPCs and determine the optimum environment for the stable operation of the RPCs over the large times required of an experiment such as ICAL. While bakelite RPCs have been fabricated and tested earlier, some of the studies on temperature and humidity dependence

are new. The behaviour of the efficiency and the plate resistance as a function of temperature has been studied earlier elsewhere; however, the impact of humidity on the noise rate has been investigated for the first time. In addition, the optimum operating environment vis a vis the location of ICAL in a tropical area is expected to be different from that of RPCs operating elsewhere in the world. This has also been investigated for this reason.

Part III

Summary and future outlook

Summary and Future Outlook

This thesis contains a simulations study of some of the physics reach, detector response to muons and R&D for active detector elements (resistive plate chambers) of the massive magnetized Iron Calorimeter (ICAL) detector (see Fig. 2.2 for a schematic view) to be built at the proposed India-based Neutrino Observatory for studying atmospheric neutrinos. It will be placed in an underground cavern at Bodi West Hills, Tamilnadu, and will have a minimum 1 km of rock overburden in all direction, which will shield the detector from the low energy cosmic ray background.

The main goals of ICAL include, the precision measurements of the neutrino oscillation parameters and determination of neutrino mass hierarchy using the matter effects differentially experienced by neutrinos and anti-neutrinos while passing through the Earth. The neutrino oscillation probability is sensitive through matter effects, which are prominent in the few GeV energy region of atmospheric neutrinos, to the neutrino oscillation parameters. This can be determined by measuring the energy and the path length traveled by neutrinos.

Neutrinos and anti-neutrinos interact differently with matter depending on the mass hierarchy. By observing the ν and $\bar{\nu}$ events separately the hierarchy can be determined. This is achieved by observing the charged leptons (primarily muons) produced in charged current (CC) interactions of the neutrinos with ICAL. Here we focus on muons since the ICAL detector is optimized to study the energy, direction, and charge of muons.

When ν_μ interacts with the detector, μ^- is produced while $\bar{\nu}_\mu$ gives μ^+ in the detector. Since ICAL is a magnetized detector it can distinguish between μ^- and μ^+ events and hence ν_μ and $\bar{\nu}_\mu$ events can be separated. In order to measure the neutrino oscillation parameters precisely, the energy and angle of muons arising from these neutrino

interactions have to be measured accurately.

Hence a detailed study of the muon response of the detector in the few GeV energy region is crucial for determination of the physics capability of ICAL.

In the first part of this thesis, a simulation study of the response of the ICAL detector to muons was presented. A GEANT4-based code was used to describe the detailed geometry of ICAL; in addition, a simulated magnetic field map was used both to propagate the particles in the detector and generate the charged-particle tracks as well as help with the reconstruction. A Kalman-filter-based code was used to determine the muon track curvature and hence its energy/momentum and the sign of its charge. In particular, the momentum reconstruction efficiency, charge identification efficiency, momentum and angular resolution of muons were calculated in the central regions of the ICAL detector, where the magnetic field is uniform and constant (see Fig. 2.3).

Initially, muons with fixed momenta and directions (azimuthal angles were smeared over while keeping the polar or zenith angle fixed) were propagated from fixed vertices in order to understand the response of the detector with respect to its dead spaces such as support structures where there is no magnetic field, coil gaps where the copper coils that would generate the magnetic field would be placed, etc. After this, the muon response with fixed energy and zenith angle was studied in the entire central region.

It was found that the simulated ICAL has a very good direction resolution, better than a degree, over most of the range of energy and zenith angle, and that the response was similar for both μ^+ and μ^- . The momentum resolution is about 9–14% while the reconstruction efficiency is about 80% in most of the regions. The relative charge identification efficiency for most of the energies is about 98% (See Figs. 3.14, 3.18, 3.19, 3.21 and 3.22). Hence these studies indicate that ICAL is suitable for studying neutrino oscillations through the CC muon channel in atmospheric neutrinos. In fact, these results have already been used to find the sensitivity of ICAL to the neutrino oscillation parameters and mass hierarchy [24, 37, 38].

Later on, studies of the muon response in the peripheral regions of the detector were conducted. Here the magnetic field strength is less compared to the central region and is nonuniform, so the results are slightly worse than in the central region. Additional selection criteria were devised to improve the performance of the detector in these regions; details of this study are not part of this thesis. A detailed study of the physics reach of ICAL using these complete results is underway; in the mean-

while, these results are also useful to study cosmic ray muons which form the major background to the oscillations physics studies. The high energy cosmic ray muons in particular are interesting in their own right since the cosmic ray muon charge ratio has important implications for understanding primary cosmic ray interactions as well as in determining atmospheric neutrino fluxes more precisely at high energies (few 100 GeV). The study of these high energy cosmic ray muons form the next component of this thesis.

The sensitivity of ICAL to the atmospheric muon charge ratio was investigated. These cosmic ray events can be separated from the atmospheric neutrino events using the event topology since the former enter the detector from one of its 5 faces (except the bottom) from outside while the muons produced in CC interactions of atmospheric neutrinos are generated inside the detector. Having an excellent charge identification efficiency, ICAL can distinguish between μ^+ and μ^- in the secondary cosmic rays. A code was developed to generate the cosmic ray muon spectra at the ICAL detector site and study the sensitivity of ICAL to the muon charge ratio.

For this study, the cosmic muon energy and angular spectra at sea level were generated separately for μ^+ and μ^- according to the modified Gaisser's formula (so-called "pika" model, Eq. 4.4.1). These muons were then propagated through the rock to the detector using Bethe-Bloch energy loss formulae. The slant depth or distance traversed by the muons before they reach the detector is calculated using the topographical map of the Bodi West Hills. Typically only muons having surface energy above 1600 GeV reach the detector. At the detector, muons with energies up to 100 GeV were considered for the analysis; above 100 GeV, the charge identification efficiency reduces below $\sim 97\%$ and additional corrections due to charge misidentification need to be considered.

These events were propagated through the ICAL detector and reconstructed for their momenta and direction (E, θ, ϕ) . The inverse process was used to propagate the reconstructed muons back to the surface and determine their surface energy and zenith angle. The muon charge ratio was then calculated as a function of the zenith angle and surface muon energy. It was found that an efficiency correction improves the reconstructed charge ratio so that it is the same as the theoretical (input) value within statistical fluctuations. The study showed that ICAL has a very good sensitivity to the atmospheric muon charge ratio in the surface muon energy range from 1.6 TeV to 10

TeV (See Figs. 4.6 – 4.11). The sensitivity to charge ratio for energies greater than 10 TeV can also be probed with a larger data set, by including events in the detector with energies beyond 100 GeV; this study will be part of a future work.

The second part of the thesis consists of an experimental study where the operation of resistive plate chambers were investigated. For the underground experiments like ICAL, the stable and long term operation of the detector is very crucial. Two bakelite RPCs were fabricated and the dependence of the performance of the RPCs on the external temperature and relative humidity was studied in detail. Preliminary studies of glass RPCs were also conducted. The bakelite RPCs were operated both in avalanche mode and streamer mode whereas the glass RPC was operated only in avalanche mode. The RPCs were tested using a cosmic ray test setup. The RPCs were placed inside a box where a constant temperature and humidity could be maintained during the measurement. The temperature was varied in the range 21–28°C and the relative humidity was varied between 53% and 66%. The parameters like leakage current, noise rate, plate resistance, efficiency and timing characteristics of RPCs were measured for different values of temperature and humidity.

It was found that for bakelite RPCs, the leakage current increases with increase in temperature and humidity. Using the leakage current values, the plate resistance of bakelite as a function of temperature and humidity was calculated. The bakelite resistance decreases as the temperature and humidity increase, which can be the reason for the increase in the leakage current. The noise rate of bakelite RPC was found to increase with temperature, but decrease with the increase in humidity. For all temperature and humidity values the efficiency of RPCs in the plateau region was about 90%, both for bakelite and glass RPCs. The time resolution and the arrival time were found to decrease slightly as the temperature increased for lower RPC threshold. At higher threshold, the time resolution value is independent of the temperature. Though the arrival time is not affected by the increase in humidity, the time resolution slightly worsened as humidity increased (See Figs. 6.7 – 6.13, 6.16).

The effect of temperature variation on the performance of RPC is more prominent compared to the humidity. The operation of bakelite RPCs is found to be stable at the temperature around 21–25°C and relative humidity ~ 53–60%.

7.1 Open issues and future work

The low energy cosmic rays are a background to the neutrino events in the ICAL detector. The vertex of the neutrino events are inside the detector while the cosmic ray muons enter from outside. Hence the cosmic ray events can be separated from neutrino induced events using the event topology. But the separation of these events is not perfect because of the efficiency of the RPC, which is about 95% and the RPCs at the edge of the detector may not give signals from the cosmic ray muons. The effect of this background can be studied as an extension of the current work on cosmic ray muons.

The very high energy cosmic ray muons (\sim PeV) lose energy as they pass through rock and reach ICAL with 10–100 TeV energies. They pass through the detector without bending in the magnetic field, but produce $e^+ - e^-$ pairs which generate cascades that are distinct from lower energy muons tracks or even hadron showers. These so-called “pair-meter” events can be separated from other cosmic ray events and neutrino events. This can also be studied in detail.

The anomalous behaviour of the humidity dependence on RPC noise rate variation as observed in the course of this work, needs more detailed investigation as well as simulation studies which will be taken up in future. Though a preliminary study of performance of glass RPCs under variable environmental conditions was attempted in course of this work, a detailed study is also required.

Finally, the simulation study of the muon response of the detector needs to be validated against data. The data from the ICAL prototype detector which will be operational soon, can be used for this, although it would be ideal to use suitable test beams for this validation. The cosmic ray muon charge ratio at lower energies can also be measured using the prototype detector which will be placed at the sea level.

Bibliography

- [1] C. Cowan, F. Reines, F. Harrison, H. Kruse, and A. McGuire, *Detection of the free neutrino: A Confirmation*, *Science* **124** (1956) 103–104.
- [2] G. Danby et. al., *Phys. Rev. Lett.* **9**, 36, 1962.
- [3] Kodama et al., DONuT collaboration, *Phys. Lett. B*, 504, 218–224, 2001.
- [4] A. Aguilar et. al., *Phys. Rev. D* **64** (2001) 112007 [hep-ex/0104049].
- [5] C. V. Achar, M. G. K. Menon, V. S. Narasimham, P. V. R. Murthy, B. V. Sreekantan, et al., *Detection of muons produced by cosmic ray neutrinos deep underground*, *Phys.Lett.* **18** (1965) 196–199.
- [6] F. Reines, M. Crouch, T. Jenkins, W. Kropp, H. Gurr, et al., *Evidence for high-energy cosmic ray neutrino interactions*, *Phys.Rev.Lett.* **15** (1965) 429–433.
- [7] Elena Giusarma et al., *PHYSICAL REVIEW D* **90**, 043507 (2014).
- [8] <http://mare.dfm.uninsubria.it/frontend/exec.php>
- [9] Christine Kraus et al., *Eur. Phys. J.* **C73** (2013) 2323
- [10] KATRIN collaboration: A. Osipowicz et al., arXiv:hep-ex/0109033v1
- [11] Spiering, Christian, *Eur.Phys.J.* **H37** (2012) 515–565, arXiv:1207.4952
- [12] T. Araki et al., *Nature* **436**, 499–503 (28 July 2005).
- [13] Wurm, Michael et al., *Astron. Nachr* 331 (2010) 512.
- [14] Raymond Davis, Jr., Don S. Harmer, and Kenneth C. Hoffman, (1968) *Physical ReviewLetters*, 20, 1205.
- [15] John N. Bahcall, Neta A. Bahcall and Giora Shaviv, (1968) *Physical Review Letters*, 20,1209.
- [16] S. N. Ahmed et. al., (SNO Collaboration), *Phys. Rev. Lett.* 92, 181301 (2004) nucl-ex/0309004.
- [17] K. S. Hirata et. al., *Phys. Lett. B* **205**, 416 (1988).
- [18] D. Casper et. al., *Phys. Rev. Lett.* **66**, 2561 (1991).
- [19] Y. Fukuda et. al., hep-ex/9803006.
- [20] Y. Fukuda et. al. (Super-Kamiokande Collaboration) *Phys. Rev. Lett.* **81**, 1562, 1998.
- [21] B. Pontecorvo, *Sov. Phys. JETP* **26**, 984. (1968)
- [22] M. Gonzalez-Garcia, M. Maltoni, and T. Schwetz, *Updated fit to three neutrino mixing: status of leptonic CP violation*, *JHEP* **1411** (2014) 052, [arXiv:1409.5439].
- [23] NuFIT webpage, <http://www.nu-fit.org/>.
- [24] “Physics Potential of the ICAL detector at the India-based Neutrino Observatory (INO)”, ICAL Collaboration, Shakeel Ahmed et al., arXiv:1505.07380 [physics.ins-det], 2015.
- [25] S. Agostinelli et al., *Geant4 - a simulation toolkit*, *Nucl. Instr. & Meth. in Phys. Res. A* **506** (2003) 250–303; <http://geant4.cern.ch/>.
- [26] M.S. Athar et al., 2006 India-based Neutrino Observatory: Project Report Volume I, <http://www.ino.tifr.res.in/ino/OpenReports/INORReport.pdf>.

- [27] D. Casper, *The Nuance neutrino physics simulation, and the future*, Nucl.Phys.Proc.Suppl. **112** (2002) 161–170, [hep-ph/0208030].
- [28] J.A. Formaggio et.al, *From eV to EeV: Neutrino cross sections across energy scales*, Rev. Mod. Phys. **84**, 1307.
- [29] INO Collaboration, *ICAL simulation using GEANT tool-kit*, in preparation, 2014.
- [30] S. P. Behera, M. Bhatia, V. Datar, and A. Mohanty, *Simulation Studies for Electromagnetic Design of INO ICAL Magnet and its Response to Muons*, arXiv:1406.3965.
- [31] Infolytica Corp., Electromagnetic field simulation software, <http://www.infolytica.com/en/products/magnet/>.
- [32] B. Satyanarayana, *Design and Characterisation Studies of Resistive Plate Chambers*, PhD thesis, (Department of Physics, IIT Bombay, PHY-PHD-10-701, 2009).
- [33] M.M. Devi et al., *Hadron energy response of the ICAL detector at INO*, JINST **8** (2013) 11003.
- [34] R.E. Kalman, *A new approach to linear filtering and prediction problems*, Journal of Basic Engineering **82** (1) (1960) 35–45.
- [35] PARTICLE DATA GROUP collaboration, J. Beringer et al., *Review of Particle Physics (RPP)*, Phys. Rev. **D 86** (2012) 010001; <http://pdg.lbl.gov>.
- [36] A. Chatterjee et al., JINST **9** (2014) P07001.
- [37] T. Thakore, A. Ghosh, S. Choubey and A. Dighe, JHEP **1305**, 058 (2013); A. Ghosh, T. Thakore and S. Choubey, JHEP **1304**, 009 (2013).
- [38] M. M. Devi, T. Thakore, S. K. Agarwalla, Amol Dighe, JHEP **1410**, 189 (2014), ArXiv:1406.3689 [hep-ph].
- [39] Lakshmi S Mohan, Thesis
- [40] Moon moon Devi, Thesis
- [41] R. Kanishka et al., JINST **01** (2015) P03011.
- [42] Morihiro Honda, Takaaki Kajita, Katsuaki Kasahara, Shoichi Midorikawa, Phys. Rev. **D 83** (2011) 123001.
- [43] G. Fiorentini, V.A. Naumov and F.L. Billante, Phys. Lett. **B 510** (2001) 173.
- [44] Thomas Hebbeker, Charles Timmermans, Astroparticle Physics **18** (2002) 107–127.
- [45] P. Adamson et al., arXiv:1012.3391v2[hep-ex].
- [46] P. Adamson et al., arXiv:0705.3815v4[hep-ex].
- [47] N. Agafonova et al., arXiv:1003.1907v1[hep-ex].
- [48] P. Achard et al., Physics Lett. **B 598** (2004) 15–32.
- [49] P. A Schreiner et al., arXiv:0906.3726v1[hep-ph].
- [50] K. Nakamura et al., (PDG), JP G **37**, 075021 (2010)
- [51] T.K. Gaisser, Astropart. Phys. **35** (2012) 801, arXiv:1111.6675v2, T.K. Gaisser, S.R. Klein, Astropart. Phys. **64** (2014) 13, arXiv:1409.4924.
- [52] N. Mauri, “Measurement of the atmospheric muon charge ratio with the OPERA detector”, PhD thesis, Universit di Bologna, 2011, http://www.bo.infn.it/opera/docs/phd_thesis-BO-2011_05_20-mauri.pdf.
- [53] M. V. N. Murthy et al., Private communication, 2015. The author is grateful for the topographical map being provided.
- [54] R. Santonico and R. Cardarelli, Nucl. Instr. and Meth. **187** (1981) 377.
- [55] Yu. N. Pestov and G. V. Fedotovitch, Preprint IYAF 77–78, Slac Translation 184 (1978).
- [56] E. Cerron Zeballos et al., Nucl. Instr. Meth., **A374**, 132–135, 1996.

- [57] CMS – Technical Proposal, CERN/LHCC/94–38, December 1994.
- [58] ATLAS Technical Design Report, Muon Spectrometer, CERN/LHCC/97–22, Geneva, 1997.
- [59] Kalweit A (for the ALICE Collaboration) J. Phys. G: Nucl. Part. Phys. 38 (2011) 124073.
- [60] ALICE Collaboration, Technical Design Report of the Time–Of–Flight Detector CERN/LHCC/2000–12; Addendum CERN/LHCC/2002–16.
- [61] I. Crotty, J. Lamas Valverde, G. Laurenti, M.C.S. Williams, A. Zichichi, Nucl. Instr. and Meth. A 346 (1994) 107.
- [62] A. Moshaii, K. Doroud, Nucl. Instr. and Meth. A 602 (2009) 727.
- [63] K. Doroud, A. Moshaii, Nucl. Instr. and Meth. A 602 (2009) 723.
- [64] M. De Vincenzi, Nucl. Instr. and Meth. A 508 (2003) 94.
- [65] S.H. Ahn et al., Nucl. Instr. and Meth. A 451 (2000) 582.
- [66] M. Abbrescia, et al., Nucl. Instr. and Meth. A 359 (1995) 603.
- [67] V M Datar et al., Nuclear Instruments and Methods in Physics Research A 602 (2009) 744.
- [68] S. Biswas et. al., Nuclear Instruments and Methods in Physics Research A 602 (2009) 749.
- [69] S. Biswas et. al., Nuclear Instruments and Methods in Physics Research A 604 (2009) 310.
- [70] K.K. Meghna et. al., JINST 7 (2012) P10003.
- [71] S. Biswas et. al., Nuclear Instruments and Methods in Physics Research A 617 (2010) 138.
- [72] S. Biswas, Ph D Thesis (2010), Calcutta University (unpublished).
- [73] Data Acquisition and Analysis Package LAMPS. (<http://www.tifr.res.in/~pell/lamps.html>).
- [74] G. Chiodini, M.R. Coluccia, E. Gorini, F. Grancagnolo, M. Primavera, S. Stella, Nucl. Instr. and Meth. A 602 (2009) 757.
- [75] Design Guide for High-Speed Controlled Impedance Circuit Boards IPC2141A, IPC, Northbrook, Illinois, USA (March 2004).